

Solar neutrinos with LENA and a spectroscopical analysis of liquid-scintillators

Diploma Thesis
by
Sebastian Todor

November 2008
Physik-Department E15



TECHNISCHE
UNIVERSITÄT
MÜNCHEN

Abstract

The **Low Energy Neutrino Astronomy** (LENA) Project comprises of a 50 kt organic liquid-scintillator detector which is planned to be of cylindrical shape with a length of 100 m and a radius of 15 m. The detector will contain about 13500 photomultipliers (PMTs) on the inner side of the cylinder that will detect the light signals produced in the scintillator by particle events. In order to shield the detector against high energetic components of the cosmic radiation, the detector has to be built either in a deep underground laboratory or on a deep sea plateau. As of today, the most probable future building site will be the Finnish center for underground physics in Pyhäsalmi (CUPP). Such a detector as LENA will only be limited in the detection of ν events by its intrinsic radioactivity and its transparency whereas the current energy threshold for water based Cherenkov detectors is several MeV. The application area of LENA will be manifold, reaching from particle physics (e.g. proton decay, neutrino oscillations) to astrophysical questions (e.g. solar neutrinos, geothermal neutrinos, supernova- and diffuse supernova neutrinos).

Chapter 1 of this thesis gives a short introduction to the standard model of particle physics and to the phenomenology of neutrino oscillations in vacuum and in matter. Chapter 2 gives an overview of the history of neutrino physics and gives an overview over other neutrino experiments.

Chapter 3 contains a brief introduction of the LENA project. The structure of the detector is explained and possible building sites are discussed. The manifold physics capabilities are discussed in detail.

Chapter 4 gives an introduction to the structure of the sun and a description of the processes that take place within it. The phenomenon of solar matter density fluctuations and their correlation to neutrino survival probabilities are also discussed.

Chapter 5 contains a phenomenological approach towards the detection of solar neutrinos in LENA, in special the estimation of event rates of the solar neutrinos from the different fusion cycles, and the calculation of the corresponding electron recoil spectra, such as would be seen in LENA. Additionally, the radioactive background, which is the main background source for solar neutrinos, and its possible implications on the detection of low energetic solar neutrinos is analyzed. Another part of this chapter is an analysis of ${}^8\text{B}$ neutrinos. The goal is to investigate the detection potential of LENA concerning the MSW-LMA solution of the MSW effect in the region between 2-3 MeV. Another investigated topic is the fluctuation of the solar neutrino flux due to the varying distance of the earth to the sun in the course of one year and also due to the earth matter induced day/night-effect. According to theoretical models, solar density fluctuations could also lead to a change of the neutrino flux over time. A limit for the detectability of periodic neutrino flux oscillations in LENA is presented.

Chapter 6 begins with an overview of different types of liquid-scintillators and gives an introduction to the scattering of light in such liquid-scintillators. It follows the

description of the experimental setup for the measurement of scattering lengths of organic liquid-scintillators that are considered for a use in LENA. The measurements were performed for different wavelengths and with different scintillators. The understanding of the optical properties of the liquid-scintillator that will finally come to use in LENA is very important. The results of the scattering length measurement will be used along with other properties of the liquid-scintillator for a Monte Carlo simulation of LENA in the future.

Chapter 7 summarizes the results of this thesis.

Contents

1	The standard model of particle physics and neutrino oscillations	3
1.1	The standard model	3
1.2	Extension of the standard model and neutrino oscillations	4
1.2.1	Neutrino oscillations in vacuum	4
1.2.2	Neutrino oscillations in matter	6
2	History of neutrino physics and an overview of neutrino experiments	9
3	The LENA project	13
3.1	The LENA detector	13
3.1.1	Detector design	13
3.1.2	Detector location	15
3.1.3	Liquid-scintillator	15
3.2	Physics capabilities	16
3.2.1	Solar neutrinos	16
3.2.2	Supernova neutrinos	17
3.2.3	Diffuse supernova neutrinos	18
3.2.4	Terrestrial neutrinos	18
3.2.5	Proton decay	18
3.2.6	Long baseline experiments	19
3.2.7	Dark matter detection	19
4	Properties of the sun	21
4.1	The structure of the sun	21

4.2	The solar fusion cycles	23
4.2.1	pp chain	23
4.2.2	hep, ${}^7\text{Be}$ and ${}^8\text{B}$ chains	24
4.2.3	CNO chain	25
4.3	Solar matter density fluctuations	27
4.3.1	P modes and helioseismology	27
4.3.2	Magneto-gravity modes	28
5	Measurement of solar neutrinos with LENA	31
5.1	Estimation of event rates for solar neutrinos in LENA	31
5.1.1	Reaction rate	31
5.1.2	Results for the event rates	33
5.1.3	The electron recoil spectra	34
5.2	Background sources	35
5.2.1	Reactor antineutrinos and atmospheric neutrinos	37
5.2.2	Background from radionuclides	38
5.2.3	Cosmogenic radionuclides	38
5.2.4	Background rates	39
5.3	${}^8\text{B}$ - ν Analysis with LENA	41
5.3.1	Influence of the MSW effect on the ${}^8\text{B}$ spectrum	42
5.3.2	χ^2 analysis	42
5.3.3	Results and discussion	44
5.4	Periodic oscillations of the ${}^7\text{Be}$ neutrino flux	47
5.4.1	Periodic oscillations of the ${}^7\text{Be}$ neutrino flux due to Kepler motion	50
5.4.2	Periodic oscillations of the ${}^7\text{Be}$ Neutrino Flux due to the day/night-effect or G modes	52
5.5	Results and discussion	54
5.5.1	Analysis of oscillations with 1 day binning	54
5.5.2	Analysis of oscillations with 1 hour binning	66
6	Scattering Length Measurement	71

6.1	On liquid-scintillators	71
6.1.1	The solvent	72
6.1.2	The fluors	74
6.2	Scattering and absorption of light in a liquid-scintillator	75
6.2.1	Scattering theory	75
6.3	Experimental setup	77
6.3.1	Arrangement of the experiment	77
6.4	The measurement	81
6.4.1	Calculation of the scattering lengths	82
6.5	Uncertainty contributions	87
6.5.1	Correlated uncertainties	87
6.5.2	Uncorrelated uncertainties	89
6.6	Results	90
7	Summary and outlook	93
A	Tables of measurements	I
	Bibliography	III

List of Figures

1.1	Survival probability for solar neutrinos	8
3.1	Two schematic views of the the LENA detector	14
4.1	The structure of the sun	21
4.2	The pp cycle and the relation to the hep, ${}^7\text{Be}$ and ${}^8\text{B}$ chains	25
4.3	The CNO-I cycle	26
4.4	The solar neutrino spectrum	27
4.5	P Mode Oscillation	28
4.6	The correlation length of g modes	29
4.7	Impact of G modes on the MSW-LMA survival probability	30
5.1	The electron recoil spectrum from solar neutrinos up to 16 MeV in LENA	36
5.2	Atmospheric neutrino and reactor-antineutrino background in LENA	37
5.3	${}^7\text{Be}$ Spectrum with background	40
5.4	The ${}^8\text{B}$ MSW-LMA probability curve as it has been confirmed today	42
5.5	The ${}^8\text{B}$ neutrino spectrum in LENA with and without MSW effect . .	43
5.6	Simulation of the ${}^8\text{B}$ neutrino spectrum with and without MSW effect after 1 year of runtime	44
5.7	${}^7\text{Be}$ neutrino spectrum after 1 day and 10 days of data aquisition . .	49
5.8	The seasonal ${}^7\text{Be}$ neutrino flux variation	51
5.9	Fit of the seasonal ${}^7\text{Be}-\nu$ flux variation	52
5.10	The ${}^7\text{Be}$ neutrino flux variation due to G modes	53
5.11	χ^2/NDF distribution of the parameters amplitude A and cycle duration T with fixed phase $\phi = 0$ d	55

5.12	Sensitivity plots of the parameters amplitude A , cycle duration T and phase ϕ for oscillations on long time scales	57
5.13	Fixed phase $\phi = 0$ d, $T=3$ d and varying amplitude	58
5.14	Fixed phase $\phi = 0$ d, $T=120$ d and varying amplitude	59
5.15	Fixed phase $\phi = 0$ d, $T=365$ d and varying amplitude	60
5.16	χ^2/NDF distribution for fixed $T=120$ d, and varying amplitude and phase	61
5.17	Fixed cycle duration $T=120$ d fixed amplitude $A=0.5\%$, varying phase ϕ	62
5.18	Fixed cycle duration $T=120$ d fixed amplitude $A=2.5\%$, varying phase ϕ	63
5.19	χ^2/NDF distribution for a fixed amplitude $A=1.5\%$, and varying phase and cycle duration	64
5.20	Fixed amplitude $A=2.5\%$, fixed phase $\phi = 180$ d and varying cycle duration T	65
5.21	Sensitivity plots of the parameters amplitude A , cycle duration T and phase ϕ for oscillations on short time scales (up to $T=8760$ h)	67
5.22	Exclusion plots of the parameters amplitude A , cycle duration T and phase ϕ for oscillations on short time scales (up to $T=100$ h)	68
6.1	The chemical structure of PXE	72
6.2	The chemical structure of dodecane	73
6.3	The chemical structure of LAB	74
6.4	The chemical structure of PPO	74
6.5	Schematics of the experimental setup	78
6.6	Photograph of the experimental setup	79
6.7	The electronics of the experiment	80
6.8	Solid angle correction	85
7.1	Sensitivity plot of the parameters amplitude A , cycle duration T and phase ϕ for oscillations on long time scales on a 99% C.L.	96

List of Tables

1.1	Properties of the interaction forces in the standard model	3
2.1	The neutrino oscillation parameters as they are known today	11
3.1	The possible neutrino detection reaction channels in LENA	16
4.1	The solar parameters	22
4.2	The different fusion chains in the sun	23
5.1	Solar neutrino event rates for LENA	34
5.2	Radioactive background in a liquid-scintillator detector	38
5.3	Estimated background rates for LENA	39
5.4	Results for χ^2/NDF for different runtimes in LENA for $E_{thr} = 2.0$ MeV	45
6.1	List of the examined liquid-scintillator solvents	81
6.2	Results of the scattering length experiment	91
7.1	Solar neutrino event rates for LENA	94
7.2	Estimated background rates for LENA	94
7.3	Results of the scattering length experiment for $\lambda = 430$ nm	97
A.1	The PMT efficiency dependance of the bias	I
A.2	Transmission of the filters dependant on the wavelength	II

Chapter 1

The standard model of particle physics and neutrino oscillations

1.1 The standard model

The standard model comprises of the unified theories of electroweak interaction and quantum chromodynamics (QCD). In group theory this is expressed by the $SU(3)_C \otimes SU(2)_W \otimes U(1)_Y$ group [Buc06].

Besides gravitation, there are three other interaction forces which are very similar in their structure. The respective forces are exchanged via vector bosons with spin 1. Table 1.1 shows the three forces of the standard model together with their properties.

Interaction force	couples to	exchange particle	mass (GeV/c ²)
strong	color charge	8 gluons (g)	0
electromagnetic	electric charge	photon (γ)	0
weak	weak charge	vector bosons W^\pm Z^0	(80.398 ± 0.25) (91.187 ± 0.0021)

Table 1.1: *The properties of the interactions in the standard model of particle physics [Pov01]. All exchange particles are bosonic particles with spin 1.*

Aside from the exchange particles, there exist other fundamental particles, the quarks and leptons. They are spin 1/2 particles, fermions, and can be segregated into three families. The three quark families are:

$$\begin{pmatrix} u \\ d \end{pmatrix}, \begin{pmatrix} c \\ s \end{pmatrix}, \begin{pmatrix} t \\ b \end{pmatrix}$$

In addition to the electric charge, the quarks and the gluons carry color charge, that

in a quark-gluon system such as a hadron or meson, adds up to white [Pov01] in color space. This property is called confinement. In contrast to photons, gluons can couple with themselves. The upper elements of the quark families carry electric charge $+\frac{2}{3}e$ ¹, while the other elements carry $-\frac{1}{3}e$. The gluons do not have an electric charge.

The three lepton families are:

$$\begin{pmatrix} \nu_e \\ e \end{pmatrix}, \begin{pmatrix} \nu_\mu \\ \mu \end{pmatrix}, \begin{pmatrix} \nu_\tau \\ \tau \end{pmatrix}$$

The neutrinos are massless in this model and have no electric charge, while the other leptons have mass and electric charge $-1e$ [Pov01]. The interaction particles are the vector bosons, W^+ , W^- and Z^0 . As the gluons, they also can couple to one another. The theory of the electroweak force states that only left-handed particles can participate in the weak force, carrying a weak isospin of $1/2$. The right-handed part carries weak isospin 0 . Only the neutrinos, which are considered massless in the standard model, do not have a right handed part. Consequently, antineutrinos do not have a left handed part in this model.

However, with the upcoming of neutrino experiments (see chapter 2) this assumption of the standard model was being questioned more and more, until an extension of the standard model was inevitable, leading to the establishment of the model of massive neutrinos and neutrino oscillations. The last remaining particle of the standard model which has not yet been experimentally discovered is the Higgs boson with spin 0 [Alt05a]. It is the mediator of the particle rest masses.

1.2 Extension of the standard model and neutrino oscillations

1.2.1 Neutrino oscillations in vacuum

The following introduction to neutrino oscillations is based on [Scm97]. Neutrino oscillation is a phenomenon that goes beyond the standard model of physics, because it requires the neutrinos to have a non-vanishing mass. It implies oscillatory changes of the lepton flavour eigenstate $L_\alpha \neq L_\beta$ ($\alpha, \beta = e, \mu, \tau$) meaning a change of the neutrino type of the form $\nu_\alpha \longleftrightarrow \nu_\beta$.

In the theory of weak interaction it can be shown that the flavour eigenvalues of neutrinos suffice the following relations:

¹ e being the elementary charge $e = 1.602 \cdot 10^{-19}C$

$$L_\alpha|\nu_\beta\rangle = \delta_{\alpha\beta}|\nu_\beta\rangle; \quad (1.1)$$

$$L_\alpha|\bar{\nu}_\beta\rangle = -\delta_{\alpha\beta}|\bar{\nu}_\beta\rangle \quad (1.2)$$

In general these eigenstates do not have an exact defined mass, meaning they are not eigenstates of the mass operator M :

$$\langle\nu_\alpha|M|\nu_\beta\rangle \neq 0 \quad \text{for } \alpha \neq \beta \quad (1.3)$$

They rather are linear combinations of non-degenerate mass eigenstates $|\nu_i\rangle$ with fixed masses m_i :

$$\langle\nu_i|M|\nu_j\rangle = m_i\delta_{ij} \quad \text{with } m_i - m_j \neq 0 \quad \text{for } i \neq j \quad (1.4)$$

That is why the mass eigenstates $|\nu_i\rangle$ develop with different phases throughout the propagation of time. As a consequence, a well defined flavour eigenstate ν_α can be described as a time dependent mixing of different mass eigenstates thus being detected with a certain (oscillating) probability as another neutrino flavour ν_β (with $\alpha \neq \beta$).

Leaving aside the possibility of heavy neutrinos, it is known that there are exactly three light neutrino flavour eigenstates and thus three mass eigenstates. In the theory of Hilbert spaces one can find an unitary² matrix U transforming the flavour eigenstates into the mass eigenstates and vice versa:

$$|\nu_\alpha\rangle = \sum_i U_{\alpha i}|\nu_i\rangle \quad (1.5)$$

$$|\nu_i\rangle = \sum_\alpha (U^\dagger)_{i\alpha}|\nu_\alpha\rangle \quad (1.6)$$

$U_{\alpha i}$ is the Pontcorvo-Maki-Nakagawa-Sakata matrix [Kot05]. It can be written as:

$$\begin{aligned} U &= \begin{pmatrix} 1 & 0 & 0 \\ 0 & c_{23} & s_{23} \\ 0 & -s_{23} & c_{23} \end{pmatrix} \cdot \begin{pmatrix} c_{13} & 0 & s_{13}e^{-i\delta} \\ 0 & 1 & 0 \\ -s_{13}e^{-i\delta} & 0 & c_{13} \end{pmatrix} \cdot \begin{pmatrix} c_{12} & s_{12} & 0 \\ -s_{12} & c_{12} & 0 \\ 0 & 0 & 1 \end{pmatrix} \\ &= \begin{pmatrix} U_{e1} & U_{e2} & U_{e3} \\ U_{\mu 1} & U_{\mu 2} & U_{\mu 3} \\ U_{\tau 1} & U_{\tau 2} & U_{\tau 3} \end{pmatrix} \end{aligned} \quad (1.7)$$

where s_{ij} and c_{ij} ($i = 1, 2, 3$) stand for $\sin(\theta_{ij})$ and $\cos(\theta_{ij})$, respectively. θ_{ij} are the rotary mixing angles and δ stands for a possible CP-violating phase.

²Unitary transformations suffice the constraint $U^\dagger = U^{-1}$.

The mass eigenstates $|\nu_i\rangle$ have a time evolution given by^{3,4}

$$|\nu_i(t)\rangle = e^{-i\hat{H}t}|\nu_i\rangle = e^{-iE_it}|\nu_i\rangle \quad (1.8)$$

with the energy eigenvalues given by the relativistic equation

$$E_i = \sqrt{p^2 + m_i^2} \approx p + \frac{m_i^2}{2p} \approx E + \frac{m_i^2}{2E} \quad (1.9)$$

for $p \gg m_i$, whereas $E \approx p$ is the mean neutrino energy. A flavour eigenstate, that is given for $t=0$ as $|\nu_\alpha\rangle = \sum_i U_{\alpha i}|\nu_i\rangle$, will thus develop through time into a state

$$|\nu(t)\rangle = \sum_i U_{\alpha i} e^{-iE_it} |\nu_i\rangle = \sum_{i,\beta} U_{\alpha i} U_{\beta i}^* e^{-iE_it} |\nu_\beta\rangle \quad (1.10)$$

The probability of a neutrino flavour change can then be calculated to⁵

$$\begin{aligned} P(\alpha \rightarrow \beta, t) &= |A(\alpha \rightarrow \beta, t)|^2 = |\langle \nu_\alpha(t) | \nu_\beta \rangle|^2 = \left| \sum_i U_{\alpha i} U_{\beta i}^* e^{-iE_it} \right|^2 = \\ &= \sum_{i,j} U_{\alpha i} U_{\alpha j}^* U_{\beta i} U_{\beta j} e^{-i(E_i - E_j)t} \\ &= \sum_i |U_{\alpha i} U_{\beta i}^*|^2 + 2\text{Re} \sum_{j>i} U_{\alpha i} U_{\alpha j}^* U_{\beta i} U_{\beta j} e^{-i\Delta_{ij}} \end{aligned} \quad (1.11)$$

with the phase difference

$$\Delta_{ij} := (E_i - E_j)t = \frac{\Delta m_{ij}^2}{2} \cdot \frac{L}{E}, \quad \text{with } \Delta m_{ij}^2 = m_i^2 - m_j^2 \quad (1.12)$$

which implies that neutrino oscillations can only occur for non degenerate mass eigenvalues. L denotes the distance between source and point of detection.

1.2.2 Neutrino oscillations in matter

In comparison to the two neutrinos ν_μ and ν_τ that can scatter on electrons only via the exchange of a neutral current (Z^0), the ν_e can additionally scatter via the exchange of a charged current (W^\pm). This leads to an additional potential V for the

³Neutrinos are assumed to be stable, thus E_i being a real eigenvalue

⁴For reasons of simplicity $\hbar = 1 = c$

⁵Making use of the orthogonality relation $\langle \nu_\alpha | \nu_\beta \rangle = \delta_{\alpha\beta}$

electron neutrinos in matter⁶ which results in a change of the oscillation parameters [MS85]. In case of constant matter density, the situation is essentially the same as for the vacuum oscillations, only with different mixing angles [MS85]. In case of a varying matter density however, there can occur a resonance effect, which can enhance the transition probability maximally, and is referred to as the Mikheyev-Smirnov-Wolfenstein (MSW) effect [Wol78]. This effect plays the key role in the solar neutrino deficit [Bah03], and is also important for supernova neutrinos [Win07]. The survival probability for solar neutrinos is the probability of an electron neutrino of the production mechanism $K = pp, pep, {}^7\text{Be}, {}^{13}\text{N}, {}^{15}\text{O}, {}^{17}\text{F}, {}^8\text{B}$ (see chapter 4.2), not to change its flavour when passing through the solar matter ($P_{ee} = P_{\nu_e \rightarrow \nu_e}$). Here the LMA (Large Mixing Angle)⁷ solution is used, because the SMA (Small Mixing Angle)⁸ solution was ruled out by solar neutrino experiments [Bah03]. The survival probability P_{ee} can be derived analytically [Hol04] to

$$P_{ee}(\langle V_K \rangle) = \frac{1}{2} + \frac{1}{2}(1 - \delta_k) \cos(2\theta_m) \langle V_K \rangle \cos(2\theta) \quad (1.13)$$

where θ is the vacuum mixing angle. $\langle V_K \rangle$ is the averaged value of the potential in the production region for the neutrino sort K . The mixing angle in matter suffices the equation

$$\cos(2\theta_m(V)) = \frac{\cos(2\theta) - 2EV/\Delta m^2}{[(\cos(2\theta) - 2EV/\Delta m^2)^2 + \sin^2(2\theta)]^{1/2}} \quad (1.14)$$

with $V = \sqrt{2}G_F n_e(x)$ being the additional potential for electron neutrinos, and $n_e(x)$ being the number density of electrons in the point x . The correction term δ_K is given through

$$\delta_K = \frac{3}{2} \frac{(2E\langle V_K \rangle/\Delta m^2)^2 \sin^2(2\theta)}{[(\cos(2\theta) - 2E\langle V_K \rangle/\Delta m^2)^2 + \sin^2(2\theta)]^2} \frac{\Delta V_K^2}{\langle V_K \rangle^2} \quad (1.15)$$

The values for $\frac{\Delta V_K^2}{\langle V_K \rangle^2}$ and $\langle V_K \rangle$ for the neutrino from fusion process K are also taken from [Hol04]. This is then used to calculate the survival probability for a neutrino from the fusion chain K (see chapter 4.2) with respect to its energy. The survival probability for the solar neutrinos of the different fusion chains is shown in Figure 2.1. As can be seen, the survival probability is high (0.55-0.57) for small neutrino energies below ~ 1 MeV. This is the energy regime where neutrino oscillations are vacuum dominated. For energies higher than ~ 10 MeV, the survival probability is lower (0.31-0.35). The survival probability is different for the neutrinos from the

⁶Because regular matter contains only electrons, not μ^\pm, τ^\pm or positrons.

⁷ $\sin^2(2\theta_{12,matter}) \approx O(10^{-3})$ [Kin99]

⁸ $0.6 \leq \sin^2(2\theta_{12,matter}) \leq 1$ [Pet01]

different fusion processes. This is because the mean potential $\langle V_K \rangle$ is a function of the density and the density depends on the radial distance to the core, which is linked to the production region of the different neutrinos [Scm97]. This survival

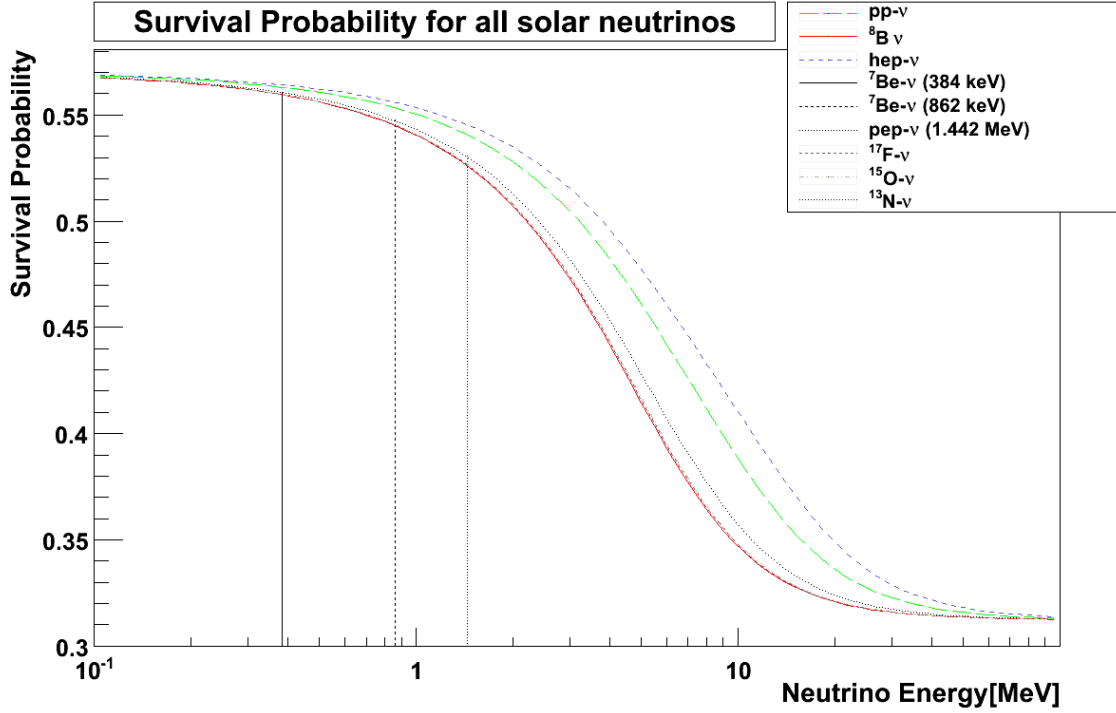


Figure 1.1: *Survival probability for the solar neutrinos from the different fusion chains (symbolized with different colours) due to the MSW effect for the LMA solution, according to equation 1.15. It is plotted as a function of the neutrino energy in MeV on a logarithmic scale. The different mean potential for a neutrino from the production mechanism $K = pp, pep, {}^7\text{Be}, {}^{13}\text{N}, {}^{15}\text{O}, {}^{17}\text{F}, {}^8\text{B}$ leads to different survival probabilities. The three lines represent the two monoenergetic ${}^7\text{Be}$ neutrino lines at 384 keV and 862 keV and the pep neutrino line at 1.442 MeV, respectively.*

probability will be used to calculate the event rates of solar neutrinos in LENA in chapter 5.1.

Chapter 2

History of neutrino physics and an overview of neutrino experiments

In the 1930s the neutrino first was postulated by Wolfgang Pauli out of physical necessity (conservation of energy, momentum and spin) for the β decay. The implications of the neutrino on astrophysics and cosmology were difficult to imagine back then. Nowadays neutrino astronomy has been well established and is an important branch of physics which combines two major fields, elementary particle physics and astrophysics. Until it got that far, neutrino physics had to undergo a long evolution. When the neutrino was first experimentally detected in 1956 by Reines and Cowan [RC56], almost nothing was known about this particle except that it was weakly interacting and electrically neutral. That is why often in literature neutrinos were referred to as "ghost particles". Only slowly more physical properties of the neutrino were revealed, such as that there are exactly three light neutrino flavours, which could be derived from the decay of the Z^0 Boson at the particle accelerator LEP at CERN [Scm97].

It soon showed that these particles have very interesting properties which make them a very good choice for particle experiments with an astrophysical background. As an example, whenever a massive star collapses, neutrinos play a fundamental role in this process. As was shown, 99% of the total energy of a supernova explosion is released via the emission of neutrinos [Scm97]. This massive neutrino flux is detectable here on earth and delivers important insights that could lead to a better understanding of supernova physics. Only one supernova explosion in the history of neutrino physics was detected, the supernova 1987a in the great magellanic cloud. However, experimental neutrino physics back then was not as sophisticated as it has become today, thus the results are quite contradictory [Hir87] [Bio87] [Bra88] [Hir88].

Supernova explosions throughout the history of the universe released so many neutrinos, that they form a so called diffuse supernova neutrino background (DSNB) [Lun06] [Mal03] which might be detectable in a large liquid-scintillator detector.

Another phenomenon that was for a long time unsolved are the so-called gamma ray bursts (GRBs), that were first detected in the 1990s and have remained a mystery for a long time [Mes06]. Newer observations have led to the conclusion that there are two types of bursts: long ones, which have their cause in the collapse of a massive Wolf-Rayet star⁹, and short ones, which could be caused by the merging of two neutron stars or a neutron star and a black hole [Mes06]. For either of these two processes neutrinos could deliver important information on the astrophysical mechanisms involved [Sur08].

The detection of high energetic neutrinos from cosmic point sources in general, for example from active galactic nuclei (AGN), requires a large detector volume because of the very low fluxes ($E_\nu^2 \Phi_{lim} = 5.9 \cdot 10^{-8} \text{ GeV cm}^2 \text{ s}^{-1}$ [Bec07]). Attempts to detect such very high energetic neutrinos have been realised in large Cherenkov detectors that use ice or water such as AMANDA [Ama05] and BAIKAL [Bai06], respectively. As of now, no neutrino emitting point source could be identified yet.

Another experiment of this class which is almost finished and soon will start with the aquisition of data is ANTARES in 2500 m depth offshore of Toulon, France [Age07]. Future detectors in this category are large km^3 detectors such as IceCUBE [Kir08] at the AMANDA site and KM3Net [Lyo08], which will be built like ANTARES in the sea. They might have a large enough detection volume to identify high energetic neutrinos from cosmological sources.

Another field where neutrinos can be used, is the study of radiochemical processes that take place within the earth via geothermal neutrinos produced by the decay of Uranium, Thorium and their decay products, and ^{40}K . With this method, new abundancies of radioactive isotopes within the earth could be estimated [Hoc07].

Atmospheric neutrinos have been used by the Super-Kamiokande detector to measure the oscillation $\nu_\mu \rightarrow \nu_\tau$ [Ash05], which was a major breakthrough for the establishment of neutrino oscillations.

In order to investigate stellar dynamics and other astrophysical properties of a star with neutrinos, the investigation of the nearest star, the sun, seems the best choice, because of the very high solar neutrino flux here on earth of about $6 \cdot 10^{10} \text{ s}^{-1} \text{ cm}^{-2}$. The first neutrino experiment that attempted the detection of these solar neutrinos was the Homestake experiment of R. Davis in the early 1970s [Dav94], which showed a significant deficit in the ν_e flux compared to the expactations predicted by the standard solar model. Even the following experiments GALLEX/GNO [Alt05] and SAGE [Abd02] made similar observations, which led to several theories that tried to explain this deficit of electron neutrinos (e.g. non standard solar models or neutrino oscillations). With the results delivered by the SNO [Bou02] and the Super-Kamiokande [Ahm02] experiments the neutrino oscillations were proven to be the source for the missing solar neutrino flux.

Another solar neutrino experiment that has begun taking data only in 2007, is the Borexino experiment situated at the Gran Sasso underground laboratory in Italy

⁹massive stars of over 20 solar masses and surface temperatures of $(2.5 - 5.0) \cdot 10^4 \text{ K}$

[Bx07a]. This detector is a liquid-scintillator detector based on Pseudocumene and has a fiducial mass of 100 tons. Due to its extremely high radiopurity, the detector is able to measure low energetic neutrinos in the regime below 1 MeV, which is impossible to achieve with Cherenkov detectors, due to their high detection threshold. These factors made it possible to detect the first real time signal of the ${}^7\text{Be}$ neutrino flux in August 2007 [Bx07a]. Only recently, the Borexino detector was able to measure ${}^8\text{B}$ neutrinos with the lowest threshold energy achieved so far (2.8 MeV) [Bx08b]. With this measurement, for the first time the presence of a transition between the low energy vacuum dominated, and the high energy matter induced solar neutrino oscillations was confirmed, in agreement with the MSW-LMA solution for solar neutrinos [Bx08b].

Appearance and disappearance experiments have delivered hard proof for neutrino oscillations, thus implying that neutrinos have a non vanishing mass. These results were confirmed by the reactor antineutrino disappearance experiment KamLAND [Egu03] and the accelerator experiment K2K [Yok05] for $\nu_e \leftrightarrow \nu_\mu$ and $\nu_\mu \leftrightarrow \nu_\tau$, respectively.

An appearance experiment that has already successfully collected data in a testrun, is the OPERA experiment [Ope08] which is situated at the LNGS in Italy. Its aim is the appearance detection of ν_τ from a beam of ν_μ which is generated at CERN and sent to LNGS with a baseline of 730 km.

Another long baseline experiment which has recently published results [Ada08], is the MINOS experiment at Fermilab, USA. It is a ν_μ disappearance experiment in which the oscillation parameters for an oscillation to ν_τ is being investigated and a new best fit for $\sin^2(2\theta_{23})$ and Δm_{23}^2 was released this year. Also oscillations of the type $\nu_\mu \rightarrow \nu_{sterile}$ can be excluded by MINOS. Table 1.1 shows the neutrino oscillation parameters with today's accuracy: Currently, the best limit for $\sin^2(2\theta_{13})$

Oscillation parameter	value (90 % C.L.)	source
$\sin^2(2\theta_{12})$	$0.86^{+0.03}_{-0.04}$	KamLAND [Yao06]
$\sin^2(2\theta_{23})$	~ 1.00	MINOS [Ada08]
$\sin^2(2\theta_{13})$	< 0.19	CHOOZ [Yao06]
Δm_{12}^2	$(8.0 \pm 0.3) \cdot 10^{-5} \text{ eV}^2$	KamLAND [Yao06]
Δm_{23}^2	$(2.4 \pm 0.13) \cdot 10^{-3} \text{ eV}^2$	MINOS [Ada08]

Table 2.1: *The neutrino oscillation parameters as they are known today.*

comes from the CHOOZ experiment [Apo03]. This was a reactor antineutrino disappearance experiment at the Chooz nuclear power station in France. In order to find a better limit for θ_{13} , the experiment DOUBLE-CHOOZ was proposed and has already entered the building phase in June 2008. After three years of measurement, it will corner the value of $\sin^2(2\theta_{13})$ to 0.02-0.03 [Ard08].

Besides the lacking knowledge of θ_{13} , there are other unsolved questions concerning the neutrino, for example if the neutrino is a Majorana particle (where $\bar{\nu}$ is a right-handed ν state, which is equivalent to the violation of the lepton number) or if it is a Dirac particle ($\bar{\nu} \neq \nu$). A possible experimental test for this question was proposed by the Heidelberg-Moscow [Kla01] collaboration meaning that the existence of a neutrinoless double beta decay should coincide with the neutrino being a Majorana particle [Scm97]. However, the results are not definite. The next generation experiment to solve this question, GERDA, is currently being built at the Gran Sasso Underground Laboratory [Bet07]. It will be based on ^{76}Ge , but will have a higher statistics than the Heidelberg-Moscow experiment.

Another question still to be solved is why the masses of the neutrinos are so much smaller than the masses of the charged leptons. A possible solution to this question might be the See-Saw-Mechanism [Fal06]. Also the mass hierarchy of the neutrinos is still unknown, because only the squared mass differences of the neutrino mass eigenstates can be measured experimentally up to now, not their absolute masses. An experiment that will attempt to measure the ν_e mass via the decay reaction $^3\text{H} \rightarrow ^3\text{He} + e^- + \bar{\nu}_e$ is KATRIN [KAT04]. A limit for the ν_e mass will be derived by the shape of the β spectrum at the endpoint energy of 18.57 keV [KAT04].

Additionally there remains the question if there exists a sterile neutrino, which is a right handed neutrino that is not participating in the weak interaction. There are also more exotic theories that suggest mass-varying neutrinos which could strongly affect cosmological parameters [Fra08]. As can be seen, many interesting challenges are still offered in the field of astro-particle physics.

A large liquid-scintillation detector such as LENA (**L**ow **E**nergy **N**eutrino **A**stronomy) would offer with its large 50kt volume the necessary prerequisites for a large variety of applications. Its low threshold of about 200 keV-250 keV, the high energy resolution and the fast timing would allow real time spectroscopy of low energetic neutrinos like geo- or solar neutrinos [Hoc07], while the large number of protons in the scintillator would make the search for a hypothetical proton decay feasible [Mar05]. Even the observation of DSN (Diffuse Supernova Neutrinos) would be possible due to the good background rejection [Wur05].

Chapter 3

The LENA project

The LENA (**L**ow **E**nergy **N**eutrino **A**stronomy) project is part of the LAGUNA (**L**arge **A**pparatus for **G**rand **U**nification and **N**eutrino **A**strophysics) network. A study concerning the possibilities of LAGUNA in different fields, such as proton decay or astro- and geoneutrino detection, can be found in [Aut07]. The LAGUNA network consists of more than 20 institutes in 11 European countries. The other proposed projects of the network besides LENA are MEMPHYS (**M**Egaton **M**ass **P**HYSics), a 1 Mt water Cherenkov detector, and GLACIER (**G**iant **L**iquid **A**rgon **C**harge **I**maging **E**xpe**R**iment), a 100 kt liquid argon detector [Aut07].

3.1 The LENA detector

3.1.1 Detector design

In the current stage of planning, the LENA detector is of cylindrical shape with a diameter of approximately 30 m and a length of about 100 m (see Figure 3.1). Within an underground cavern, for example at Pyhäsalmi (Finland) at a depth of 1450 m (4060 m.w.e.), large pressure forces act on the detector. For such an underground site, recent studies have shown that a vertical setup might be more feasible in terms of stability [Kal08]. In this study, the cavern is formed in an oval shape in order to dissipate the pressure acting on the detector as good as possible. Studies (see [Wur07]) suggest the detector to comprise of an inner vessel with a length of 96 m and a diameter of 13 m, which is filled with 50 kt of liquid-scintillator. It is surrounded by a 2 m wide, water filled shielding, that serves as a muon veto as well as a shielding against external radioactivity. Depending on the measurement channel and the radiopurity, the fiducial volume of the detector is in the range of 18 kt - 30 kt.

The surface of the inner vessel is equipped with about 13.500 PMTs, that collect the

scintillation light and yield a surface coverage of 30%. Beginning from the outside

DETECTOR LAYOUT

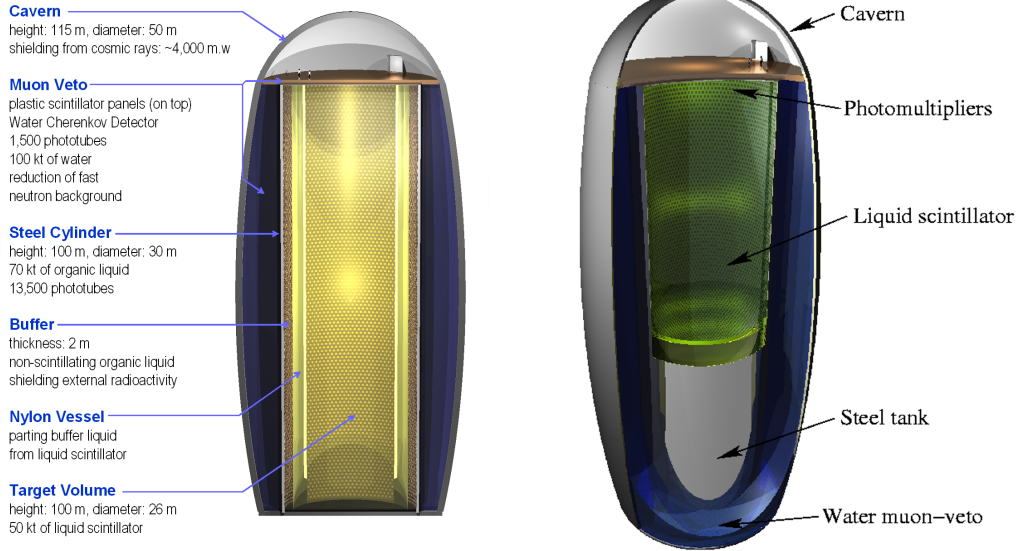


Figure 3.1: Two schematic views of the cylindrical detector LENA which show the components of the detector. New results indicate that a vertical setup is more feasible in terms of pressure forces that act on the detector [Kal08].

of the schematic view in Figure 3.1, the outermost layer is the cavern, in which the detector is placed. Next is the myon veto, which comprises of 100 kt of ultra pure water and 1500 photomultipliers. Muons will then be detected by the Cherenkov light they emit when passing through the water. Also the water lowers the background from fast neutrons. The next layer is the steel cylinder, which contains 70 kt of organic liquids. The first layer of the interior is the buffer that shields the target volume from external radioactivity. It contains a non-scintillating organic liquid and has a thickness of 2 meters. The innermost part of the detector is the target volume which is separated from the buffer by a nylon vessel and contains 50 kt of liquid-scintillator. Here the actual neutrino detections takes place. As was mentioned, the fiducial volume is not fixed yet, but for this thesis, it was set to 18 kt for all calculations, in order to have the most conservative estimate.

The detector is aimed at a detection threshold of 200 keV - 250 keV, yielding 24- 30 photoelectrons at threshold, respectively [Mar06]. This corresponds a light yield of 120 photoelectrons per MeV.

3.1.2 Detector location

As for the site of the detector, many have been proposed throughout the whole of Europe. A complete collection of the possible sites can be found in [Win07]. The prerequisite for sufficient shielding against atmospheric muons is an underground site or a site in the deep sea. One of the proposed sites is on a deep sea plateau off the shore of Pylos, Greece in 4000 m - 5000 m depth [Mar06]. The other suitable site would be at the Center for Underground Physics in Pyhäsalmi (CUPP) [Wur07] which would provide a shielding of 4060 m water equivalent. Both detector sites are far off nuclear power plants which limits the $\bar{\nu}_e$ flux to $1.9 \cdot 10^5 \text{ cm}^{-1}\text{s}^{-1}$ for Pyhäsalmi and $1.1 \cdot 10^5 \text{ cm}^{-1}\text{s}^{-1}$ for Pylos, respectively [Win07].

3.1.3 Liquid-scintillator

The organic liquid-scintillator which is considered for a use in a detector of such magnitude as LENA, has to suffice several demands. For one thing it should offer an attenuation length which lies in the order of the detector radius (See chapter 6.1) so that photons which are emitted in the center of the detector can reach the PMTs. Also aspects like the light yield, the fluorescence decay time, the chemical long term stability and the radiopurity are of major concern for the right choice of the liquid-scintillator. In terms of safety, the flash point and the toxicity are being regarded as well. The costs are also a major factor for the choice of the right liquid-scintillator.

A liquid-scintillator comprises usually of a solvent (mainly hydrogen and carbon) with one or more fluors, which act as wavelength shifters. They are added in a concentration of a few g/l. Without the addition of those wavelength shifters, the excitation caused by a passing particle in the solvent would be captured through to a chain of absorption and reemission processes in the UV range, thus no light would be detected by the PMTs. There can also be added secondary wavelength shifters so that the scintillation light is shifted overall from the UV range to the blue part of the visible spectrum. Fluors that are currently being investigated are 2,5-Diphenyloxazole (PPO), para-Terphenyl (pTP), 1-Phenyl-3-Mesityl-2-Pyrazolin (PMP), and 1,4-bis-(o-methylstyryl)-benzole (bisMSB).

Solvents under investigation are Phenyl-o-Xylylethane (PXE) and different sorts of Linear Alkylbenzene (LABp500, LABp550, LABp550q). There is also the possibility of adding linear hydrocarbons (dodecane or tetradecane) in order to increase the ratio of free protons to carbon in the solvent. In chapter 6.1, the investigated liquid-scintillators for the scattering experiment will be discussed in more detail.

3.2 Physics capabilities

Because of its low energy threshold, the LENA detector could detect neutrinos from very different sources. The main sources of interest for the LENA detector are Solar Neutrinos, which make up the first part of this thesis, supernova and diffuse supernova neutrinos (DSN), terrestrial neutrinos and atmospheric neutrinos. Because of the large amount of atoms in the scintillation volume, the detector would also be suitable for the detection of the proton decay, which is predicted by several grand unified theories [Wie04]. A short overview of the different reaction channels in LENA is given in Table 3.1.

CCR		
channel nr.	reaction channel	E_{thr} [MeV]
1	$\bar{\nu}_e + p \rightarrow n + e^+$	1.8
2	$\bar{\nu}_e + {}^{12}\text{C} \rightarrow {}^{12}\text{B} + e^+$	14.39
3	$\nu_e + {}^{12}\text{C} \rightarrow {}^{12}\text{N} + e^-$	17.34
4	$\nu_e + {}^{13}\text{C} \rightarrow {}^{13}\text{N} + e^-$	2.22
NCR		
channel nr.	reaction channel	E_{thr} [MeV]
5	$\nu_x + {}^{12}\text{C} \rightarrow {}^{12}\text{C}^* + \nu_x$	15.11
6	$\nu_x + p \rightarrow p + \nu_x$	-
7	$\nu_x + e^- \rightarrow e^- + \nu_x$	-
8	$\nu_x + {}^{13}\text{C} \rightarrow {}^{13}\text{C}^* + \nu_x$	3.68

Table 3.1: *The possible neutrino detection reaction channels in LENA. They can be divided into charged current reactions (CCR) and neutral current reactions (NCR). E_{thr} is the threshold energy of the reactions.*

3.2.1 Solar neutrinos

Solar neutrinos are a fundamental probe for the interior of the sun, because the neutrino fluxes are correlated with properties like density and temperature of the solar core. The fluxes are well predicted through the standard solar model [Bah05]. Super-Kamiokande [Ash05] and SNO [Bou02] measured the solar spectrum above a threshold of 5.5 MeV. Gallium based experiments like GALLEX [Alt95], GNO [Alt05] and SAGE [Abd02] were only sensitive to the integrated neutrino flux, but with a lower threshold than water Cherenkov detectors.

As will be shown in Chapter 5, LENA would be able to detect the monoenergetic ${}^7\text{Be}$ neutrinos via elastic neutrino electron scattering with a rate of ~ 5400 events per day for a conservative fiducial volume of 18 kt. The monoenergetic pep neutrinos will induce an event rate of $\sim 370 \text{ d}^{-1}$. The CNO neutrino event rate has been

calculated to $\sim 1250 \text{ d}^{-1}$. The ${}^8\text{B}$ neutrinos would be detected additionally to the elastic neutrino electron scattering via the CC capture of ν_e by ${}^{13}\text{C}$. The event rates are $\sim 27900 \text{ yr}^{-1}$ for the elastic channel and $\sim 680 \text{ yr}^{-1}$ for the CC capture channel, respectively (see chapter 5.2). The rate of hep- ν has been calculated to $\sim 58 \text{ yr}^{-1}$. Because ${}^{14}\text{C}$ is very abundant in an organic liquid-scintillator, the pp-flux cannot be measured directly. But using the measurements of the pep neutrino flux, which is correlated to the pp neutrino flux, the well-known solar luminosity and ν -oscillation parameters, the pp-flux could be determined to an accuracy better than 0.5%. Spectroscopy of the pep neutrinos could be used to investigate the MSW effect in the transition region regime from vacuum to matter induced flavour oscillations at 1-2 MeV (See Figure 1.1). In the regime between 2-3 MeV, ${}^8\text{B}$ neutrinos would be best suitable for an analysis of the MSW-LMA curve. An analysis of the MSW-LMA curve with ${}^8\text{B}$ neutrinos in this energy regime is performed for LENA in chapter 5.3. Due to the very high event rates in the detector, LENA is able to look for fluctuations in the neutrino fluxes. Besides from fluctuations with a periodicity of one year due to the excentricity of the earth orbit, magnetic driven density fluctuations of the solar medium (G modes, see [Bur03a] [Kum99]) might also lead to fluctuations of the neutrino flux. This is analyzed in further detail in chapter 5.4. Some models suggest additionally a slight seasonal variation of the neutrino flux caused by the non-spherical symmetry of those modes [Bur03c]. A day-night asymmetry of about 1% of the ${}^7\text{Be} - \nu$, because of the earth matter effect, might also lie within reach of detection [MS85] [Wol78] [Akh93]. The detectability of oscillatory fluctuations of the solar neutrino flux at the scale of the earth matter effect is investigated in chapter 5.5.2.

3.2.2 Supernova neutrinos

An $8 M_{\odot}^{10}$ star, that explodes in a supernova in the centre of the galaxy (10 kPc distance), will induce a signal rate of $\sim 2 \cdot 10^4$ events in LENA. Both ν_e and $\bar{\nu}_e$ are produced in a supernova, they could be discriminated by charged current reactions, antineutrinos via inverse beta decay and neutrinos via interaction with ${}^{12}\text{C}$. In this way LENA will deliver information on the ν_e and $\bar{\nu}_e$ flux and on the spectrum. The neutral current reactions are sensitive to all neutrino flavours and would thus deliver the total flux [Obe05].

Because of the high event rate for supernova neutrinos, the statistics are very good, so that a time resolved neutrino-flux rate could be measured for different neutrino interactions. This would deliver new results on astrophysical models for the dynamics of supernova explosions.

¹⁰ $1 M_{\odot} = 1 \text{ solar mass} = 1.99 \cdot 10^{30} \text{ kg}$

3.2.3 Diffuse supernova neutrinos

It is assumed that all the supernova explosions throughout the history of the universe have produced a massive neutrino flux which resulted in a background of diffuse supernova neutrinos (DSN). These neutrinos provide information about supernova mechanisms, as well as the stellar formation rate (SFR). Currently the best limit for the DSN-flux comes from the Super-Kamiokande Experiment, giving an upper limit of $1.2 \text{ cm}^{-2}\text{s}^{-1}$ for ν_e with an energy threshold of 19.3 MeV [Mal03]. Through a better background rejection, LENA will be able to detect DSN- ν through inverse beta decay $\bar{\nu}_e + p \rightarrow n + e^+$ in an energy window of 10-25 MeV [Win07]. The limits are given by the flux of neutrinos from nuclear power plants and atmospheric neutrinos. The accuracy for the detection of DSN- ν is thus extremely dependant on the detector location.

3.2.4 Terrestrial neutrinos

A very promising way of investigating processes that take place within the earth, is through the detection of geo or terrestrial neutrinos. They are constantly produced within the earth mantle and crust through the decay of radioactive isotopes such as ^{40}K , ^{232}Th and ^{238}U . The thermal energy created by the decay chains of these isotopes contributes to more than half of the thermal energy flow of the earth of about 60 mW m^{-2} [Hoc07]. The other part is thought to be emitted by latent heat through geochemical processes [GO05]. Electron antineutrinos, which are produced in these decays, could deliver valuable information about the amount of the radioactive materials within the earth. In 2005 KamLAND was able to detect geo neutrinos for the first time [Ara05].

LENA would detect terrestrial neutrinos via the inverse beta decay channel $\bar{\nu}_e + p \rightarrow n + e^+$. The threshold of 1.8 MeV would only allow $\bar{\nu}_e$ from Uranium and Thorium to be detected. Because the main background in this energy region is produced by nuclear power plants, the detector location is essential for the measurement of geo neutrinos. An event rate between $\sim 500 \text{ yr}^{-1}$ and $\sim 1000 \text{ yr}^{-1}$ has been estimated for a detector location at Hawaii or Pyhäsalmi, respectively [Hoc07].

3.2.5 Proton decay

Grand Unification theories that attempt to unify the four fundamental forces, predict that the proton decays with a large lifetime [Wie04]. Currently the experimental limit of the lifetime is $\tau_p > 2.3 \cdot 10^{33} \text{ yr}$ at 90 % C.L. for the decay channel $p \rightarrow K^+ + \bar{\nu}$ [Kob05] and $\tau_p > 5.4 \cdot 10^{33} \text{ yr}$ at 90 % C.L. for the decay channel $p \rightarrow e^+ + \pi^0$ [Hak05]. About 40.7 proton decay events would be observed in LENA after a measuring time of 10 years with about 1.1 background events for the decay channel $p \rightarrow K^+ + \bar{\nu}$ [Mar05]. If no signal is seen within this timespan for this channel, the lower limit

of the proton lifetime will be raised to $\tau > 4 \cdot 10^{34}$ yr at 90 % C.L. This lies within the order of theoretical predictions of ($\sim 10^{30} - 10^{35}$) yr, depending on the model [Rab02].

3.2.6 Long baseline experiments

A beam of neutrinos, produced in artificial sources like particle accelerators, could be directed towards LENA. The high statistics of LENA would offer the possibility to investigate the values of the neutrino oscillation parameters such as θ_{13} , a possible CP-violating phase, or the influence of the earth matter on neutrino oscillations.

3.2.7 Dark matter detection

Another possibility that could be offered by LENA, is the detection of a certain type of dark matter. Besides the lightest supersymmetric particle (neutralino), there could also be lighter particles as candidates for the dark matter [Boe04] in the mass region of 10-100 MeV. The signature would result from the annihilation of this kind of dark matter via $\chi\chi \rightarrow \nu\bar{\nu}$ throughout our galaxy. Due to the good energy resolution and the clear signature of $\bar{\nu}_e$ in LENA, the detector will be able to detect these particles [Mar08].

Chapter 4

Properties of the sun

4.1 The structure of the sun

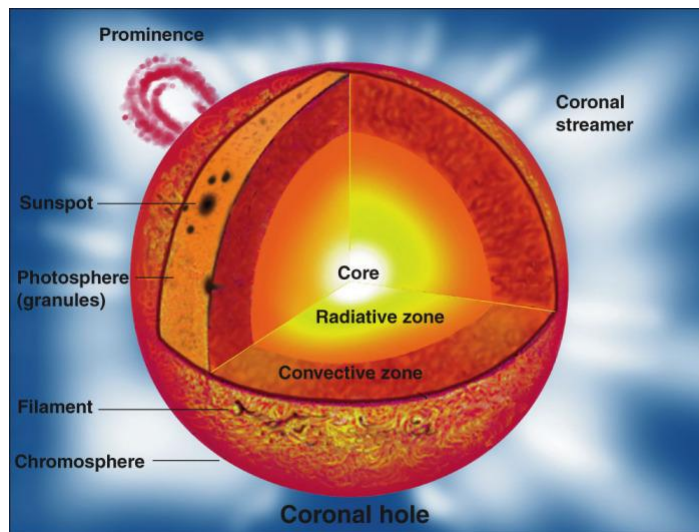


Figure 4.1: *Schematic view of the sun [Ifa08]. The structure of the sun can be divided into several layers: the core, the radiative zone, the convective zone, the photosphere, the chromosphere and the corona.*

The sun can be segregated into different layers as can be seen in Figure 4.1. Beginning from the interior, there is the core where the density is the highest at a temperature of approximately $1.56 \cdot 10^7$ K [Scm97]. It has a radius of $\sim 0.2 R_{\odot}$. Next is the radiative zone ($\sim 0.2 R_{\odot} - 0.7 R_{\odot}$), where the gas is an ionized plasma and the energy transport is achieved entirely through radiation. The next layer is the convective zone. Here the solar plasma is not dense and hot enough to transfer the energy of the interior outward via radiation. As a result, thermal convection occurs

as thermal columns carry hot material to the surface of the sun. Once the material cools off at the surface, it plunges back downward to the base of the convection zone and receives more heat from the top of the radiative zone. The convective zone stretches from $\sim 0.7 R_{\odot}$ up to the surface, the photosphere. The photosphere is the border from where visible sunlight is free to propagate into space and its energy escapes the sun entirely. The change in opacity is due to the decreasing amount of H^{-} ions, which absorb visible light to a high extent. Below the photosphere the gas is opaque. Above the photosphere is the chromosphere, a thin layer of the Sun's atmosphere just above the photosphere, $\sim 10^4$ km deep. It has a red colour due to the Balmer H – α emission line, which is the origin of its name. The outermost layer is the corona, where the gas is heated to temperatures beyond 10^6 K through a mechanism that has not been fully understood yet, but two theories seem most plausible: the wave heating theory and the magnetic reconnection theory [Asc04] [Alf47]. Some important facts about the sun are listed in Table 4.1.

Parameter	Value
Age	$4.6 \cdot 10^9$ yr
Radius R_{\odot}	$6.96 \cdot 10^5$ km
Mass M_{\odot}	$1.99 \cdot 10^{30}$ kg
Mean density	1.41 g cm^{-3}
Density at center	148 g cm^{-3}
Temperature at center	$1.56 \cdot 10^7$ K
Surface temperature	$5.78 \cdot 10^3$ K
Luminosity	$2.41 \cdot 10^{39} \text{ MeV sec}^{-1}$
Composition (% of mass)	
Hydrogen H	73.46 % [Edd79]
Helium He	24.85 % [Edd79]
Heavy elements ($Z > 2$)	1.69 % [Edd79]
Mean distance to earth	$1.496 \cdot 10^8$ km
ν_e flux density on earth	$6.52 \cdot 10^{10} \text{ cm}^{-2} \text{ sec}^{-1}$ [Bah05]
Total ν_e flux produced in the sun	$1.87 \cdot 10^{38} \text{ sec}^{-1}$

Table 4.1: *The solar parameters [Scm97]*

The dynamics of the sun is described through the so called Standard Solar Model (SSM) [Bah05]. It takes the fusion processes into account and assumes a thermal equilibrium (energy production = energy radiation) within the sun. It treats the sun as an ideal gas using the four equations of stellar dynamics [Scm97].

4.2 The solar fusion cycles

An overview over all fusion reactions and the corresponding neutrino energies and fluxes is given in the Table 4.2. All values are based upon BS05(OP) (Bahcall-Serenelli model 2005 with new solar opacities, see [Bah05]).

Process	short notation	neutrino energy E_ν [MeV]	ν_e flux on earth after BS05(OP) [$10^{10} \text{ cm}^{-2} \text{ sec}^{-1}$]
$p + p \rightarrow {}^2\text{H} + e^+ + \nu_e$	pp	≤ 0.420	5.99 ± 0.06
$p + e^- + p \rightarrow {}^2\text{H} + \nu_e$	pep	1.442	$(1.42 \pm 0.03) \cdot 10^{-2}$
${}^3\text{He} + p \rightarrow {}^4\text{He} + e^+ + \nu_e$	hep	≤ 18.773	$(7.93 \pm 1.27) \cdot 10^{-7}$
${}^7\text{Be} + e^- \rightarrow {}^7\text{Li} + \nu_e$	${}^7\text{Be}$	0.862(90 %); 0.384(10 %)	$(4.88 \pm 0.53) \cdot 10^{-1}$
${}^8\text{B} \rightarrow {}^8\text{Be} + e^+ + \nu_e$	${}^8\text{B}$	≤ 14.6	$(5.69 \pm 0.91) \cdot 10^{-4}$
${}^{13}\text{N} \rightarrow {}^{13}\text{C} + e^+ + \nu_e$	${}^{13}\text{N}$	≤ 1.199	$(3.07 \pm 0.01) \cdot 10^{-2}$
${}^{15}\text{O} \rightarrow {}^{15}\text{N} + e^+ + \nu_e$	${}^{15}\text{O}$	≤ 1.732	$(2.33 \pm 0.01) \cdot 10^{-2}$
${}^{17}\text{F} \rightarrow {}^{17}\text{O} + e^+ + \nu_e$	${}^{17}\text{F}$	≤ 1.740	$(5.84 \pm 0.01) \cdot 10^{-4}$
		Total	6.60 ± 0.07

Table 4.2: *The different fusion chains in the sun, using the values of the BS05(OP) solar model from Bahcall-Serenelli, see also Figure 4.3*

4.2.1 pp chain

98.4 % of the suns energy radiation (the other 1.6 % are produced by the CNO cycle) is produced via the exothermic thermonuclear fusion reaction of hydrogen to helium in the reaction



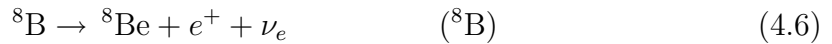
In this reaction a netto energy of 26.73 MeV is set free. The mean energy of the two released neutrinos is only $2\langle E_\nu \rangle = 0.59$ MeV, while the rest is thermal energy, which is transported via charged particles or photons. There are two reactions of the pp chain producing ν_e :



The first reaction produces the pp neutrinos, which have the highest flux on earth (see Table 4.2). Because there are three products, the energy is continuously distributed, resulting in a spectral energy shape of the neutrinos (see Figure 4.3). The second reaction produces the pep neutrinos, which are monoenergetic with $E_\nu = 1.442 \text{ MeV}$. Due to only two products of the reaction, the products of the reaction have discrete energies. Almost the whole neutrino flux on earth consists of the pp neutrinos ($5.94 \cdot 10^{10} \text{ cm}^{-2} \text{ sec}^{-1}$). The flux of the pp neutrinos is well known (the uncertainty is below 1%, because it depends weakly on the core temperature ($\Phi(\nu_{pp}) \sim T^{-1.2}$)).

4.2.2 hep, ${}^7\text{Be}$ and ${}^8\text{B}$ chains

The three reactions



are sub-cycles of the pp chain. After the pp neutrino flux, the ${}^7\text{Be}$ reaction delivers the second highest neutrino flux. As the pep neutrinos, the ${}^7\text{Be}$ neutrinos are monoenergetic. As can be seen in Table 4.2, the ${}^7\text{Be}$ neutrinos consist of two monoenergetic parts, one with $E_\nu = 0.862 \text{ keV}$, which makes up 90% of the ${}^7\text{Be}$ neutrino flux, the remaining part with $E_\nu = 0.384 \text{ keV}$ ¹¹. The hep and ${}^8\text{B}$ chains reach up to higher neutrino energies of 14.6 MeV and 18.773 MeV, respectively, but they have significantly lower fluxes. Figure 4.2 shows their relation to the pp cycle.

¹¹The two energy values for the ${}^7\text{Be}$ neutrinos derive from the ground state and the excited state of ${}^7\text{Li}$

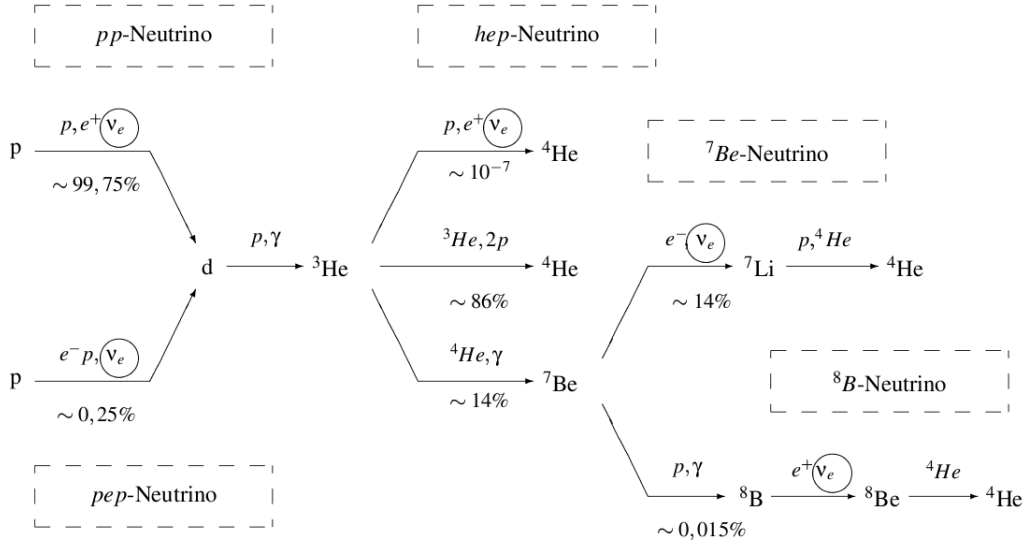


Figure 4.2: The pp cycle and the relation to the hep , ${}^7\text{Be}$ and ${}^8\text{B}$ chains, from [MPK]

4.2.3 CNO chain

The CNO-I cycle (the CNO-II, CNO-III and CNO-IV subcycles play only a role in very massive stars) consists of several reactions of which three produce neutrinos:



This cycle makes up to only $\sim 1.6\%$ of the suns energy production. Theoretical models show that the CNO cycle is the dominant source of energy in stars heavier than the sun at temperatures above $1.8 \cdot 10^7$ K [Mei08]. The proton-proton chain is more important in stars with the mass of the sun or less. Figure 4.3 illustrates the CNO-I cycle.

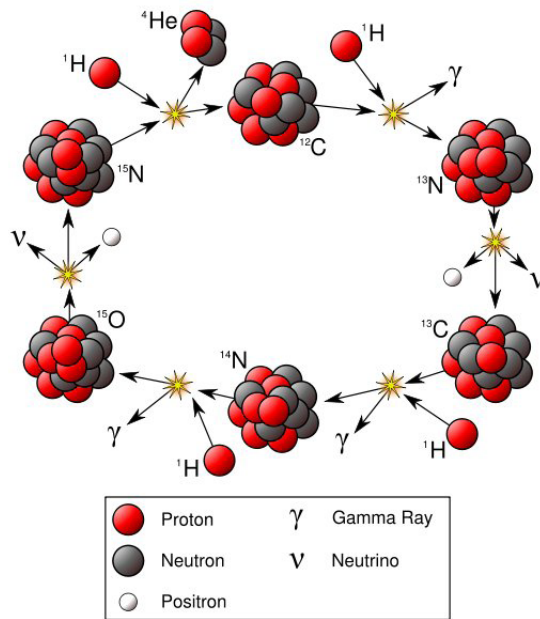


Figure 4.3: *Schematics of the CNO-I cycle [Mei08].*

Figure 4.4 shows the energy dependant flux of the solar neutrinos of all fusion reactions combined into one plot according to calculations based on the Standard Solar Model.

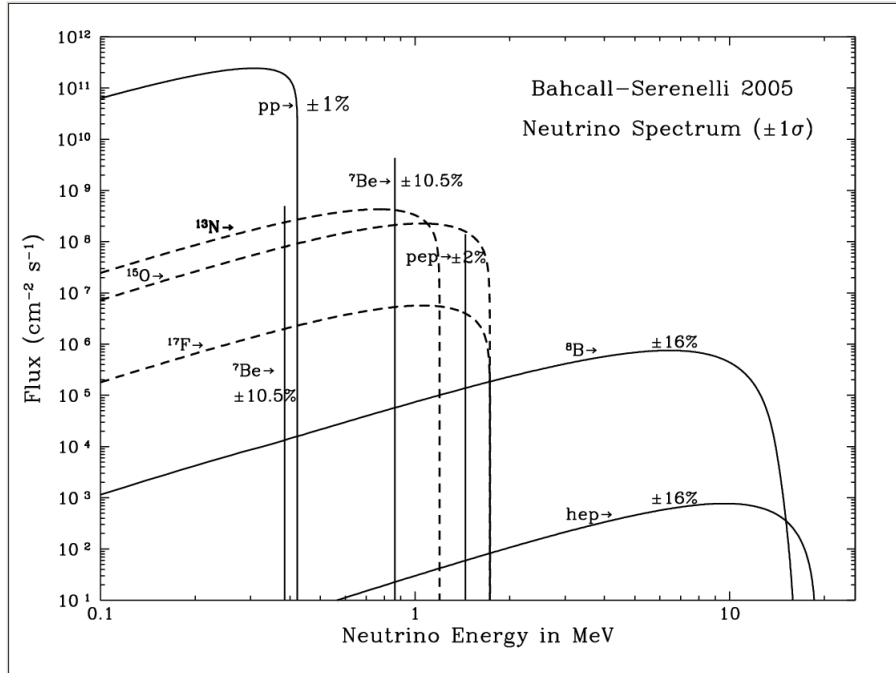


Figure 4.4: *The solar neutrino spectrum based upon calculations from Bahcall and Serenelli (2005) [Bah05]*

4.3 Solar matter density fluctuations

4.3.1 P modes and helioseismology

Solar matter density fluctuation is a phenomenon, that has already been known since the 1960s and has been studied by several experiments [Gon] [DG89]. These so called *pressure modes* have their origin within the convective zone of the sun. They are excited due to acoustic waves, which are emitted by turbulent convection. They reach throughout the convective zone up to the surface. There they can be analyzed by measuring the velocity field of the gas on the solar surface by means of doppler spectroscopy. The modes have periods of about 3-12 minutes and a lifetime of days to sometimes months. Pressure waves can be viewed as standing waves within the sun, where the sun acts as a resonance body. The individual normal modes of the sun are identified by three numbers, analogous to the energy states of the hydrogen atom. These are the spherical harmonic degree l , azimuthal order m , and the number of modes in the radial direction, n . Figure 4.5 shows the velocity field of the sun for a P mode oscillation with $l=20$, $m=16$ and $n=14$.

These oscillations can be used to gain additional insight into the solar structure and

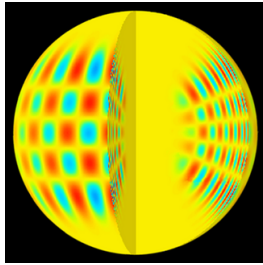


Figure 4.5: A graphical illustration of a P mode oscillation with $l=20$, $m=16$ and $n=14$ as it would occur in the sun [Ifa08]

can be viewed as a good test for the Standard Solar Model (SSM). They have been found to be in excellent agreement with the theoretical expectations. Thus, helioseismology, together with neutrino detection, is a good tool for the investigation of the interior of the sun. Much of the knowledge about the structure of the sun is based upon helioseismological observations. According to [BBM98], the P modes however do not have the necessary prerequisites to affect the neutrino survival probability via the MSW effect, because they have a too small amplitude.

4.3.2 Magneto-gravity modes

Another possible process which leads to the creation of density fluctuations in the sun are so called *magnetic driven gravity modes* (G modes). In contrast to the previously mentioned P modes, it is thought that they have their origin in a strong magnetic field within the radiative zone of the sun [Bur03c]. The strength of this magnetic field is unknown, but an upper limit is set, because as was already stated by Chandrasekhar, the field energy should be less than the gravitational energy [Bur03c] (which corresponds to $B_{rad.zone} \leq 10^4$ T). The implication on neutrino physics is, that for a given oscillation length and amplitude, they could have a significant impact on the MSW flavour conversion in the sun, which could be measured in neutrino detectors. A complete deduction of the eigenfrequencies of G mode oscillations can be found in [Bur03a]. An exponential density profile of the form $\rho_0(r) = \rho_c \cdot \exp(\frac{-r}{H})$ is being assumed, with ρ_c being the density in the center of the sun, ρ_0 the average radial density and H the density height scale (here $H = const \sim 0.1R_\odot$). The eigenmode problem is solved using the four equations for stellar hydrodynamics in presence of magnetic fields for small perturbations of several percent above the average matter density [Bur03b].

In order to have an effect on the MSW neutrino flavour conversion, the G modes should have a wavelength or correlation length (L_{corr}) in the order of the MSW resonance length [Bur03a]:

$$L_{res}^{osc} = \frac{250km(\frac{E}{MeV})}{\frac{\Delta m^2}{10^{-5}eV^2} \sin(2\theta)} \sim L_{corr} \quad (4.10)$$

For a 10 MeV ^8B neutrino for example, the resonance length for $\nu_e \rightarrow \nu_\mu$ is ~ 337 km. As can be seen in figure 4.6, a field of approximately 10 T, would yield a correlation length of about 300 km for ~ 0.15 and ~ 0.5 solar radii, respectively. The radiative zone stretches, as was mentioned, from 0.2 to 0.7 solar radii, thus a 1 Tesla field at 0.5 solar radii would deliver the necessary correlation length in order to alter the MSW-LMA survival probability in a significant way.

G modes could also lead to changes of the temperature at the production region of neutrinos [Bur03b]. These would result in a change of the neutrino production rate and thus in an oscillation of the neutrino flux. Such fluctuations of the neutrino flux are analyzed in chapter 5.4 with ^7Be neutrinos in LENA, because they offer the best statistics. Figure 4.7 shows the effect of G modes on the MSW-LMA survival probability of neutrinos produced in the sun in dependence of the amplitude of the modes.

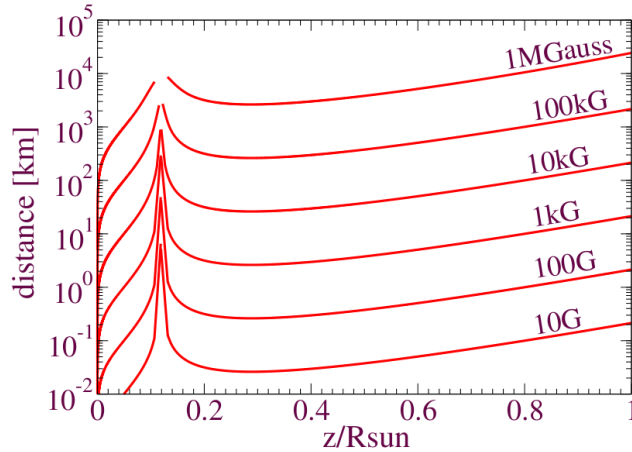


Figure 4.6: *The wavelength or correlation length of G modes depends on the strength of the magnetic field in the radiative zone and on the radial distance z from the center of the sun. For a 10 MeV ^8B neutrino, a wavelength of 337 km would be needed, which is approximately sufficed for a field of 10 T in the radiative zone at ~ 0.5 solar radii. From [Bur03b]*

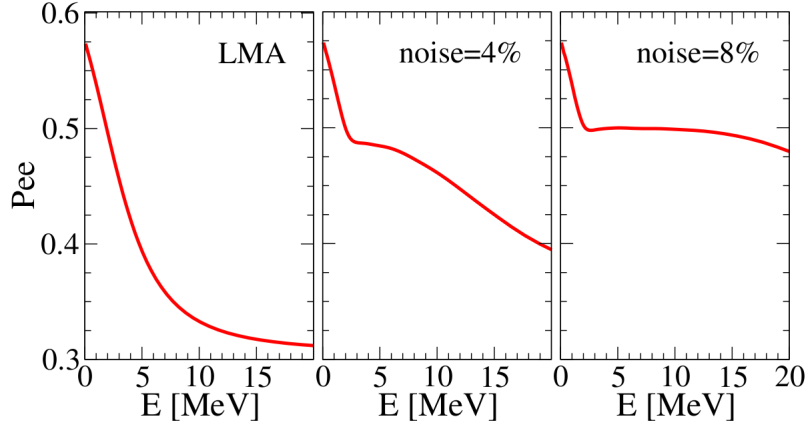


Figure 4.7: *The effect of random solar matter density fluctuations on electron neutrino survival probability for MSW-LMA oscillations and a correlation length $L_0 = 100$ km. The amplitude of the fluctuations at the position of neutrino resonance is zero in the left panel, and is 4 % and 8 % of the mean density of the solar matter in the middle and right panels, respectively [Bur03b]*

Already for an amplitude of 4 % of the mean density, a significant alteration of the MSW-LMA curve takes place. The higher the amplitude, the more the large mixing angle survival probability differs from the non perturbed MSW-LMA solution. Such a changed survival probability would have a significant impact on the event rates in a neutrino detector. A detector as LENA with its high statistics should be able to set very precise limits for the oscillation parameters of such G modes. In Chapter 5.4, the possible implications of G modes on the ${}^7\text{Be}$ neutrino flux with its high event rates is studied and limits for the amplitude and cycle duration of G modes are presented.

Chapter 5

Measurement of solar neutrinos with LENA

As was already mentioned in chapter 3, the measurement of solar neutrinos with a detector such as LENA would offer a very statistics, and thus enable very accurate precision measurements of solar neutrino fluxes, which are strongly correlated with the solar parameters of the standard solar model. In the first section of this chapter, the event rates for the solar neutrinos from all the different fusion chains will be calculated. After that, the energy spectra of the solar neutrinos, as will be seen in LENA are presented and possible background contributions from diverse sources are discussed and the background rates for the most relevant sources are calculated. Also, factors such as quenching and a qualitative plot with the different background contributions in a large PXE based liquid-scintillator will be discussed. The next section covers an analysis of the influence of the MSW effect on ^8B neutrinos in LENA, with the goal of investigating the effectivity of LENA for proving the existence of the MSW curve in the 2-3 MeV regime, then a discussion of the results follows. The last analysis will be the detectability of possible fluctuations of the ^7Be neutrinos caused by magneto gravity modes in the radiative zone of the sun (see chapter 4), and an exclusion plot will be shown which corners the detectable regions of such flux variations for LENA.

5.1 Estimation of event rates for solar neutrinos in LENA

5.1.1 Reaction rate

The reaction rate for elastic neutrino scattering off electrons is given by

$$R_{electron} = n \cdot \Phi \cdot \int_0^\infty dT \int_{E_\nu}^\infty dE'_\nu \cdot \lambda(E'_\nu) \cdot P_{ee}(E'_\nu) \cdot \frac{d\sigma(E'_\nu, T)}{dT} \quad (5.1)$$

where n is the amount of target particles, in this case electrons within the fiducial volume of LENA ($n = 1.45 \cdot 10^{34}$ [Mar05]), Φ the solar neutrino flux on earth, E_ν the energy of the incoming neutrino, T the kinetic recoil energy of the electron, $\frac{d\sigma(E_\nu, T)}{dT}$ the differential cross-section for elastic neutrino-electron scattering, P_{ee} the neutrino survival probability and $\lambda(E_\nu)$ is the spectral shape of the neutrino flux (See Fig. 4.4). The reaction rate itself depends on the recoil energy of the electron and on the energy of the incoming neutrino. This is also the formula needed when calculating the recoil spectra later on.

Differential cross-section

The differential cross section is given by [Fer02]

$$\frac{d\sigma}{dT}(E_\nu, T) = \frac{G_F^2 M_e}{2\pi E_\nu^2} [(c_V + c_A)^2 E_\nu^2 + (c_V - c_A)^2 (E_\nu - T)^2 - (c_V^2 - c_A^2) M_e T] \quad (5.2)$$

where G_F is the Fermi coupling constant, M_e is the mass of the electron, and c_V and c_A are the vector- and the axialvector coupling constants of the weak interaction theory. For $\nu_e + e^-$ scattering they are given by $c_V = 1$; $c_A = 0.5$, and for $\nu_{\mu, \tau} + e^-$ they are given by $c_V = -0.02$; $c_A = -0.5$ [Per].

Thus, the cross section differs for the channel $\nu_e + e^-$ and $\nu_{\mu, \tau} + e^-$.

The total cross sections for ν_e and $\nu_{\mu, \tau}$ are linear to the neutrino energy [Cad02]:

$$\sigma_{\nu_e} = 9.2 \cdot 10^{-45} \frac{E}{\text{MeV}} \text{ cm}^2 \quad (5.3)$$

$$\sigma_{\nu_{\mu, \tau}} = 1.57 \cdot 10^{-45} \frac{E}{\text{MeV}} \text{ cm}^2 \quad (5.4)$$

The total cross section for ν_e is 5.86 times higher than for $\nu_{\mu, \tau}$ ¹², thus the rate of μ - and τ -neutrinos is suppressed. This was also considered for the calculation of the event rates.

Because the elastic scattering of a neutrino off an electron follows the same principle as Compton scattering of a photon with an electron, the kinetic recoil energy of the electron suffices the constraint

$$T \leq \frac{2E_\nu^2}{M_e + 2E_\nu} \quad (5.5)$$

¹²Because electron neutrinos can additionally interact via charged current

The neutrino energy then must exceed the threshold

$$E_\nu \geq (2T \pm \sqrt{4T^2 + 8TM_e}) \cdot \frac{1}{4} \quad (5.6)$$

with the minus sign being ignored, because it could deliver negative neutrino energies. This condition will be used when calculating the event rate and recoil spectrum using (5.2).

Survival probability and MSW effect

As was shown in chapter 2.2.2, the MSW effect changes the survival probability of an electron neutrino produced in the sun dependant on the energy (see figure 1.1). If the ν_e which is produced in the sun, does not change its flavour due to the MSW effect, the rate is given by

$$R_{electron,\nu_e} = n \cdot \Phi \cdot \int_0^\infty dT \int_{E_\nu}^\infty dE'_\nu \cdot \lambda(E'_\nu) \cdot P_{ee}(E'_\nu) \cdot \frac{d\sigma(E'_\nu, T)_e}{dT} \quad (5.7)$$

with the cross section for $\nu_e + e^-$ scattering.

In case of an oscillation $\nu_e \rightarrow \nu_{\mu,\tau}$, the event rate becomes

$$R_{electron,\nu_{\mu\tau}} = n \cdot \Phi \cdot \int_0^\infty dT \int_{E_\nu}^\infty dE'_\nu \cdot \lambda(E'_\nu) \cdot (1 - P_{ee}(E'_\nu)) \cdot \frac{d\sigma(E'_\nu, T)_{\mu,\tau}}{dT} \quad (5.8)$$

with the cross section for $\nu_{\mu,\tau} + e^-$.

The spectra $\lambda(E_\nu)$ for the ^{13}N , ^{15}O , ^{17}F , ^8B , hep and pp neutrinos were taken from [SNS], they are also based upon the BS05(OP) solar model and are publically accessible.

5.1.2 Results for the event rates

The channel $\nu_{e,\mu,\tau} + e^- \rightarrow e^- + \nu_{e,\mu,\tau}$

All the following results were calculated for 18 kt fiducial volume and are shown in the Table 5.1. The rate for ν_e and $\nu_{\mu,\tau}$ were calculated separately and then added to get the total event rate. For the calculation of the values, an integration over T and E_ν was done (with the constraints (5.5) and (5.6)) using the survival probability, the neutrino spectra, the differential cross sections, the restriction for the recoil energy of the electron, the overall neutrino flux and the number of electrons in the fiducial volume of LENA. The threshold energy of LENA is aimed at 200 keV-250 keV. Thus the calculation was performed for 200 keV and 250 keV, respectively. The uncertainties are also from the BS05(OP) model.

$E_{thr} = 200 \text{ keV}$

Neutrino sort	Total Event Rate ($\nu_{e,\mu,\tau}$)
${}^7\text{Be}$	$(5.391 \pm 0.566) \cdot 10^3 \text{ d}^{-1}$
pep	$(389 \pm 6) \text{ d}^{-1}$
pp	$(844 \pm 8) \text{ d}^{-1}$
${}^8\text{B}$	$(2.8399 \pm 0.4544) \cdot 10^4 \text{ yr}^{-1}$
hep	$(60 \pm 10) \text{ yr}^{-1}$
CNO	$(656 \pm 1) \text{ d}^{-1}$

$E_{thr} = 250 \text{ keV}$

Neutrino sort	Total Event Rate ($\nu_{e,\mu,\tau}$)
${}^7\text{Be}$	$(4.763 \pm 0.500) \cdot 10^3 \text{ d}^{-1}$
pep	$(368 \pm 6) \text{ d}^{-1}$
pp	$(25 \pm 0) \text{ d}^{-1}$
${}^8\text{B}$	$(2.8076 \pm 0.4492) \cdot 10^4 \text{ yr}^{-1}$
hep	$(60 \pm 10) \text{ yr}^{-1}$
CNO	$(585 \pm 1) \text{ d}^{-1}$

Table 5.1: *Expected event rates R for solar neutrinos in LENA for a threshold energy of $E_{thr} = 200 \text{ keV}$, 250 keV , respectively, for the elastic neutrino-electron scattering channel*

The ${}^{13}\text{C}$ channels

For neutrino energies above $E_{thr} = 2.22 \text{ MeV}$, the channel $\bar{\nu}_e + {}^{13}\text{C} \rightarrow {}^{13}\text{N} + e^-$ becomes relevant, especially for the detection of ${}^8\text{B}-\nu$. Above $E_{thr} = 3.68 \text{ MeV}$, $\nu_x + {}^{13}\text{C} \rightarrow {}^{13}\text{C}^* + \nu_x$ plays an additional role. In order to estimate the event rate, the number of ${}^{13}\text{C}$ atoms in the fiducial volume of LENA has to be calculated. The natural abundance of ${}^{13}\text{C}$ is 1.1% [Hol95]. The number of protons bound in ${}^{12}\text{C}$ in 18 kt volume is $1.22 \cdot 10^{34}$ [Mar05]. Thus, the number of ${}^{13}\text{C}$ is $n_{13\text{C}} = \frac{1}{6} \cdot 0.011 \cdot 1.22 \cdot 10^{34} = 2.03 \cdot 10^{31}$. With the cross section for this reaction, taken from [Ian05], the event rate can be calculated. The result is $(R = 610 \pm 98) \text{ yr}^{-1}$ for $E_{thr} = 200 \text{ keV}$ and the same for $E_{thr} = 250 \text{ keV}$, as the intrinsic threshold of the reaction channels is 2.22 MeV and 3.68 MeV, respectively.

5.1.3 The electron recoil spectra

The electron recoil spectrum is described by the differential form of equation (5.1), which can be written as

$$\frac{dR}{dE_\nu dT} = n \cdot \Phi \cdot \lambda(E_\nu) \cdot P_{ee}(E_\nu) \cdot \frac{d\sigma(E_\nu, T)}{dT} \quad (5.9)$$

A physical detector however, has a finite energy resolution. The energy resolution of LENA can be approximated to be $\frac{\sqrt{180pe}}{180pe} = 7.45\%$ at 1 MeV [Mar05]. This can

also be approximated as $\frac{\sigma(E)}{E} = 0.1 \cdot \left(\frac{E}{\text{MeV}}\right)^{-\frac{1}{2}}$ [Nef05]. This however, is only an estimation, and the actual resolution in the finished detector could differ from that value. In order to calculate the recoil spectrum with the energy resolution of LENA, the differential rate has to be convoluted with a gaussian function of the form:

$$G(T - E_\nu) = \frac{1}{\sqrt{2\pi}\sigma} \exp\left(-\frac{1}{2} \cdot \frac{T - E_\nu}{\sigma^2}\right) = \frac{1}{0.1 \cdot \sqrt{2T}\pi} \exp\left(-\frac{1}{2} \cdot \frac{T - E_\nu}{(0.1)^2 T}\right) \quad (5.10)$$

The differential rate for the calculation of the electron recoil spectrum with the energy resolution of the detector is given through

$$\frac{dR}{dE_\nu} = n \cdot \Phi \int_{-\infty}^{\infty} dT \cdot \lambda(E'_\nu) \cdot P_{ee}(E'_\nu) \cdot G(T - E'_\nu) \cdot \frac{d\sigma(E'_\nu, T)}{dT} \quad (5.11)$$

The results for all solar neutrinos are shown in figure 5.1. It was summarized over the event rates of all neutrino flavours, and the total event rate is drawn also. The first plot covers the whole spectrum up to recoil energies of 16 MeV, for the high energetic hep- ν channel. The higher energetic solar neutrinos were already measured in detail, thus the interesting lower energy region up to 2 MeV is drawn separately. The spectrum files were taken from [SNS].

5.2 Background sources

The main background sources for solar neutrinos in LENA are radionuclides. A part of them are myon-induced radionuclides¹³ such as ^{11}C and ^{10}C , which are the main cosmogenic background for solar neutrinos. The other part are radionuclides from the Uranium and Thorium decay chains, which are abundant in the surrounding rock, and also radionuclides that are abundant in the liquid-scintillator itself, for example ^{14}C or decay products of Radon.

¹³Cosmogenic radionuclides

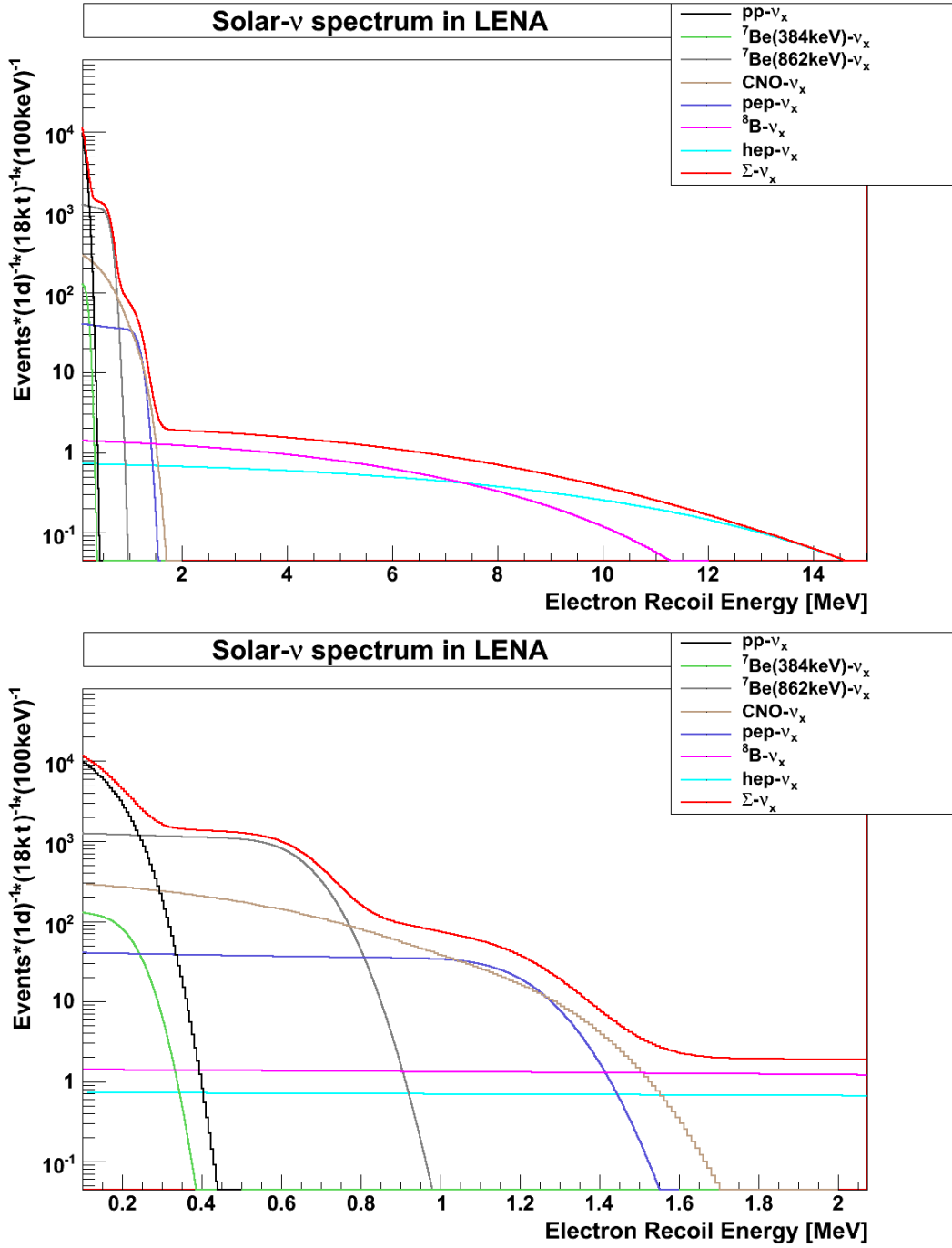


Figure 5.1: The whole electron recoil spectrum from solar neutrinos up to 16 MeV in the upper plot, and up to 2 MeV in the lower plot, respectively, as would be seen in LENA (fiducial volume 18 kt). The event rates for the different neutrino channels are the sum of all neutrino flavours $\nu_{e,\mu,\tau}$ and the red line represents the overall rate for all neutrino channels.

5.2.1 Reactor antineutrinos and atmospheric neutrinos

A possible background source are for example atmospheric neutrinos. The lowest energetic atmospheric neutrinos begin at about 14 MeV with fluxes of $\sim 1 \text{ MeV}^{-1} \text{ yr}^{-1}$ [Wur05], while only the highest energetic solar neutrinos are in this energy regime. Thus this background source can be neglected.

Another possible background source are reactor-antineutrinos, that are constantly produced in nuclear power plants. The integrated rate for LENA at Pyhäsalmi has been estimated to $(7.56 \pm 1.06) \cdot 10^3 (18 \text{ kt})^{-1} \text{ yr}^{-1}$ and $(4.14 \pm 0.58) \cdot 10^3 (18 \text{ kt})^{-1} \text{ yr}^{-1}$ for Pylos, respectively [Wur05] for the reaction channel $\bar{\nu}_e + p \rightarrow n + e^+$ (See Table 3.1).

The shape of the reactor-antineutrino, and of the atmospheric neutrino spectrum is shown in figure 5.2. By the delayed coincidence of the positron and the neutron in this reaction, this background can be identified clearly. Additionally, the fluxes are significantly lower than the fluxes of solar neutrinos. Thus, this background can be neglected.

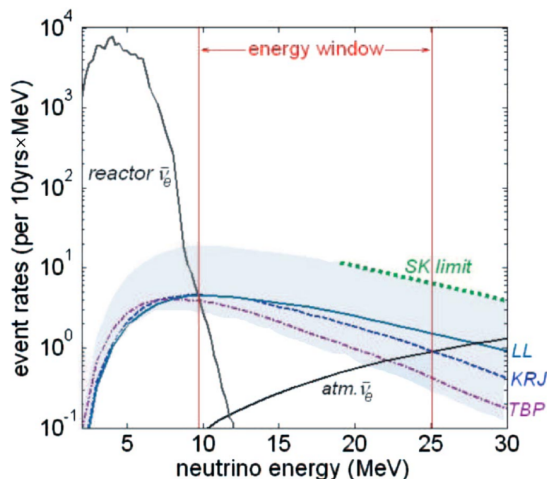


Figure 5.2: *Atmospheric neutrino and reactor-antineutrino background in LENA (for a 50 kt volume), from [Wur05].*

5.2.2 Background from radionuclides

There are several radionuclides abundant in a liquid-scintillator or in the detector volume itself. In order to minimize the background levels, so that the signal to background ratio is improved, a high radiopurity is necessary for such a detector. Purification methods can be found in [Ang05]. The main radionuclides in a liquid-scintillator detector that contribute to the background are enlisted in Table 5.2, the data is for the Borexino detector and is also taken from [Ang05]. The values for PXE and PC are based upon data acquired by the counting test facility (CTF).

Isotope	Source	Typical Concentration	Tolerable Level
^{14}C	radiogenic	$1.2 \cdot 10^{-12}$ g/g in living organic material	$3 \cdot 10^{-18}$ g/g (PC) [Ang05] $9 \cdot 10^{-18}$ g/g (PXE) [Hag00]
^{222}Rn	air, emanation from materials	150 Bq/m ³ at LNGS	$0.1 \mu\text{Bq/m}^3$ (PC) [Ang05]
^{210}Bi ^{210}Po	^{210}Pb	$5 \cdot 10^2$ ev/d/T	0.5 ev/d/T [Ang05]
^{238}U ^{232}Th	suspended dust	$2 \cdot 10^{-5}$ g/g in dust	$< 1 \cdot 10^{-15}$ g/g (PXE) [Hag00]
^{40}K	dust or fluor contamination	$2 \cdot 10^{-6}$ g/g	$< 10^{-14}$ g/g in scintillator [Ang05]
^{39}Ar ^{85}Kr	air	0.1 Bq/m ³ in air	$0.1 \mu\text{Bq/m}^3$ (PC) [Hag00]

Table 5.2: *The main radioactive background sources in a liquid-scintillator detector, taken from [Ang05]. The values for PXE and PC are based upon data taken by the Borexino Counting Test Facility (CTF) [Hag00]*

5.2.3 Cosmogenic radionuclides

Cosmogenic radionuclides are constantly produced by atmospheric muons in a detector. When an atmospheric muon hits the surrounding material of the detector, an electromagnetic or hadronic cascade is produced, mainly consisting of γ -rays, electrons, neutrons, protons and π mesons. By interacting with the scintillator mass, the muon and its secondaries can produce radioactive nuclides within the detector. The main cosmogenic radionuclides of interest are ^{10}C and ^{11}C , which are produced by neutron capturing.

The myon flux at Pyhäsalmi is $\Phi_{\mu}^{LENA} = (1.1 \pm 0.1) \cdot 10^{-4} \text{m}^{-2} \text{s}^{-1}$. This value was taken from [Enq05]. The mean energy of a muon at Pyhäsalmi can be estimated to $\langle E_{\mu}^{LENA} \rangle = 304 \text{GeV}$ assuming a water equivalent of 4 km and standard soil [Kud03].

In order to get the neutron production rate for LENA, the well known neutron production rate of Borexino was scaled up to the volume of LENA.

The mean muon energy at LNGS where Borexino is situated (3800 m.w.e) is $\langle E_\mu^{BX} \rangle = 320 \pm 4_{stat.} \pm 11_{sys.}$ GeV [Hag00]. The muon flux is $\Phi_\mu^{BX} = (3.2 \pm 0.25) \cdot 10^{-4} \text{ m}^{-2} \text{ s}^{-1}$. Thus, the neutron production rate which is directly proportional to the abundance of ^{10}C and ^{11}C , can be estimated for LENA using the Borexino data through

$$\frac{R(^{11}\text{C} \& ^{10}\text{C}, BX)}{R(^{11}\text{C} \& ^{10}\text{C}, LENA)} \sim \frac{\Phi_\mu^{BX} \cdot \langle E_\mu^{BX} \rangle^{0.7} \cdot M_{BX}}{\Phi_\mu^{LENA} \cdot \langle E_\mu^{LENA} \rangle^{0.7} \cdot M_{LENA}} \quad (5.12)$$

$$\begin{aligned} \implies R(^{11}\text{C} \& ^{10}\text{C}, LENA) &= R(^{11}\text{C} \& ^{10}\text{C}, BX) \cdot \left(\frac{1.1}{3.2}\right) \cdot \left(\frac{304}{320}\right)^{0.7} \cdot \left(\frac{18\text{kt}}{0.1\text{kt}}\right) = \\ &59.7 \cdot R(^{11}\text{C} \& ^{10}\text{C}, BX) = 59.7 \cdot (29 \pm 1) \text{ d}^{-1} = (1732 \pm 60) \text{ d}^{-1} \end{aligned} \quad (5.13)$$

5.2.4 Background rates

The background rates for the relevant radionuclides are listed in Table 5.3. The values for LENA were upscaled with the assumption that LENA would have a similar radiopurity like Borexino, using the values from [Bx08a] and [Smi08].

Isotope	Rate in Borexino	Estimated rate in LENA
^{14}C	$2.0 \cdot 10^6 \text{ d}^{-1} (0.1 \text{ kt})^{-1}$	$3.6 \cdot 10^9 \text{ d}^{-1} (18 \text{ kt})^{-1}$
^{210}Po	$(882 \pm 3) \text{ d}^{-1} (0.1 \text{ kt})^{-1}$	$(1.5876 \pm 0.0054) \cdot 10^5 \text{ d}^{-1} (18 \text{ kt})^{-1}$
$^{210}\text{Bi} + \text{CNO}$	$(23 \pm 2) \text{ d}^{-1} (0.1 \text{ kt})^{-1}$	$(4140 \pm 360) \text{ d}^{-1} (18 \text{ kt})^{-1}$
^{85}Kr	$(25 \pm 3) \text{ d}^{-1} (0.1 \text{ kt})^{-1}$	$(4500 \pm 540) \text{ d}^{-1} (18 \text{ kt})^{-1}$
^{214}Pb	$0.92 \text{ d}^{-1} (0.1 \text{ kt})^{-1}$	$166 \text{ d}^{-1} (18 \text{ kt})^{-1}$
^{10}C	$4 \text{ d}^{-1} (0.1 \text{ kt})^{-1}$	$239 \text{ d}^{-1} (18 \text{ kt})^{-1}$
^{11}C	$(25 \pm 1) \text{ d}^{-1} (0.1 \text{ kt})^{-1}$	$(1493 \pm 60) \text{ d}^{-1} (18 \text{ kt})^{-1}$

Table 5.3: *The total background rates for the main radionuclides that are relevant for solar neutrinos. The data was taken from [Smi08], [Bx08a], and the values for LENA are upscaled on its fiducial volume of 18 kt. For the cosmogenic radionuclides (^{10}C and ^{11}C), the production rate was estimated using further knowledge of the myon flux and average myon energy at Pyhäsalmi.*

Figure 5.3 shows the summarized solar neutrino spectrum together with the radioactive background. The decay spectra were calculated using the upscaled values of the Borexino data (see Table 5.3), the decay energies of the isotopes, and the type of decay. In order to plot the spectrum with background, another effect in liquid-scintillators has to be taken into account, which is the quenching. The quenching is described through the semi-empirical Birks' formula [Win07]:

$$\frac{dE_{equiv}}{dx} = \frac{A \cdot \frac{dE}{dx}}{1 + k \cdot \frac{dE}{dx}} \quad (5.14)$$

with $\frac{dE_{equiv}}{dx}$ being the light output per unit length with respect to an electron, $\frac{dE}{dx}$ the energy loss according to the Bethe-Bloch law, A the absolute scintillation efficiency and k a factor that relates the density of ionisation centres to $\frac{dE}{dx}$. PXE has $k = 0.015$ cm/MeV, while for PC it is $k = 0.017$ cm/MeV ([Smi08]), thus the quenching is higher for PC than for PXE. This was also considered for LENA, meaning that the background curves are qualitatively shifted to the right by the factor $\frac{0.017}{0.015}$ in comparison to PC. The data was then scaled up to the mass of LENA using again the data from [Smi08].

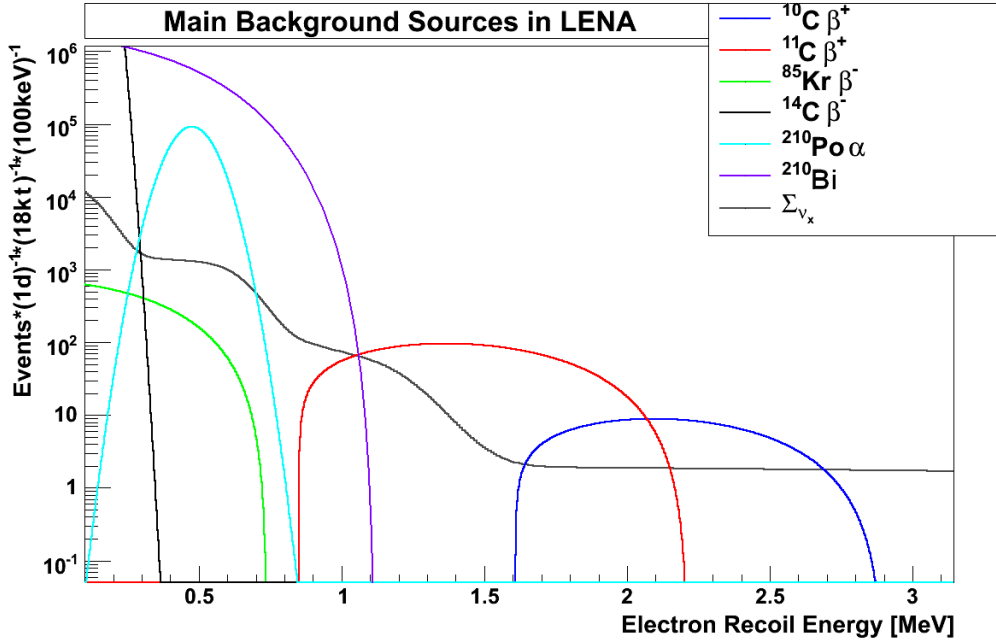


Figure 5.3: *This plot shows qualitatively the estimated background rates in LENA for one day of measurement time, assuming a similar radiopurity as in Borexino, and a similar quenching mechanism as in PC. The black curve represents the summarized solar neutrino spectrum. The data was taken from [Smi08], in the case of ^{210}Bi from [Mer08].*

Because ^{210}Po decays via α -decay, a pulshape discrimination¹⁴ can reduce the background from this source by about $\geq 95\%$ [Bx07a]. Although the emitted α particles are monoenergetic, the shape of the pulse is widened due to the detector's energy resolution. Because of the relatively short half-life of 138.4 d, most of the ^{210}Po has decayed after a few years (This is only sufficed if the contamination with

¹⁴The mean decay time of the light intensity in an organic liquid-scintillator is different for α and β particle events, which allows a separation of the two events.

^{210}Pb is very low in the scintillator, because ^{210}Po is a decay product of ^{210}Pb . Results from Borexino show that the ^{210}Po background rate has decreased about one order of magnitude within one year [Bx08b], see also chapter 5.4). The β^- emitters ^{85}Kr and ^{210}Bi cannot be distinguished from a neutrino signal, they have to be statistically subtracted. It is therefore crucial to know the abundancies and reaction rates of radionuclides in an organic liquid-scintillator detector.

5.3 $^8\text{B}-\nu$ Analysis with LENA

The new measurement of ^8B neutrinos by the Borexino detector delivered only recently for the first time proof of the MSW-LMA solution in the regime between vacuum driven and solar matter induced neutrino oscillations [Bx08b]. The motivation for this analysis is to investigate the potential of the LENA detector on this topic.

For the analysis, the threshold rate was set to 250 keV, but even for 200 keV, the event rates are only insignificantly higher (See Table 5.1), so the choice of the threshold energy almost does not affect this analysis at all. As of today, the MSW probability curve is known only for low energies (below 1 MeV) or high energies (above 7 MeV) and the interesting part in the middle part is still unconfirmed. Figure 5.4 shows a plot of the MSW-LMA curve with the data that has already been taken by Gallex/GNO and Sage as well as Borexino for the ^7Be neutrinos, and for the higher energetic region, which was measured with great accuracy by the water cherenkov detectors. The data of SNO was implemented into this plot. Additionally to the usual MSW-LMA curve, the MSW-LMA-NSI curve has been implemented, which would result if there were additional non-standard interactions (NSI) of neutrinos with matter. Non-standard interactions are based upon the assumption that the interaction of neutrinos with matter involves physics beyond the standard model [Gro95]. The MaVaN prediction is the probability curve one would obtain, if there were mass-varying neutrinos. As can be seen, the MSW curve has been confirmed in these energy regions, but a confirmation in the energy regime of around 2-3 MeV would be very rewarding. This region is particularly interesting, because the regime around 2 MeV is the transition region between vacuum dominated and matter induced neutrino oscillations by the MSW effect in the sun. With a detector such as LENA, a much higher statistics than for example in Borexino could be achieved in order to deliver another proof for the MSW-LMA curve. For this purpose, an analysis was performed for the ^8B neutrinos in LENA, using a statistical χ^2 method.

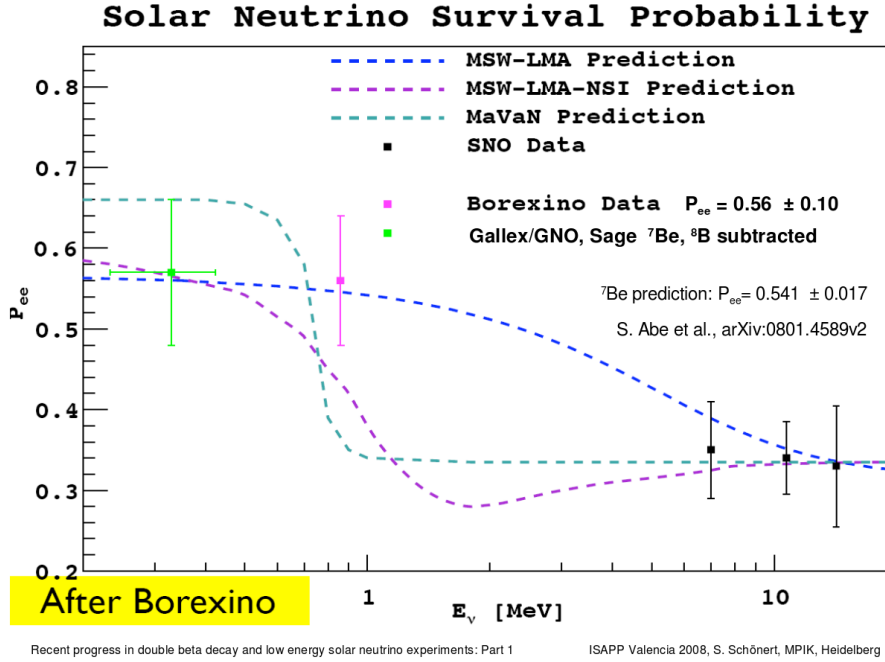


Figure 5.4: *This is the MSW-LMA survival probability as it has been confirmed today by different detectors, in comparison to the MSW-LMA-NSI (non standard interactions) and the MaVaN (mass varying neutrinos) curves. In the lower energetic regime, the data by Gallex/GNO, Sage and Borexino confirm the MSW-LMA curve. In the higher energetic regime, the curve is proven by the data of SNO. Yet, a confirmation of the curve in the middle energy regime of around 2-3 MeV would be very rewarding. In this chapter the potential of LENA for a confirmation of this curve will be analyzed. The plot was taken from [Sco08].*

5.3.1 Influence of the MSW effect on the ^8B spectrum

Figure 5.5 shows the analytical ^8B neutrino recoil spectrum for LENA, one curve representing the existence, the other one representing the absence of the MSW effect. The integrated event rate with MSW effect is the value from Table 5.1 $((2.8076 \pm 0.4492) \cdot 10^4 \text{ yr}^{-1} (18\text{kt})^{-1})$. Without MSW effect, the rate is significantly higher, namely $(3.7911 \pm 0.6066) \cdot 10^4 \text{ yr}^{-1} (18\text{kt})^{-1}$.

5.3.2 χ^2 analysis

In order to analyze the significance of LENA's statistics concerning the MSW effect in the transition regime between matter and vacuum dominated oscillations, a χ^2 -analysis of the ^8B spectrum was performed for different runtimes. The analysis will be performed for a threshold energy of 2.0 MeV and 2.8 MeV, respectively, because of the cosmogenic background in this regime (see Figure 5.3). The background will

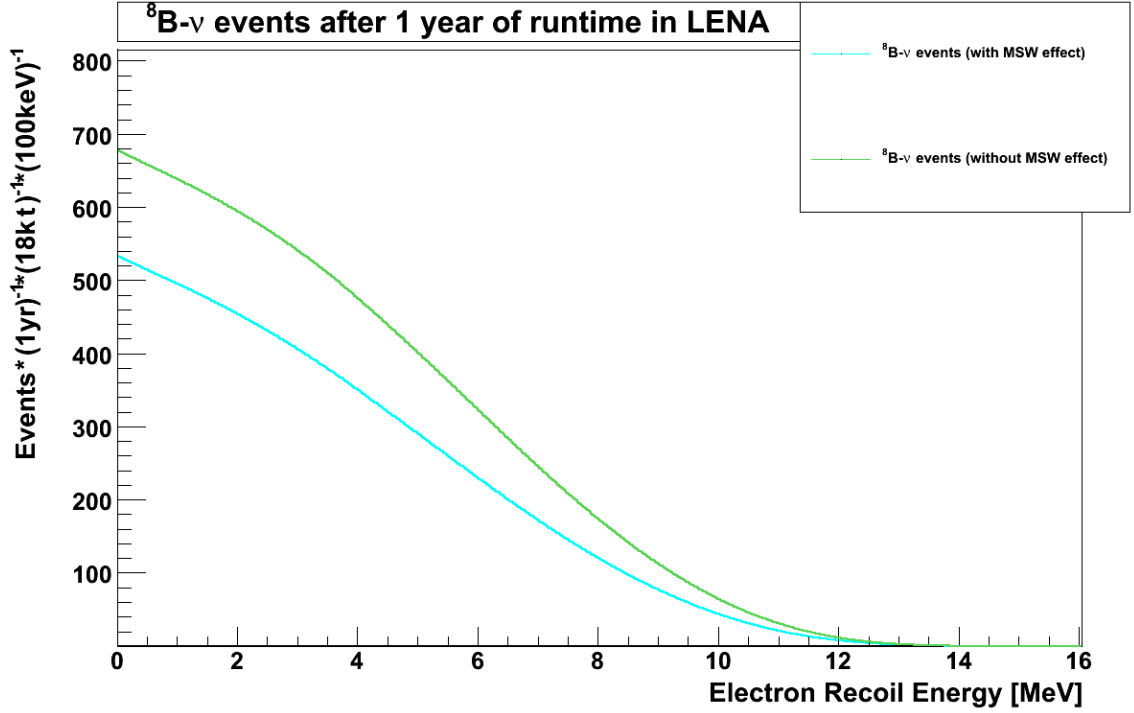


Figure 5.5: *This plot shows the influence of the MSW effect on the neutrino spectrum for a runtime of 1 year. The green curve represents the absence of the MSW effect, where only vacuum neutrino flavour oscillations can occur, and the blue curve represents the existence of the MSW effect, where additionally matter induced flavour oscillations take place.*

be discussed in more detail in chapter 5.3.3.

Figure 5.6 shows the spectrum of the ^8B neutrinos with and without the MSW effect for the runtime of 1 year. The number of randomly generated events¹⁵ equals to the number of events for the whole energy spectrum, which is $2.9369 \cdot 10^4 \text{ yr}^{-1} (18\text{kt})^{-1}$ for the existence of the MSW effect and $3.9558 \cdot 10^4 \text{ yr}^{-1} (18\text{kt})^{-1}$ for the absence of the MSW effect, respectively. The drawn through lines represent the analytical result. The statistical error is proportional to \sqrt{N} , N being the number of events per energy bin (100 keV/bin). The energy resolution in the regime around (2.0-2.8) MeV, where the analysis was performed, is in the range of 5.27%-4.45%. This corresponds to 105 keV and 126 keV, respectively. The binning should therefore be of the same order, which was also considered for this analysis. The χ^2 distribution is given by

$$\chi^2 = \sum_{i=1}^n \left(\frac{x_i - \nu_i}{\sigma_i} \right)^2 \quad (5.15)$$

¹⁵For every bin a random number is generated from a gauss function with the mean being the value of the bin and the statistical error given by \sqrt{N} .

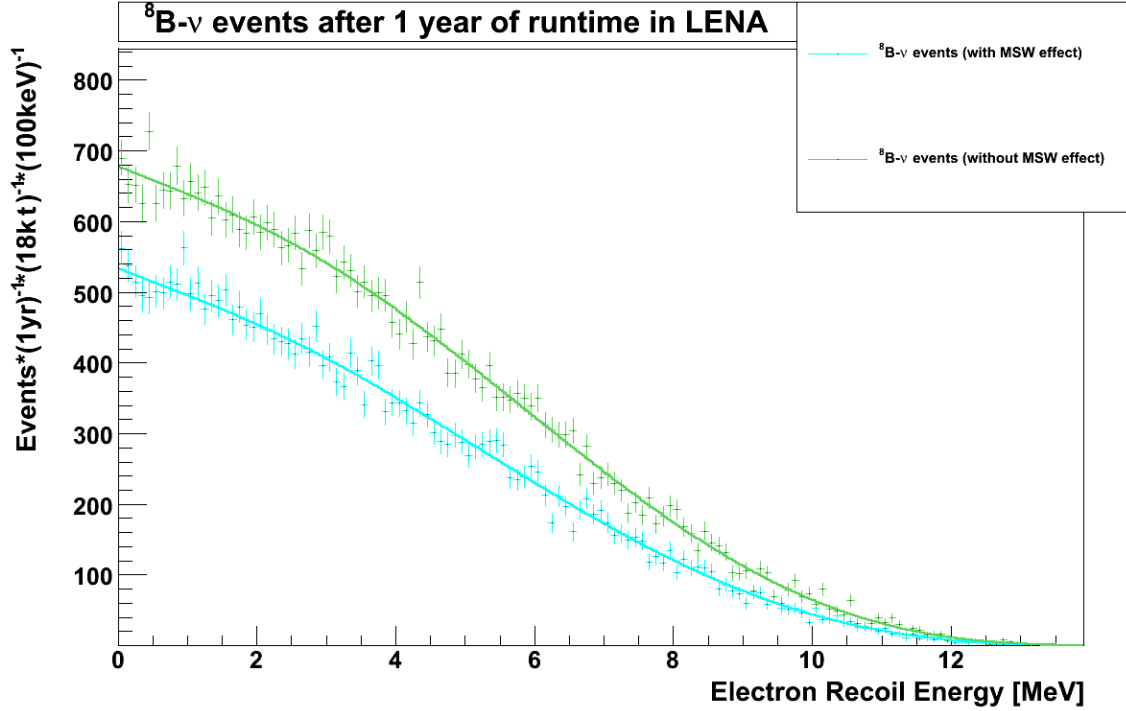


Figure 5.6: This plot shows a simulation of the ${}^8\text{B}$ neutrino spectrum with and without the MSW effect after a 1 year runtime in LENA. The drawn through lines represent the analytical results. The error bars represent the statistical error which is proportional to \sqrt{N} .

whereas x_i is the measured random value, ν_i the expectation value, thus the value of the analytical calculated spectrum, and σ_i the error for each data point.

5.3.3 Results and discussion

The analysis was performed with a Monte Carlo simulation using the ROOT toolkit from CERN [Cer]. The results for the reduced χ^2 value and their corresponding confidence level can be seen in Table 5.4.

For each runtime, 5 simulations were performed in order to decrease the statistical fluctuation. The χ^2/NDF value in the right column is the mean of the values from the 5 simulations.

The analysis was performed for two different threshold energies, 2.0 MeV, and 2.8 MeV, as in the Borexino MSW analysis [Bx08b]. The analysis for the lower threshold is based on the assumption that the ${}^{10}\text{C}$ background can be statistically subtracted from the measurement. It is the main background source in this energy regime (See Figure 5.3), and is cosmogenic, thus created by atmospheric myons. It is a β^+

6 months				
	$E_{thr} = 2.0 \text{ MeV}$		$E_{thr} = 2.8 \text{ MeV}$	
Measured \iff Expected	χ^2/NDF	C.L.	χ^2/NDF	C.L.
MSW \iff MSW	2.2286	< 0.5 %	2.0665	< 0.5 %
no MSW \iff no MSW	2.1605	< 0.5 %	2.2308	< 0.5 %
MSW \iff no MSW	28.3498	< 0.5 %	27.6908	< 0.5 %
no MSW \iff MSW	38.99038	< 0.5 %	38.07178	< 0.5 %

12 months				
	$E_{thr} = 2.0 \text{ MeV}$		$E_{thr} = 2.8 \text{ MeV}$	
Measured \iff Expected	χ^2/NDF	C.L.	χ^2/NDF	C.L.
MSW \iff MSW	1.0373	25 %	1.1185	10 %
no MSW \iff no MSW	1.1223	10 %	1.1314	10 %
MSW \iff no MSW	27.8762	< 0.5 %	26.9760	< 0.5 %
no MSW \iff MSW	36.4116	< 0.5 %	36.8180	< 0.5 %

18 months				
	$E_{thr} = 2.0 \text{ MeV}$		$E_{thr} = 2.8 \text{ MeV}$	
Measured \iff Expected	χ^2/NDF	C.L.	χ^2/NDF	C.L.
MSW \iff MSW	0.6299	99 %	0.6449	97.5 %
no MSW \iff no MSW	0.6976	97.5 %	0.6723	97.5 %
MSW \iff no MSW	27.5321	< 0.5 %	26.6070	< 0.5 %
no MSW \iff MSW	36.0019	< 0.5 %	35.0857	< 0.5 %

24 months				
	$E_{thr} = 2.0 \text{ MeV}$		$E_{thr} = 2.8 \text{ MeV}$	
Measured \iff Expected	χ^2/NDF	C.L.	χ^2/NDF	C.L.
MSW \iff MSW	0.5524	99.9 %	0.5469	99.9 %
no MSW \iff no MSW	0.5331	99.9 %	0.5519	99.9 %
MSW \iff no MSW	27.4180	< 0.5 %	26.5575	< 0.5 %
no MSW \iff MSW	35.8063	< 0.5 %	35.4626	< 0.5 %

Table 5.4: *This table summarizes the values of χ^2/NDF for different runtimes. NDF is the value for the degrees of freedom of the fit, in this case corresponding the number of bins. The analysis was performed for a threshold of 2 MeV and 2.8 MeV, respectively [Bx08b]. The values over 9 MeV were neglected for this analysis because they are too close to zero.*

emitter with a lifetime of $\tau = 19.3\text{s}$. Because of the short lifetime, a method for discriminating the ^{10}C background from actual neutrino events would be to ignore

all events that occur within a time window of $3\tau - 5\tau^{16}$ after a muon enters the detector, which can be identified by the muon veto. If the dead time from this method exceeds 50%, another method is more desirable. It should also be possible to veto a cylindrical volume around the track of every muon that is registered by the muon veto. With this method the ^{10}C background could be eliminated and the threshold could thus be set lower without having this dead time. Below 2.0 MeV there are too large contributions from ^{11}C , also a cosmogenic radionuclide, but with a greater lifetime of $\tau = 20.38$ min. The method of muon-tagging would not work with ^{11}C , because of the long lifetime there would remain no timeframe to measure actual neutrino events. There are efforts ongoing to tag ^{11}C events in Borexino, but at the moment a threshold under 2.0 MeV is not feasible for the ^8B analysis. However, there still remain two background components over 2.8 MeV, the first being ^{214}Bi , which belongs to the ^{238}U chain, and ^{208}Tl from the ^{232}Th chain [Bx08b]. ^{214}Bi can be rejected event by event with an efficiency of 89% [Bx08b], the residual contamination can be neglected. ^{208}Tl can be statistically subtracted by measuring the delayed coincidences of its branching competitor, ^{212}Bi - ^{212}Po [Bx08b].

As was already mentioned, the quenching in PC is about 1.13 times higher than in PXE, so the threshold in LENA will be higher, but for this analysis the values of Borexino were used.

The runtimes which were simulated are 6 months, 12 months, 18 months and 24 months, and each runtime was simulated 5 times in order to increase the statistics. The NDF (Degrees of freedom) value equals 71 for 2.8 MeV and 64 for 2.0 MeV, respectively. For higher energies, the event rates are too close to zero. Therefore the analysis is only performed up to 9 MeV. There are four χ^2/NDF values for each runtime:

- One for the case that the MSW data points are fitted with the MSW curve (MSW \iff MSW)
- One for the case that the non-MSW data points are fitted with the non-MSW curve (no MSW \iff no MSW)
- One for the case that the MSW data points are fitted with the non-MSW curve (MSW \iff no MSW)

¹⁶This time is needed so that the muon induced ^{10}C background has decayed to a high extent.

- One for the case that the non-MSW data points are fitted with the MSW curve (no MSW \iff MSW)

As can be seen, for a runtime of 6 months the fit for either of the 4 scenarios and the two threshold energies is not statistically significant. For a runtime of 12 months, the fits (MSW \iff MSW) and (no MSW \iff no MSW) have a better χ^2/NDF , but the C.L. is still below 25 % and 10 % respectively, a too small value to be considered statistically significant. After 18 months of runtime, the first statistically significant fits can be obtained. The MSW data points can be fitted with the MSW curve on a 99 % C.L. for a threshold of 2.0 MeV. This result would be already considered as proof for the MSW-LMA survival solution. The other fits are slightly worse, but this is due to statistical fluctuations. After 24 months of runtime, the MSW-LMA survival probability could be already proven on a 99.9 % C.L. As can be also seen for all four runtimes, the fit of the MSW data points with the non-MSW curve and vice versa delivers very high χ^2/NDF values. Thus, the scenario of wrongly interpreting the data as the MSW-LMA solution, although the non-MSW-LMA exists, is below 0.1 %. The reason why the χ^2/NDF value for the (MSW \iff no MSW) scenario is lower than (no MSW \iff MSW), is the following: The error of the MSW data points is lower than the error for the non-MSW data points. Because the χ^2 function is proportional to $\sum_i \frac{1}{\sigma_i}$, the χ^2 function has a higher value for a fit with lower errors, which is the case for the fit of the non-MSW curve with the MSW data points.

5.4 Periodic oscillations of the ${}^7\text{Be}$ neutrino flux

The following section analyzes periodic oscillations of the ${}^7\text{Be}$ neutrino flux due to the excentricity of the earth orbit, the day/night-effect, and possible oscillations of the ${}^7\text{Be}$ neutrino production rate due to G modes in the sun (see chapter 4.3.2). The ${}^7\text{Be}-\nu$ flux seems the best choice for analysis of periodic neutrino flux oscillations because of the very high statistics with ~ 4800 events/day above a threshold energy of 250 keV and ~ 5400 events above a threshold of 200 keV, respectively (see Table 5.1). Although the $pp - \nu$ have a higher flux, they cannot be detected due to the abundance of ${}^{14}\text{C}$ in the detector below a threshold of 200 keV-250 keV, which is several orders of magnitude higher than the neutrino flux.

The main background source for the ${}^7\text{Be}-\nu$ signal is ${}^{210}\text{Po}$, which is in PXE nearer to the energy regime of the ${}^7\text{Be}$ "shoulder". The ${}^{210}\text{Po}$ peak in Borexino is at lower energies than in PXE, because PC has a higher quenching factor. Nevertheless this background should not pose a threat to the measurement, because it can be, as already mentioned, reduced by almost two orders of magnitude by means of the $\alpha - \beta$ discrimination. Additionally ${}^{210}\text{Po}$ has a lifetime of $\tau = 138.4$ d, so that already after a year the background signal should be lowered by a factor of 6. After 5 years only 0.01 % of the primarily abundant ${}^{210}\text{Po}$ in the detector would remain, and would thus

not contribute to the ${}^7\text{Be}-\nu$ background any more. This is again under the premise that no ${}^{210}\text{Po}$ is produced by abundant ${}^{210}\text{Pb}$ as was already mentioned in section 5.2.4. However, the ${}^{85}\text{Kr}$ background suppresses a measurement of the 384 keV line, because it surpasses the neutrino events by one order of magnitude (see Figure 5.3). Therefore only the 862 keV line, that makes up 90 % of the total ${}^7\text{Be}$ neutrino flux was considered for this analysis.

The following plot shows a simulation of the statistical distribution of ${}^7\text{Be}$ neutrino events in the LENA detector, after 1 day and after 10 days, respectively. The binning was set to 50 keV/bin, because the energy resolution of LENA at the ${}^7\text{Be}$ "shoulder" is about 8.3 %, thus about 67 keV.

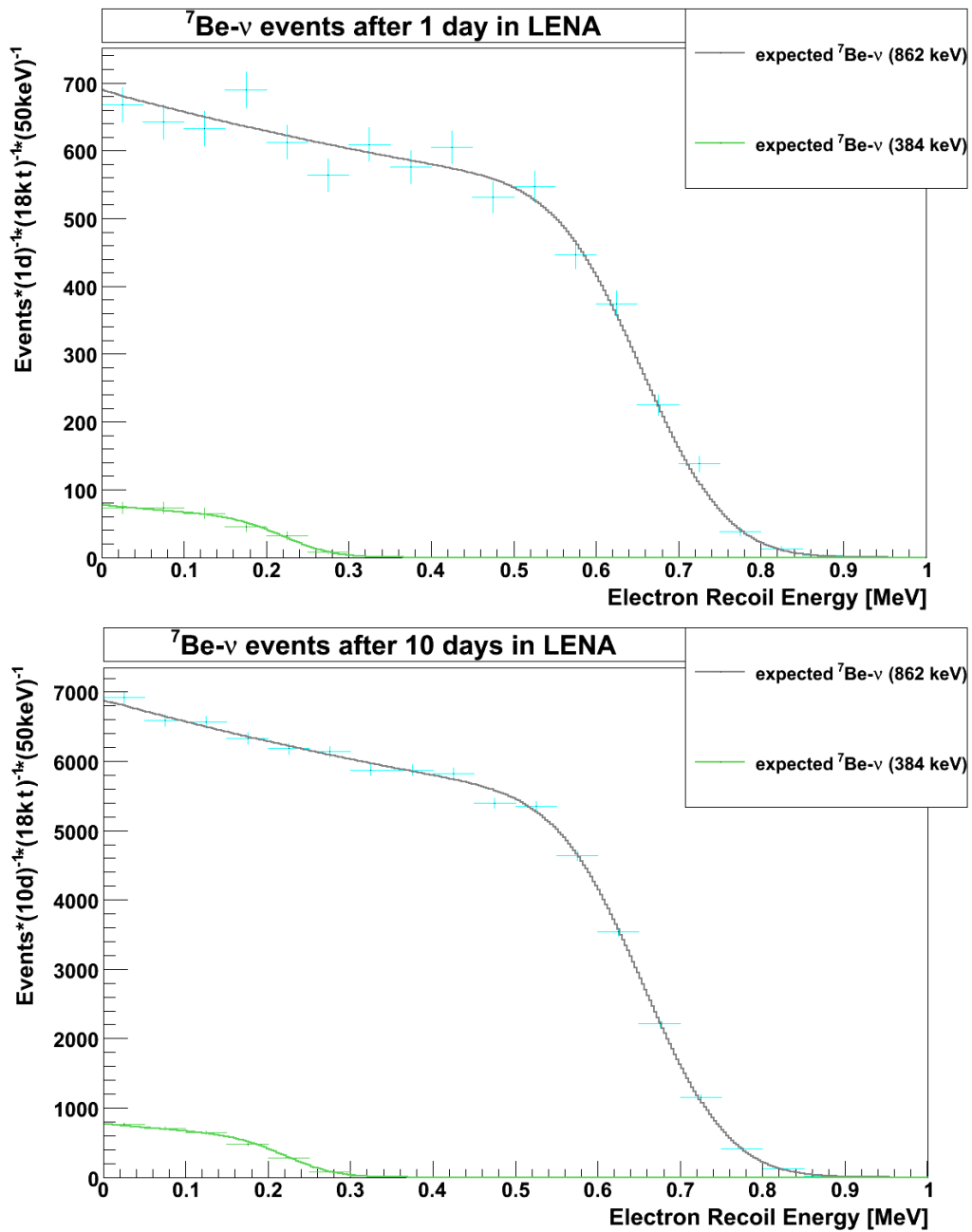


Figure 5.7: The plot shows the expected ⁷Be neutrino events in LENA after 1 day and 10 days of measurement, respectively. The data points are drawn with a binning of 50 keV/bin for both plots which is in the order of the energy resolution of LENA in this energy regime. For comparison the analytical curve is shown also. As can be seen the statistics have improved significantly after 10 days of data acquisition.

5.4.1 Periodic oscillations of the ${}^7\text{Be}$ neutrino flux due to Kepler motion

The following analysis was performed for a threshold energy of 200 keV.

The first effect that has to be taken into account, is the periodic oscillation of the neutrino flux due to the changing distance of the earth to the sun in the course of one year. Thus, the flux becomes a function of time $\Phi = \Phi(t)$, and accordingly also the measured neutrino event rates on earth should change. The motion of the earth around the sun follows a Kepler trajectory (effects of general relativity are too small and can thus be neglected for this analysis):

$$r(\Theta) = \frac{p}{1 + \epsilon \cdot \cos(\Theta)} \quad (5.16)$$

with the excentricity of the earth orbit $\epsilon = 0.0167$ and the parameter $p = r_{min}(1 + \epsilon) = 1.496 \cdot 10^8$ km (see Table 4.1). The angle Θ follows the relation $\Theta = 2\pi \cdot \frac{t}{T}$ with $T=365$ days. The flux suffices the relation $\frac{\Phi(t)}{\Phi} = \left(\frac{r(t)}{r_0}\right)^2$ and thus it can be obtained

$$\Phi(t) = \Phi_0 \cdot \left(r_0 \cdot \frac{1 + \epsilon \cdot \cos\left(\frac{2\pi \cdot t}{T}\right)}{p} \right)^2 \stackrel{p=r_0}{=} \Phi_0 \cdot \left(1 + \epsilon \cdot \cos\left(\frac{2\pi \cdot t}{T}\right) \right)^2 \quad (5.17)$$

with $\Phi_0 = 4.86 \cdot 10^9 \text{ cm}^{-2} \text{ s}^{-1}$ the mean ${}^7\text{Be}-\nu$ flux on earth. The event rate in LENA is now a function of the neutrino flux $\frac{dN}{dE} = \frac{dN(\Phi(t))}{dE}$. As can be verified, the order of the effect is about 6.8%. Figure 5.8 shows the analytical result of the oscillation of the event rate in the course of one year which was aquired by integration of the recoil spectrum over the whole energy range. The green points represent the Monte Carlo simulation. They were generated using a gaussian distribution of the measured values around the analytical curve with $\sigma = \sqrt{N}$, N being the number of events. The binning was chosen to be 1 day, with an average of about 5400 events/day, high enough statistics for this analysis.

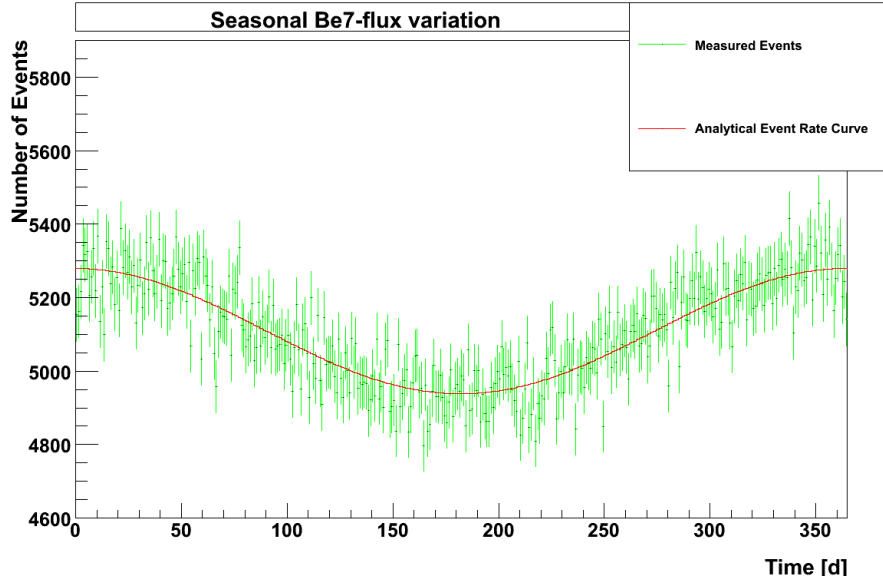


Figure 5.8: *This plot shows the seasonal ${}^7\text{Be}-\nu$ flux variation in the course of one year due to the changing distance of the earth to the sun, which is described through the Kepler Law. The green data points represent the Monte Carlo simulation with $\sigma = \sqrt{N}$, the red line is the analytical curve. One bin is the equivalent of 1 day of measuring time.*

As can be seen in Figure 5.9, the statistical significance of the seasonal effect is very high. In the left plot, the seasonal curve is fitted with a function of the form of equation 5.17, which would be seen if the flux would change over time. The χ^2/NDF value is for this case 0.99, so the data matches the fit function. The right plot shows the same seasonal flux variation fitted with a linear curve, for the case of no variation. As can be seen, the χ^2/NDF for this fit is much larger, 3.85, so that this case can be excluded on a 99.9% C.L.

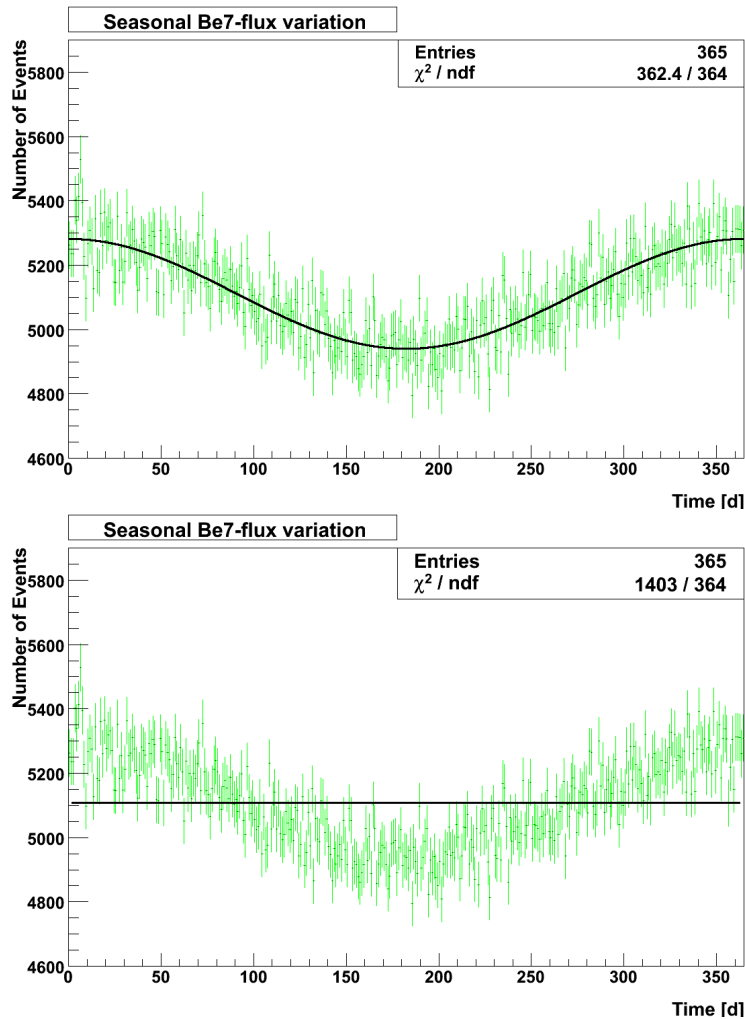


Figure 5.9: The two plots show a fit for the seasonal flux variation due to the Kepler motion of the earth. The upper plot fits the data with the expected curve ($\chi^2/NDF = 0.99$), and the lower is a fit for a constant time dependence of the flux. As can be seen, the right fit can be excluded on a 99.9% level, with a $\chi^2/NDF = 3.85$.

5.4.2 Periodic oscillations of the ${}^7\text{Be}$ Neutrino Flux due to the day/night-effect or G modes

In addition to the seasonal variation of the neutrino flux due to the Kepler motion of the earth around the sun, which could be detected in LENA after one year as was shown on a 99.9% C.L., there could be additional fluctuations in the neutrino signal. The motivation to search for further oscillations in the flux is due to the prediction that there is a day/night asymmetry of the signal in the order of 1% of the signal. This difference comes from the conversion of solar $\nu_e \rightarrow \nu_\mu$ ¹⁷ because

¹⁷ $\nu_e \rightarrow \nu_\tau$ is also possible, but not as probable, because $\sin^2(2\Theta_{13}) < 0.19$ in the current limit

of the earth matter, analogous to the MSW effect in the sun.

As was shown, solar gravity modes could have in addition a significant impact on the survival probabilities of solar neutrinos, and could also lead to an oscillation of the neutrino production rates in the sun. Therefore, there is the possibility of oscillations in the neutrino flux that are superimposed over the seasonal flux variations. The next plot shows hypothetical flux oscillations with an amplitude of 4% of Φ_0 , a cycle duration of 30 days and a fixed phase $\phi = 0$ d.

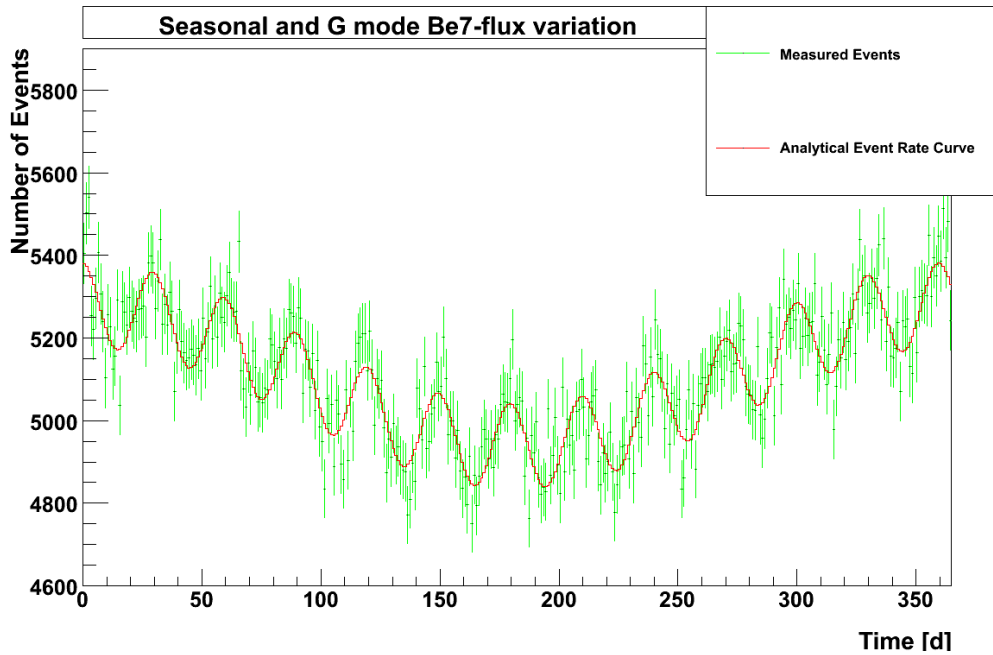


Figure 5.10: *This plot shows the ${}^7\text{Be}-\nu$ flux variation due to oscillation modes, superimposed with the ordinary flux variation due to the motion of the earth around the sun. For this plot, the amplitude of the modes was set to 4% of Φ_0 , the cycle duration T to 30 days and the phase was fixed to $\phi = 0$ d.*

In order to verify the detectability of such periodic oscillations of the ${}^7\text{Be}$ neutrino flux with cycle durations in the order of hours to months, two χ^2 analyses are performed. The first analysis simulates the data taking of the detector in steps of one day for 365 days. In order to also include oscillations on shorter time scales in the order of hours or days, another analysis is performed with bins of one hour.

The analysis is performed for different combinations of cycle duration and amplitude of the oscillations. The flux oscillations have in general three parameters, the amplitude A , the cycle duration T and a phase ϕ . A Monte Carlo simulation was written again using the ROOT toolkit from CERN, which was used to generate a set of data for a given A and T which were both changed in small steps. Next, the phase was also varied.

Then, for every generated data set, two cases were fitted: The case of no additional

mode oscillations, but only seasonal variations of the flux, and the case of the same fluctuations as was used for the generation of the data set, which always delivered a good fit value. Then, the χ^2/NDF value for every data set was fitted with no oscillations, retrieved and plotted into a three dimensional histogramm, where the x- or y- axis is A, T or ϕ , respectively and the z-axis is χ^2/NDF . The resulting histogramm now shows the distribution of the χ^2/NDF for the fit of the generated mode with only the seasonal oscillation. The fit of the mode with the same oscillation delivers a very good χ^2/NDF , the fit of the mode with no oscillations delivers a bad χ^2/NDF . Thus, a fit of an oscillation mode which delivers a good fit value for a fit with no oscillations can be excluded from detection, because no conclusion can be drawn regarding the existence of an oscillation. Every point in the 2D plane of A, T or ϕ now has exactly one χ^2/NDF value. Additionally, the χ^2/NDF value is an indicator for the confidence level of the measurement. This fit has exactly $365 - 3 = 362$ degrees of freedom (NDF), because every bin contains data from one day, and there are three fit parameters. In χ^2 tables, such as in [Har], the confidence level for a given χ^2 can be obtained for different degrees of freedom. The hypothesis that will be tested is that there are no oscillations. If a fit is good, it will be excluded, because this means that even for the existence of an oscillation, the fit with the scenario of no oscillation delivers a good fit value.

5.5 Results and discussion

5.5.1 Analysis of oscillations with 1 day binning

In this analysis A was changed from 0% up to 6% of the total flux Φ_0 in steps of 0.005%, and T from 1 day up to 365 days in steps of 1 day. The phase was also varied in steps of one day. The exclusion limit for $NDF = 362$ is $\chi^2/NDF \leq 1.101$ on a 90% C.L. On a 99% or 3σ C.L., the exclusion limit for 362 degrees of freedom is $\chi^2/NDF \leq 1.189$ [Har]. If the χ^2/NDF fit value is above the respective C.L., it can be excluded, thus an oscillation can be clearly identified. If the value is below the respective χ^2/NDF limit, the value cannot be excluded, thus the detection of an oscillation is not possible.

The next three plots show different combinations of the three fit parameters with their respective χ^2/NDF values in a topographic 3 dimensional plot. The possible combinations are $\langle A, T, \chi^2/NDF \rangle$, then $\langle A, \phi, \chi^2/NDF \rangle$ and $\langle T, \phi, \chi^2/NDF \rangle$. For the plot with varying A and T, the phase was fixed to $\phi = 0$ d. In the next case, for varying A and ϕ , T was set to 120 days. In the last case, the amplitude was fixed to 1.5% of Φ_0 . The first plot (Figure 5.11) shows the dependance of the cycle duration with respect to the amplitude. The left picture shows the 3 dimensional distribution of χ^2/NDF whereas the right plot shows the projection of the left plot onto the A-T

plane. The purple region of the plot has low χ^2/NDF values. These regions can be excluded from detectability because a fit with an oscillation mode to the case of no oscillations still delivered a good fit result, so no conclusion can be drawn regarding the existence of additional oscillations beside the seasonal variation.

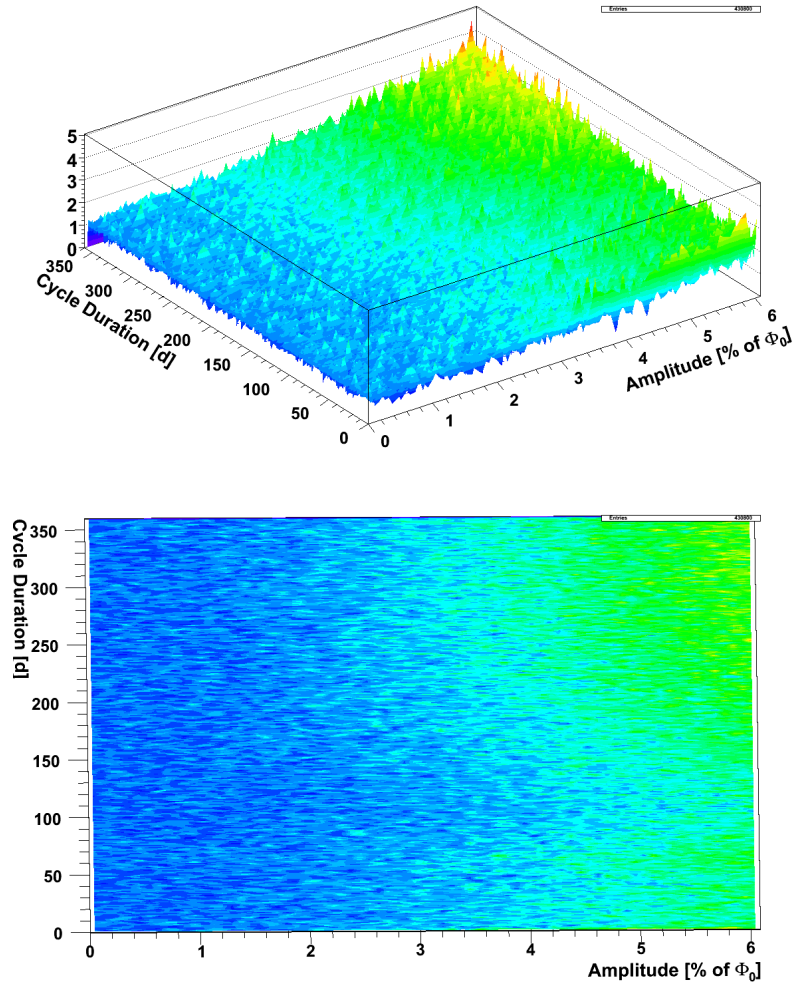


Figure 5.11: *The upper image shows the 3 dimensional distribution of the χ^2/NDF value from every fit with a fixed phase of zero days, and varying A and T . The amplitude was changed in steps of 0.005% of Φ_0 from 0% to 6%, and the cycle duration was changed in steps of one day beginning from one day up to one year. The lower image shows the projection of the left image onto the A - T plane. It can be seen that the measurable amplitude is dependant from the cycle duration. Purple regions indicate a good fit and thus a bad detectability.*

Figure 5.12 shows the same distribution, but now a point was filled into the histogram for every fit up to the threshold of $\chi^2/NDF \leq 1.101$ for a 90% C.L. and $\chi^2/NDF \leq 1.189$ for a 99% C.L. Above these thresholds, the fits can be excluded

with the respective confidence levels, thus a detectability of additional oscillations with the respective confidence levels is possible in these regions. The exclusion contour lines were also drawn into the histograms. This is the final result for the sensitivity of the detector of additional oscillations.

What can be seen is that for a fixed phase, with for example $\phi = 0$ d, additional oscillations with an amplitude of more than $\sim 1.5\%$ could be detected for large cycle durations of over 300 days on a 99% C.L. For very small cycle durations in the order of days, the detectability seems to improve towards an amplitude of 1.4% of Φ_0 . The reason is that for small cycle durations, the oscillation is in the order of the binning of the analysis. The Nyquist-Shannon sampling theorem [Nyq28] from information processing theory states that if the sampling rate of a test function is in the order of the binning, the test function is not determined. For this analysis, low cycle durations seem to lead to a better detectability because the oscillation function becomes a step function for $T = 1$ day, which leads to a high degree of scattering of the generated data points. Therefore low cycle durations in the regime of 1–10 days can be neglected in the exclusion plot because the seemingly better detectability is not a physical but a numerical effect from the simulation. Figure 5.13 shows the χ^2/NDF dependence of the amplitude for a small cycle duration of three days and a fixed phase $\phi = 0$ d in order to illustrate this effect.

With increased cycle durations, the detectability gets worse until it reaches its maximum at ~ 120 d. This behaviour is illustrated in Figure 5.14.

For larger cycle durations of up to one year, the detectability increases again, because with the fixed phase, the additional oscillation leads to a constructive interference with the seasonal variation curve, which makes the fit worse and leads to a better detectability. This is demonstrated in the three plots of Figure 5.15. The exclusion plot for the amplitude and the phase shows that the χ^2 value does not depend on the phase of the oscillation mode. This is shown in the 3 dimensional histogram of Figure 5.16 for a fixed cycle duration of $T=120$ days. The phase was changed in steps of one day from $\phi = 0$ d to $\phi = 365$ d.

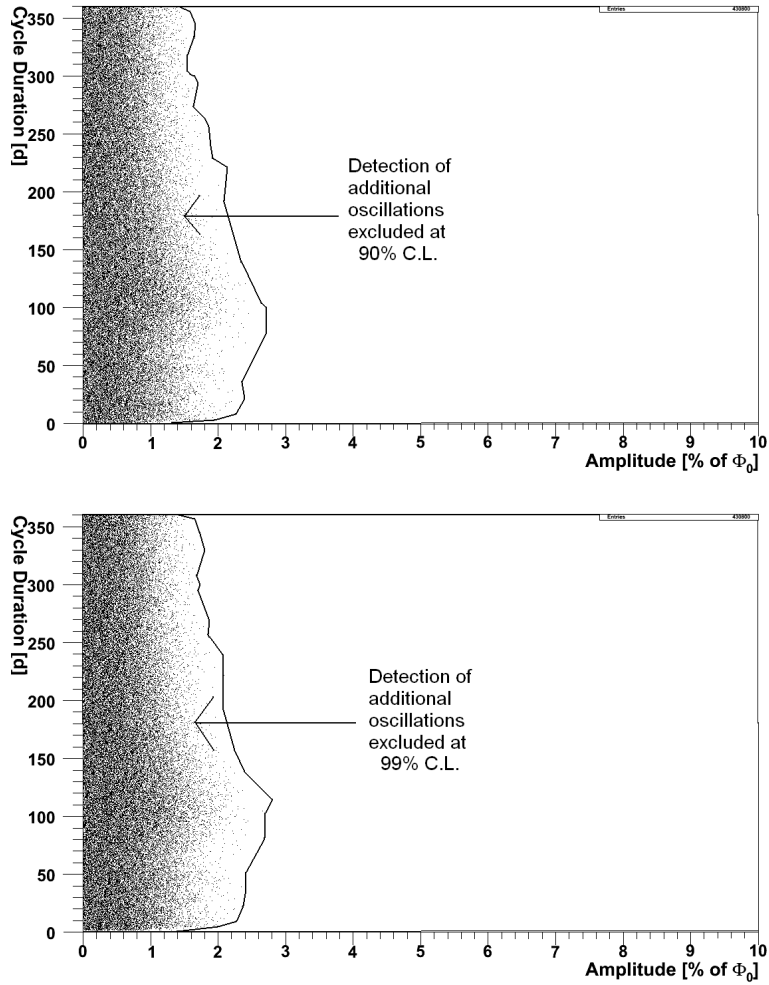


Figure 5.12: *These two plots show the sensitivity of the detector for a fixed phase of zero days, and variable A and T with the same binning as in Figure 5.11. The region on the left is excluded from detection with the respective confidence level, while the white region on the right marks the detectable area. It can be seen that for a cycle duration of ~ 120 d, the detectability of additional oscillations is the worst, whereas large cycle durations are better detectable. The seemingly better detectability of small cycle durations is a numerical effect (Nyquist-Shannon theorem [Nyg28]) because the binning is in the order of the cycle duration. Cycle durations below 10 d can therefore be neglected.*

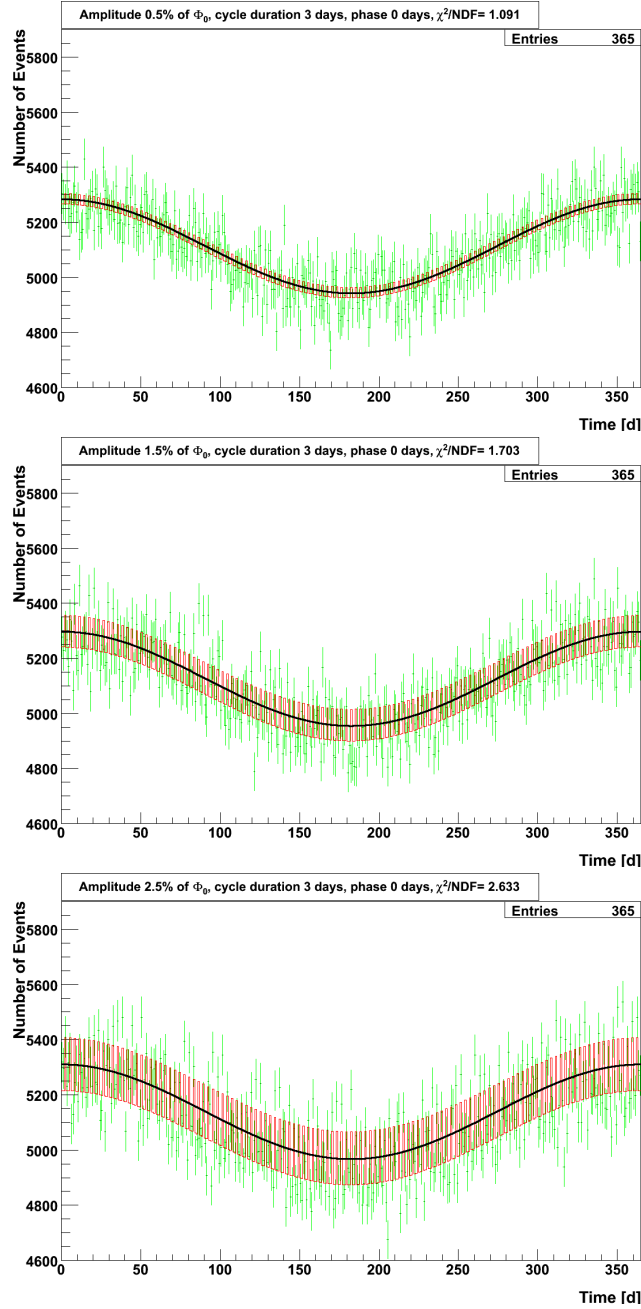


Figure 5.13: This series of plots demonstrates the behaviour of the χ^2/NDF value for $\phi = 0$ d, $T=3$ d and a varying amplitude (from up to down 0.5 %, 1.5 %, 2.5 %, respectively). The χ^2/NDF values are 1.091, 1.703 and 2.633, respectively. The black curve is the seasonal variation without additional oscillations and the red curve represents the analytical oscillation curve from which the data points are generated in a gaussian distribution. The Nyquist-Shannon sampling theorem [Nyg28] states that a test function is not determined if the sampling rate is in the order of the binning of the function. Therefore low cycle durations in the order of 1 – 10 days can be neglected for this analysis because the seemingly better detectability is a numerical, not a physical effect.

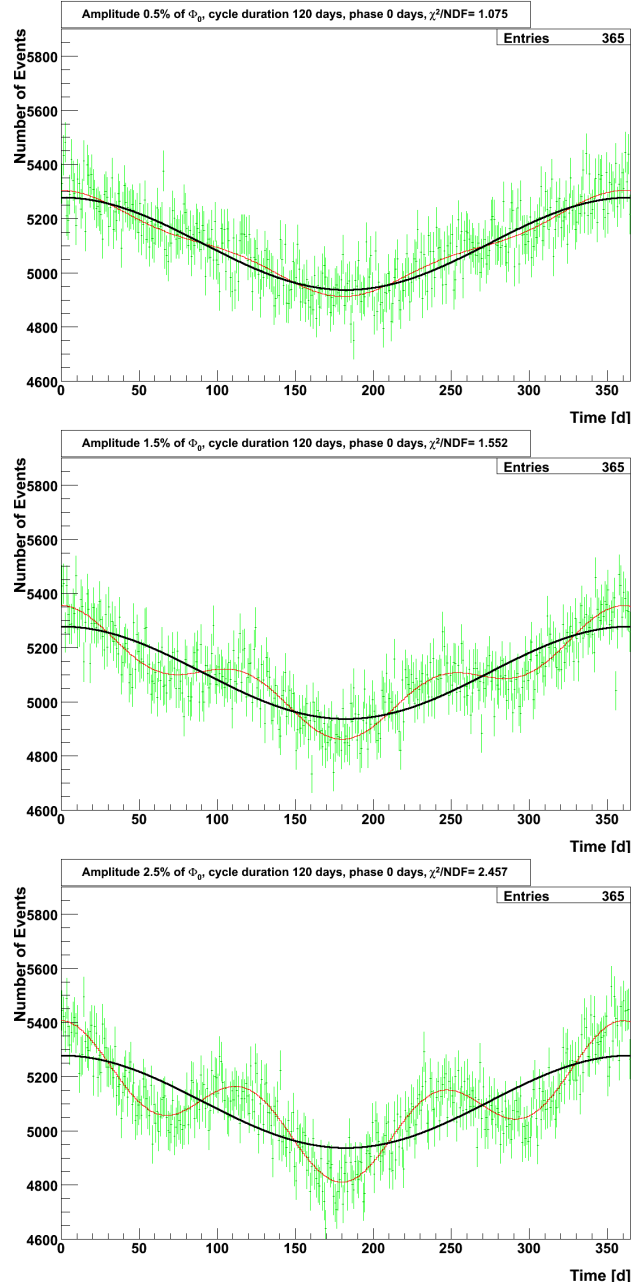


Figure 5.14: This series of plots demonstrates the behaviour of the χ^2/NDF value for $\phi = 0$ d, $T=120$ d and a varying amplitude, which is again changed from 0.5 % to 1.5 % to 2.5 % from up to down. The χ^2/NDF values are 1.075, 1.552 and 2.457, respectively. As can be seen, the fit is better than for smaller cycle durations with the same amplitude, which implies a worse detectability. The oscillation lies within a detectable range down to $\sim 2.7\%$ of the amplitude on a 1σ level or $\sim 2.8\%$ on a 3σ level, respectively. This fit is better than for larger cycle durations of one year, because the oscillation function intersects more often with the seasonal variation function. Therefore the generated points lie in average nearer to the black seasonal variation curve which leads to a better χ^2/NDF .

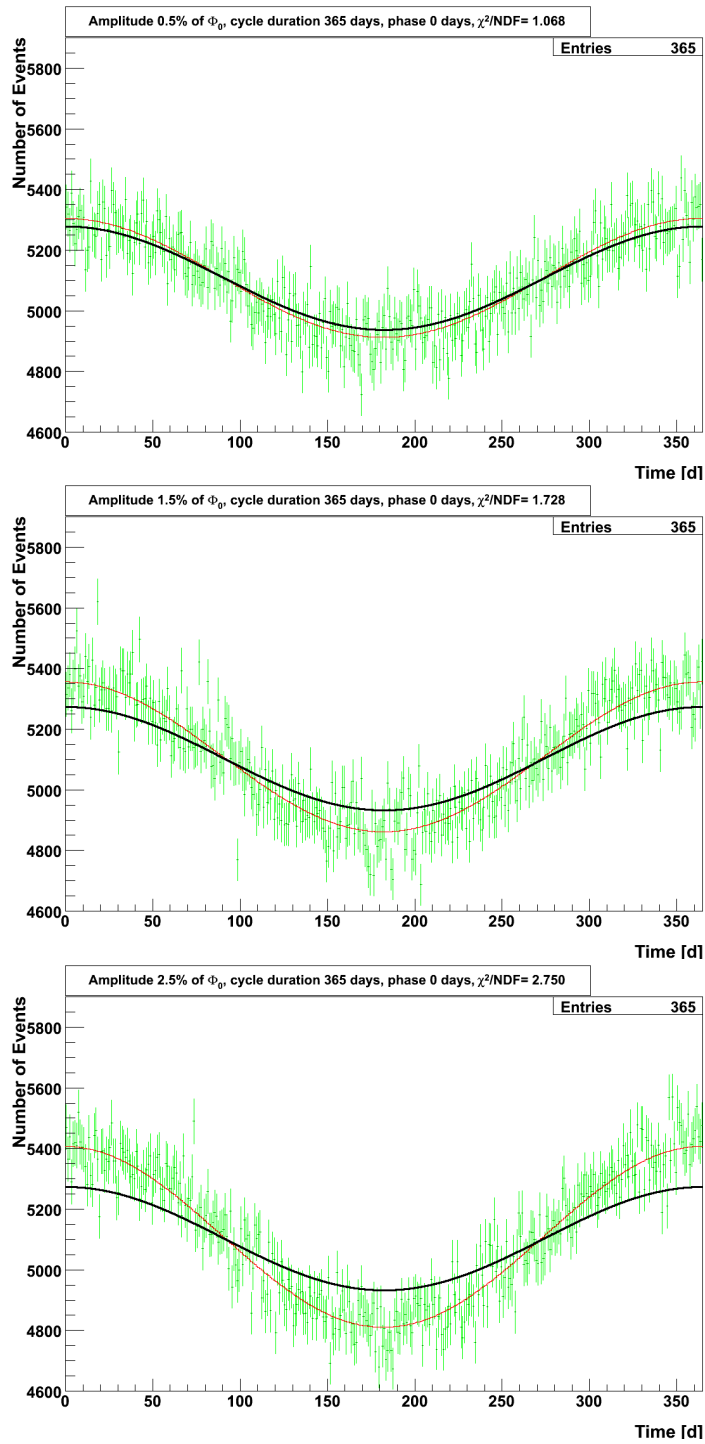


Figure 5.15: This series of plots demonstrates the behaviour of the χ^2/NDF value for $\phi = 0$ d, $T=365$ d and a varying amplitude, which is changed from 0.5% to 1.5% to 2.5% from up to down. The χ^2/NDF values are 1.068, 1.728 and 2.750, respectively. As can be seen, the fit gets worse again than for cycle durations of 120 days with the same amplitude, which leads to a better detectability. The oscillation lies within a detectable range down to $\sim 1.5\%$ of the amplitude on a 1σ level or $\sim 1.6\%$ on a 3σ level, respectively.

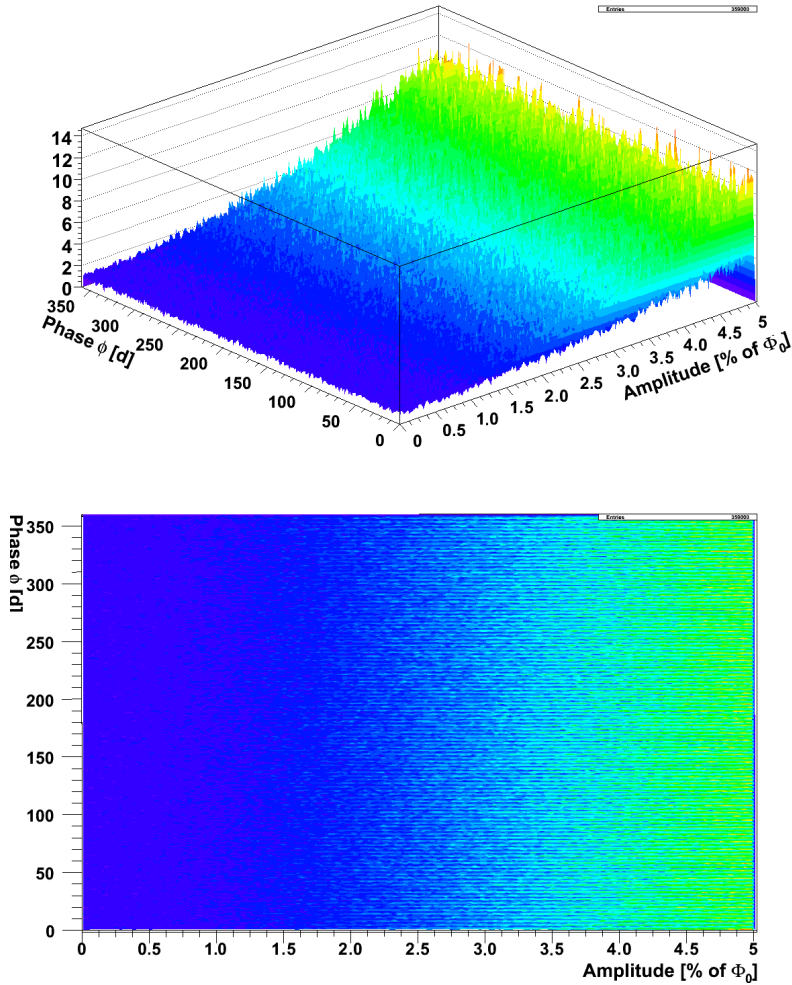


Figure 5.16: *These plots show the χ^2/NDF distribution in dependance of the amplitude and the phaseshift for a fixed cycle duration of 120 days. The purple and blue regions mark good fits. As can be seen, the phaseshift has no influence on the goodness of fit.*

As can be seen, the amplitude shows no dependance from the phase. For a phaseshift of zero days which is the same as 365 days, there is a constructive interference of the mode with the seasonal variation, thus enlarging the difference of the data set to the curve of only seasonal variations. For a non zero phaseshift, the goodness of fit is not afflicted.

This behaviour is illustrated in the next plots (Figure 5.17 and 5.18), which show three different examples for a data set with fixed $T=120$ d, $A=0.5\%$ and $A=2.5\%$, respectively, and a changing phase. The phase is changed in steps of 90 days from $\phi = 0$ d to $\phi=270$ d.

Figure 5.18 shows the same variation of ϕ , but with an increased amplitude of 2.5% , here also no significant dependance of the χ^2 value from the phase is detectable.

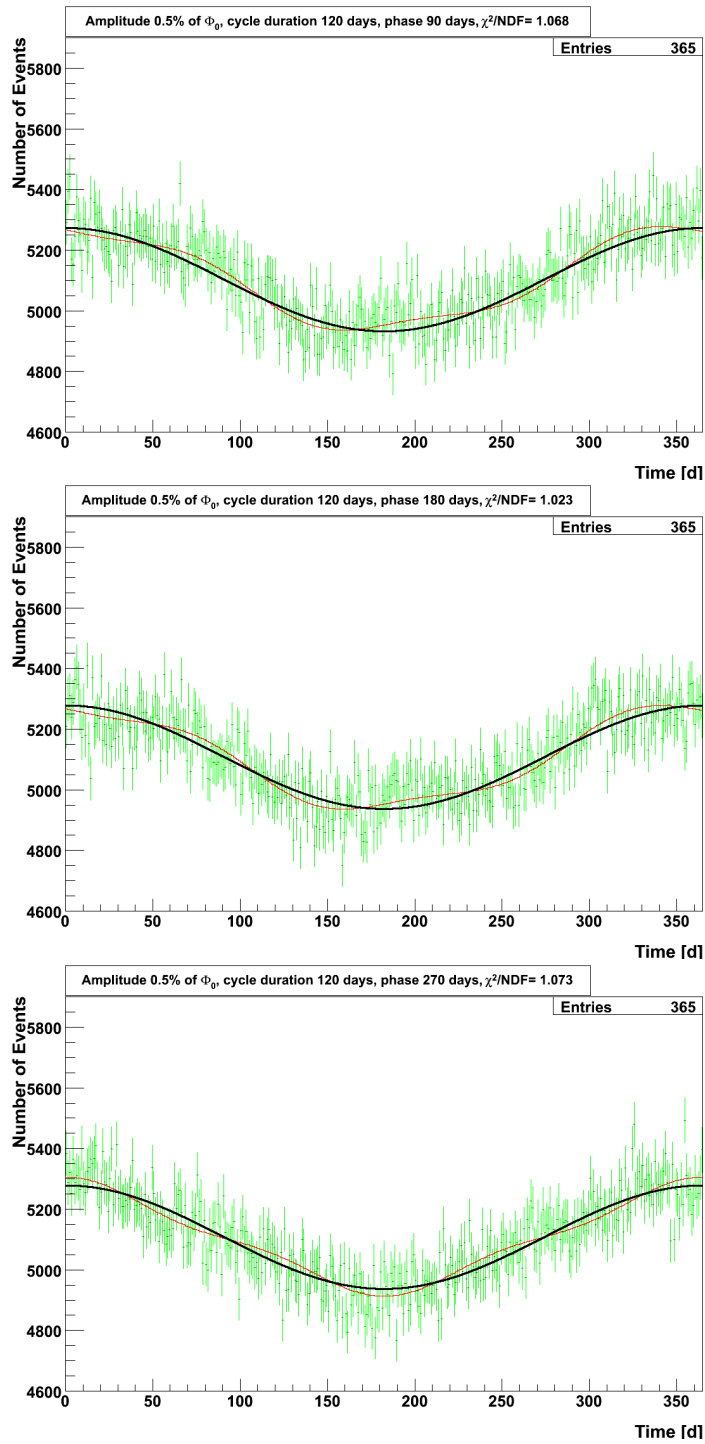


Figure 5.17: *This series of plots demonstrates the behaviour of the χ^2/NDF value for a fixed $T=120$ d, a fixed amplitude $A=0.5\%$, and a varying phase in steps of 90 days. The oscillation lies for this case within a detectable range for all three phaseshifts. The χ^2/NDF values are 1.068, 1.023 and 1.073, respectively, all three well within the exclusion threshold for a 1σ exclusion, thus the phase has no significant influence on the goodness of fit.*

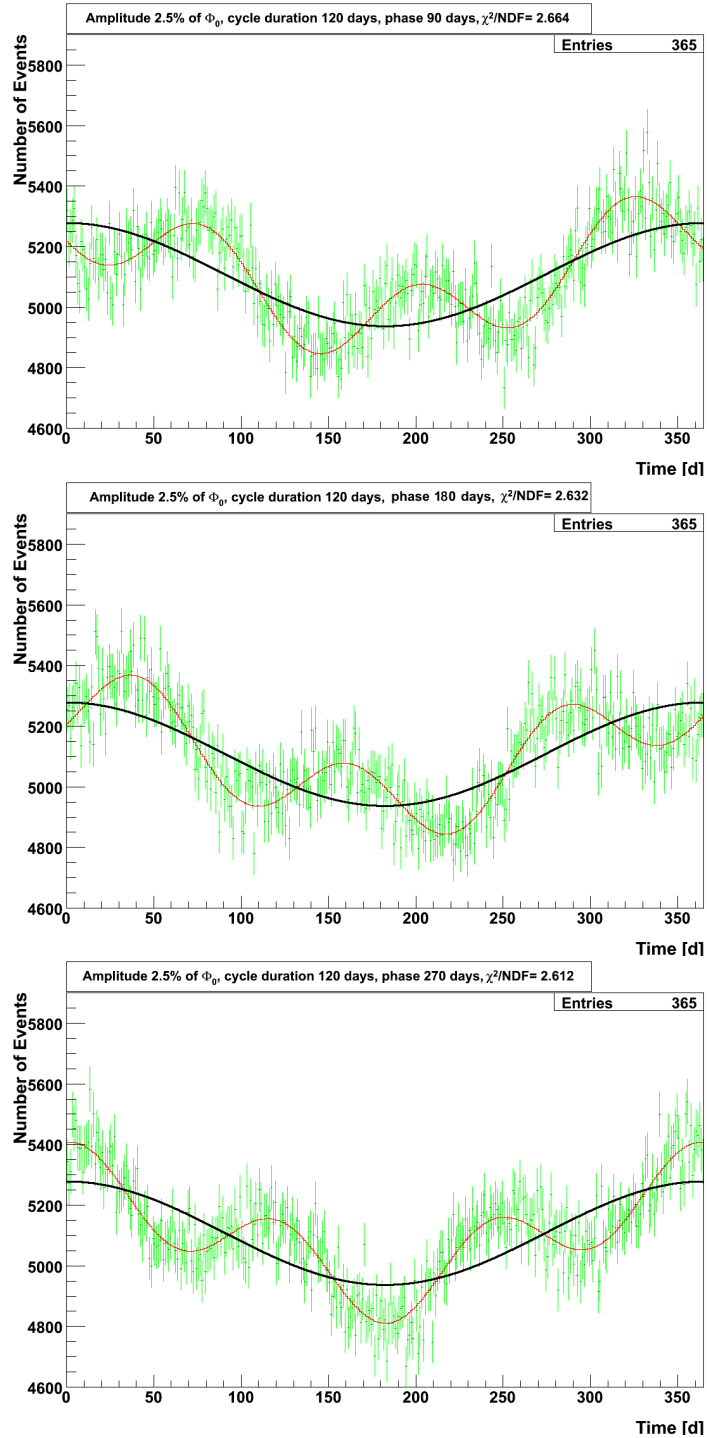


Figure 5.18: This series of plots demonstrates the behaviour of the χ^2/NDF value for a fixed $T=120$ d, a fixed amplitude $A=2.5\%$, and a varying phase in steps of again 90 days. All three data sets can be excluded on a 1σ and 3σ level. The χ^2/NDF values are 2.664, 2.632 and 2.612, respectively.

As can be seen, the phaseshift does not afflict the χ^2/NDF value in a significant way. It lies well within the statistical fluctuation of the χ^2/NDF value due to statistical fluctuations. The same conclusion can be drawn for the combination of cycle duration and phase. Here also, no significant dependance of the cycle duration from the phase can be seen. The amplitude was fixed to 1.5 % of Φ_0 (Figure 5.19).

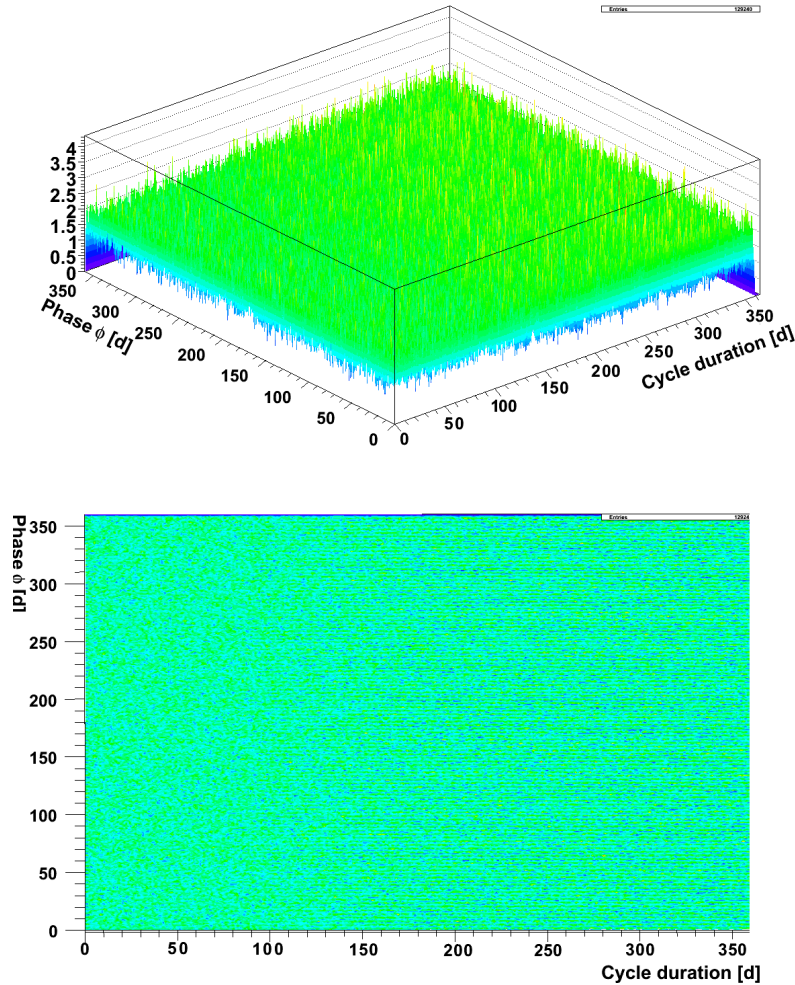


Figure 5.19: The χ^2/NDF distribution for a fixed amplitude $A=1.5\%$, and varying phase and cycle duration. As can be seen a very small dependance for the goodness of fit from the cycle duration and the phaseshift can be seen, but not on a statistical significant level. The blue areas mark good fits, whereas the green areas represent bad fits. On a 90 % C.L. or a 99 % C.L., respectively, no dependance can be seen.

The last series of plots demonstrates this behaviour (Figure 5.20). Again, as in the previous case, the phase does not affect the χ^2/NDF more than statistical fluctuations alone would. This is illustrated for a fixed phase of $\phi=180$ d, $A=2.5\%$ and a varying cycle duration T . If the same procedure is applied to small amplitudes

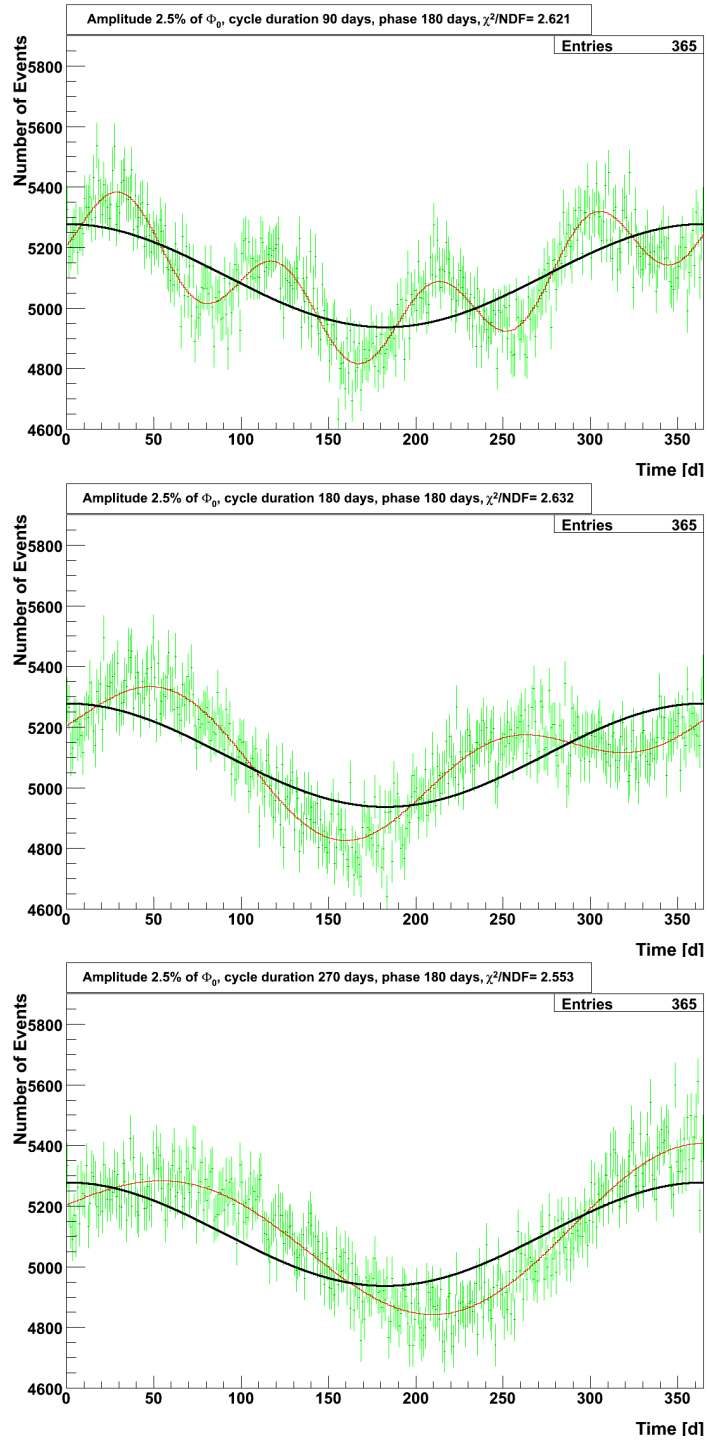


Figure 5.20: This series of plots demonstrates the behaviour of the χ^2/NDF value for a fixed amplitude $A=2.5\%$, fixed phase $\phi = 180$ d and varying cycle duration T in steps of 90 days. All three data sets can be excluded on a 99% C.L. The χ^2/NDF values are 2.621, 2.632 and 2.553. respectively.

in the range of 1.5 %, which is just at the border of detectability, it can be seen that the varying cycle duration does not affect the goodness of the fit in a significant way for a fixed amplitude and phase. Finally, it can be concluded that the detectability of oscillations of the ${}^7\text{Be}$ neutrino flux lie within an amplitude range of $\sim 1.4\% - 2.8\%$ of the initial neutrino flux Φ_0 on a 99 % C.L. Also, it can be concluded from the analysis that the phase (relative to the seasonal variation due to the elliptical orbit of the earth) does not influence the detectability of additional modes. In order to investigate the detectability potential for the day/night-effect, an analysis on shorter timescales is performed in the following section.

5.5.2 Analysis of oscillations with 1 hour binning

Because the binning of the first analysis was set to one day, oscillation modes in the order of hours could not be analyzed. This will be done in this section. With an estimated mean event rate of ~ 5400 events per day for a 200 keV threshold, LENA would be able to detect 225 ${}^7\text{Be}$ events per hour. The systematics of the analysis follows the same procedure as for the first analysis, but with a binning of one hour. The maximal time scale was set to 365 days. This makes a total of $365 \cdot 24 - 3 = 8757$ degrees of freedom for the χ^2 analysis. The confidence levels for an exclusion of the fit with $NDF = 8757$ can be calculated from the χ^2 probability density function [Har]. The result is $\chi^2/NDF \leq 1.0194$ for an exclusion on a 90 % C.L. and $\chi^2/NDF \leq 1.0355$ for a 99 % C.L.

Because of the increased NDF by a factor of 24, the amplitude was now changed in steps of 0.07 % (up to 2.1 % of Φ_0) instead of 0.005 % in order to reduce the computing effort. As was discussed in the previous section, the phase has no impact on the goodness of fit for a fixed cycle duration. The same can be seen for a fixed amplitude and a variable cycle duration and phase. Therefore the phase is now fixed to $\phi = 0$ h. Figures 5.21 and 5.22 show the obtained exclusion plots for the amplitude and the cycle duration for a fixed phase. Here, as in the case of a 1 day binning, the Nyquist-Shannon theorem [Nyq28] leads to the fact that low cycle durations (1 h – 10 h) can be neglected in this analysis.

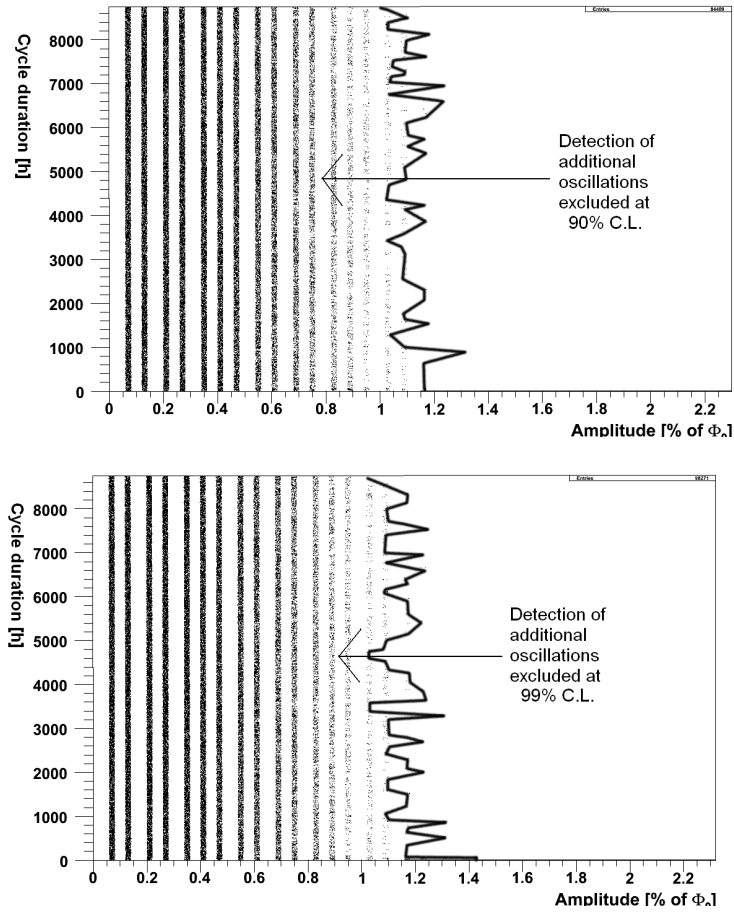


Figure 5.21: *These plots show the sensitivity range for the detection of oscillations at a 90% C.L. and a 99% C.L., respectively. The region on the left marks the area where additional oscillations beside the seasonal variation cannot be detected, while the white are on the right marks the area where the sensitivity is sufficient to measure these oscillations (with the respective C.L.). T was changed in steps of one hour up to $365 \cdot 24 = 8760$ hours, and the amplitude was changed in steps of 0.07% up to 2.1% of Φ_0 . As can be seen, oscillations down to $\sim (1.0 - 1.3)$ % are in the possible detection range for certain cycle durations.*

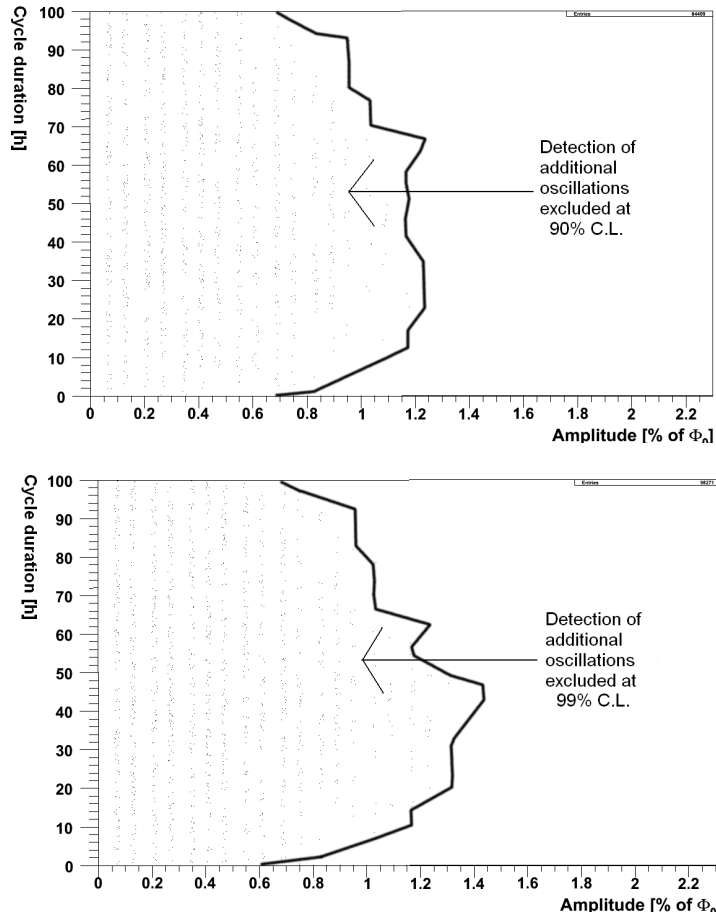


Figure 5.22: These two plots are the same as in Figure 5.21, with T up to 100 hours. Here, as in the case of a 1 day binning, the Nyquist-Shannon theorem [Nyq28] leads to the fact that low cycle durations (1h-10h) can be neglected in this analysis. At $T=24$ h, the detectable amplitude is 1.2% of Φ_0 on a 90% C.L. and 1.35% on a 99% C.L. A detection of the day/night-effect might lie within reach.

As can be seen, an amplitude of the order of 1 % is well within reach for an analysis with bins of 1 hour and a measurement duration of 365 days. Although the amount of ${}^7\text{Be}$ events per bin is far lower as in the case of bins of 1 day (225 events instead of 5400 events), the increased degrees of freedom compensate this effect and lead to a detectability of periodic oscillations of the ${}^7\text{Be}$ flux to $\geq 1\%$. As can be seen, for a cycle duration of 24 hours, which would be seen for the day/night-effect, a detection down to 1.2 % of Φ_0 is possible on a 90 % C.L. and down to 1.35 % on a 99 % C.L. A detection of the day/night-effect thus lies within reach.

Chapter 6

Scattering Length Measurement

In a liquid-scintillator detector of the scale of LENA, the optimization of the optical parameters of the used liquid-scintillator is crucial for the performance of a future detector. One parameter for example is the fluorescence time that has already been analyzed for different scintillators [Mar08]. This parameter is essential for a good time resolution and event separation. The other essential optical parameter is the attenuation length, which should be of the order of the detector radius so that the scintillation light of an event can reach the PMTs. A high attenuation length results in a high light yield of the detector. The attenuation length consists of the scattering length and the absorption length of the scintillator. A large scattering length is desirable for a good timeresolution and spatial event reconstruction. In this thesis, an experiment was set up to measure the scattering length (for the measurement of the attenuation length, see [Wur05]). As will be shown, the optical properties vary greatly for different liquid-scintillators. In the first section there will be given an overview over liquid-scintillation physics, and the different solvents and fluors. Then, the scattering theory is discussed. After that, the experimental setup and the electronic data aquisition system is presented. The last section will show the results of the scattering length measurements for all used scintillators and will be discussed.

6.1 On liquid-scintillators

A liquid-scintillator has the property of emitting light when hit by an incident particle. The liquid-scintillator serves both as a target and as a source of light emission, which then is detected by the photomultiplier tubes on the inner surface of the detector. The very short fluorescence time of the order of 10 ns allow a distinction of events happening within a very short time window. Moreover an organic liquid-scintillator has a low energy threshold (which is limited by the abundance of ^{14}C), and allows a good energy resolution due to its high light yield of $\sim 10^4\gamma/\text{MeV}$.

A liquid-scintillator consists of an aromatic hydrocarbon compound containing benzene-ring structures. The energy deposited by a passing particle excites the quasi-free (π orbitals) electrons of the benzene ring. When the valence electrons transit from the excited state to the ground state, scintillation light is emitted. The excited state comprises of a singlet and a triplet state. The singlet state decays faster, thus the scintillation light has a fast component 3-4 ns and a slow component (~ 20 ns).

6.1.1 The solvent

If only the solvent alone would be used as scintillator, the light would not reach the PMTs because the emitted light would be absorbed by the solvent itself, as the solvents emission band has a large overlap with its absorption band in the UV range. In order for this not to happen, wavelength shifters (fluors) are added so that the emitted wavelength is shifted towards larger wavelengths where the solvent is transparent (~ 430 nm) and enable the light to reach the detector surface. They usually are added in concentrations of a few g/l.

One of the most likely candidates that would come to use in LENA is Phenyl-o-Xylylethane ($C_{16}H_{18}$), short PXE, which is shown in following Figure 6.1. The PXE used in the scattering experiment is from the Dixie Chemical Group. The mean absorption and emission wavelengths of PXE are 270 nm and 290 nm, respectively [Mar08].

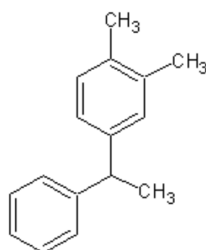


Figure 6.1: *The chemical structure of PXE.*

As can be seen, the PXE molecule consists of two connected benzene rings, with three methyl structures. In comparison with other liquid-scintillator candidates, PXE as a solvent is attractive for several reasons. First it has a high light yield. Second its density of 0.985 kg/l is very similar to the density of water. Thus, water could be used as a myon veto and as a buffer liquid around the inner vessel which would be filled with PXE thus avoiding buoyancy forces. In terms of safety, PXE has a relatively high flash point of about $145^{\circ}C$, and a low toxicity (See [Dix05]). The PXE used in the measurement of the scattering experiment is produced by the Dixie Chemical Company¹⁸. A disadvantage of PXE is for one thing the low

¹⁸300 Jackson Hill, Houston, 77007 Texas, USA.

attenuation length of only 4 meters. In order to increase the attenuation length to an order of the diameter of LENA, a purification method with an Al_2O_3 column has been investigated and delivered good results [Bx07b] with an increased attenuation length of up to 10 meters. The attenuation length can further be increased by the addition of Dodecane ($\text{C}_{12}\text{H}_{26}$) to the solvent. The structure of Dodecane can be seen in the Figure 6.2.

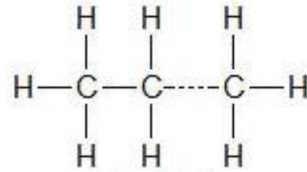


Figure 6.2: *The chemical structure of Dodecane.*

Another benefit from the addition of Dodecane would be the significant increase of the number of free protons (not bound in a nucleus), which means hydrogen atoms, in the same volume. This would enhance the sensitivity for detection of low energetic electron antineutrinos via the channel $\bar{\nu} + p \rightarrow n + e^+$. But as the density of a mixture Dodecane-PXE is lower than for PXE alone ($\rho_{\text{Dodecane}} = 0.749 \text{ kg/l}$), the number of protons in the whole scintillator (with the bound protons in the carbon nucleus included) decreases. This would lessen the sensitivity at the search for an eventual proton decay. Also the flash point of Dodecane is with 74°C lower than for PXE. But the main arguments against the use of Dodecane are a decrease of the light yield compared to PXE and the high costs. Two Dodecane samples from different manufacturers were used in the scattering experiment. One being from from Sigma-Aldrich¹⁹, the other one from the Chinese manufacturer Always Chem²⁰.

Another liquid-scintillator that could be considered for LENA is Linear Alcylbenzene (LAB, $\text{C}_9\text{H}_{12} + (\text{CH}_2)_m$, $m \in [7, 8, 9, 10]$). The chemical structure is shown in Figure 6.3. The mean absorption wavelength of LAB is 260 nm, while the mean emission wavelength is 283 nm [Mar08].

The density of LAB is 0.863 kg/l and the attenuation length is above 10 metres. LAB is a quite new solvent which is not only interesting for a use in LENA because of its high transparency, but also because of its high light yield and its low prize. Also, like PXE, LAB is non-hazardous and has a high flash point of 128°C . For the scattering experiment, the LAB was from Petresa²¹.

¹⁹3050 Spruce Street, St.Louis, MO 63103.

²⁰No.51 Taiping Road, Qingdao, China 266001.

²¹Campo de las Naciones, Avda del Partenon 12, 28042 Madrid, Spain.

6.2 Scattering and absorption of light in a liquid-scintillator

The light propagation in a liquid-scintillator can be described by two processes: Absorption and Scattering. The absorption processes are due to the fact that light emitted by the scintillator can be again absorbed by the scintillator itself with a certain probability that depends on the amount of fluors and impurities contained in the scintillator. The light can then be reemitted into a random direction with a certain probability (absorption- reemission process) or not²², in which case the light is lost for the detection with the PMTs. The other process is the scattering which can be divided into Rayleigh scattering (scattering of light on bound electrons) and Mie scattering (scattering of light on spherical particles of a diameter in the order of the wavelength of the light). If absorption and scattering are treated as independent processes, the intensity of the light can be described by a product of exponential decays:

$$I(x) = I_0 \cdot e^{-x/L_{Abs}} \cdot e^{-x/L_{Scat}} = I_0 \cdot e^{-x/L_{Att}} \quad (6.1)$$

With L_{Abs} being the absorption length, L_{Scat} the scattering length, and L_{Att} being the attenuation length. L_{Scat} is measured in the scattering length experiment for this thesis. As can be seen, the knowledge of two of the three optical lengths is sufficient to calculate the third.

6.2.1 Scattering theory

The scattering length can be derived from the particle density of the liquid-scintillator and the scattering cross section to

$$L_{Scat} = \frac{1}{n \cdot \sigma_{tot}} \quad (6.2)$$

with σ_{tot} being the total cross section for the scattering process [Wur05].

Rayleigh scattering

Rayleigh scattering is in general the elastic scattering of light or other electromagnetic waves on bound electrons (particles with $r \ll \lambda$), in this case the electrons of the liquid-scintillator atoms which are bound in molecules. This effect dominates in a liquid-scintillator with a high degree of purity. The scattering cross section for Rayleigh scattering is [Zin98]

²²In this case the excited molecule descends to the ground state via a radiationless transition

$$\frac{d\sigma}{d\Omega} = r_e^2 \frac{\omega^4}{(\omega_0^2 - \omega^2)^2} \frac{1 + \cos^2(\theta)}{2} \quad (6.3)$$

with $r_e = \frac{e^2}{4\pi\epsilon_0 m_e c^2} = 2.9\text{fm}$ being the classical electron radius, θ the scattering angle, ω the angular frequency of the light, and ω_0 the resonance frequency of the system. For air molecules, as well as liquid-scintillators, it lies in the ultraviolet regime. As can be seen, at $\theta = \pi/2$ the light is completely polarized parallel to the scattering direction and the intensity of the light is only half of the intensity at $\theta = 0$ or $\theta = \pi$. This effect will be essential for the scattering experiment as will be described later. An integration over the whole solid angle Ω delivers the total Rayleigh cross section, which simplifies for $\omega \ll \omega_0$ to

$$\sigma_{tot} = \frac{8\pi}{3} r_e^2 \left(\frac{\omega}{\omega_0}\right)^4 = \frac{8\pi}{3} r_e^2 \left(\frac{\lambda_0}{\lambda}\right)^4 \quad (6.4)$$

This is the well known ω^4 dependancy of the Rayleigh scattering amplitude. An estimation of the scattering length can now be calculated using equation 6.2. The result for PXE can be found in [Wur05] $L_{Scat,PXE} = 35\text{m}$. The scattering length for LAB can be calculated analogous, using the molecular weight of LAB $M_{mol} = 240\text{g/mol}$, the density $\rho_{LAB} = 0.863\text{g/cm}^3$ and the mean absorption wavelength $\lambda_0 = 260\text{nm}$ [Mar08]:

$$\sigma_{tot} = \frac{8\pi}{3} (2.9\text{fm})^2 \left(\frac{260\text{nm}}{430\text{nm}}\right)^4 = 10.16\text{fm}^2 \quad (6.5)$$

at a wavelength of 430 nm. The particle density can be calculated by

$$n_{LAB} = \frac{\rho_{LAB} \cdot N_A}{M_{LAB}} = 2.17 \cdot 10^{21}\text{cm}^{-3} \quad (6.6)$$

Using equation 6.2, the scattering length can be obtained: $L_{Scat,LAB} = 45\text{m}$.

Mie scattering

Mie scattering describes the scattering of electromagnetic waves on spherical particles that have a diameter in the order of the wavelength of the electromagnetic wave or higher. A detailed description of the theory can be found in [Bor06]. This theory develops the scattering process into a progression of spherical Bessel functions (because only spherical scattering particles are considered). The scattering is highly depending on the dielectricity coefficient of the scattering particle and on its diameter. In contrast to Rayleigh scattering, the light is preferably scattered into forward direction. The differential cross section can be described empirically by the Henyey-Greenstein formula:

$$\frac{d\sigma}{d\Omega} \propto \frac{1 - g^2}{(1 + g^2 - 2g \cdot \cos(\theta))^{3/2}} \quad (6.7)$$

The asymmetry factor g describes the difference of the cross section relative to the Rayleigh case in respect to the diameter of the scattering particles and the wavelength. The light from this scattering process can be partially polarized, whereas the polarization as well as the angular distribution depend heavily on the particle size. The impurities in the measured samples could contribute to the Mie scattering, but there is no evidence in the data that suggests this (see also chapter 6.4.1). The conclusion which can be drawn, is that the samples probably have a low level of contamination with impurities.

Absorption and reemission processes

The absorption and emission bands of the solvent molecules overlap, as has been stated before. Thus the probability is high that the light which was generated by the excitation of the solvent molecule by an incident particle, is absorbed again by another solvent molecule. Organic impurities abundant in the liquid-scintillator can also absorb the light, usually the absorption bands are at higher wavelengths than the absorption bands of the solvent molecules. The absorption probability is highest at the mean absorption frequency. The absorption excites the molecule and by the transition to the ground state, light is being emitted randomly into a 4π solid angle. The wavelength of the emitted light lies in the region of the emission band of the solvent molecule. This process can take place numerous times successively. The light generated by the absorption and reemission processes is unpolarized.

6.3 Experimental setup

The goal of the experiment is to measure the scattering lengths of different liquid-scintillators at different wavelengths. The scattering length is the length that a photon with a certain wavelength can travel on average within the scintillator until being scattered. The scattering length is a function of the wavelength of the photon. In order to measure the scattering length, the number of scattered photons N_{scat} has to be measured and set into relation to the number of photons which passed the sample without being scattered $N_{trans} = N_0 - N_{scat}$. N_0 is the initial number of photons that is emitted by the light source. In the experiment, the polarized and the unpolarized part of the light is being segregated and investigated separately.

6.3.1 Arrangement of the experiment

In order to shield it from external light, the whole setup is in a black box, which was covered from the inside with black felt. The experiment was mounted on a massive optical bench. Figures 6.5 illustrates the experimental setup, Figure 6.6 shows a

photograph of a sample in the experimental setup.

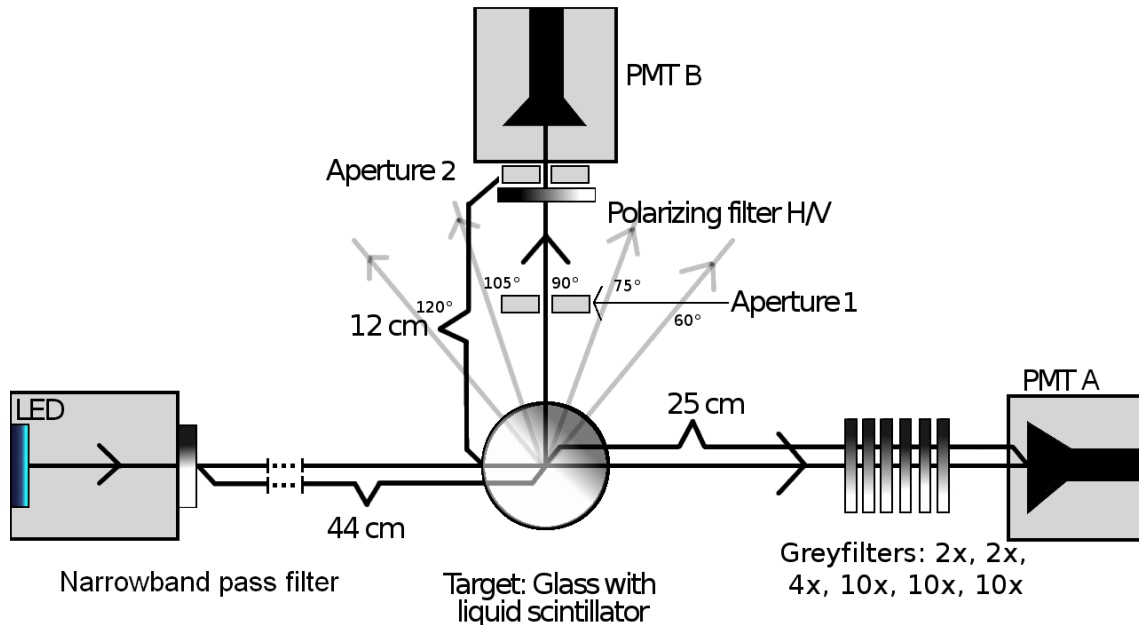


Figure 6.5: A schematic view of the experimental setup. The light which is emitted by the LED passes a narrowband pass filter. After that, it hits the target and if it is scattered into the right direction, it is being detected by the PMT B after it passes a polarizer and two apertures. If it passes the target, it passes 7 grey filters in order to lessen the light intensity to such an extent that it can be detected by PMT A without aggravating the PMT.

The light is being emitted by an LED of a certain wavelength. Two LEDs were used in the experiment, both from Roithner Laser Technik²³. The first LED with the description LED395-01V emits at 395 nm wavelength. It was used for the lower end of the wavelength area which was covered in the experiment. The other LED has the description LED430-06U, which emits with 430 nm. The light which is emitted by the LED then passes a narrow-band interference filter which only lets light of a certain wavelength pass. For the experiment four such filters from Edmund Optics²⁴ were used, thus the scattering length was measured for four different wavelengths: 396 nm, 415 nm, 430 nm and 442 nm.

After the light has passed the interference filter, it hits the target liquid-scintillator which is contained within an ordinary cylindrical glass with a diameter of 6.1 cm and a glass thickness of 1.1 mm. Glass begins to absorb in the ultraviolet range, so for this experiment it is still suitable, because the shortest wavelength of 396 nm was still optically visible. The scattered light then passes a polarizing filter which

²³Wiedner Hauptstrasse 76, 1040 Vienna, Austria.

²⁴Zur Giesserei 19-27, 76227 Karlsruhe, Germany.



Figure 6.6: *A photograph of a sample in the experimental setup. In the foreground there is the LED and the interference filter which is covered with felt. Then, the sample can be seen which is filled into a cylindrical glass and covered in order to keep it clean from dust particles. To the left, the PMT that detects the scattered light is covered with felt, as is the PMT in the background which detects the light that passed the sample.*

is mounted between two apertures. Aperture 1 with 1 cm x 6 cm is mounted in front of the polarizer. Aperture 2 with 1 cm x 2 cm is mounted directly in front of the PMT. The two apertures are used to define the field of view of the PMT and to avoid seeing spots of diffuse reflection where the beam enters or leaves the glass in which the sample is contained. The used linear polarizer is also from Edmund Optics. The polarizer alignment is horizontal and vertical and is changed after every measurement. This is done in order to separate the polarized Rayleigh scattered fraction of the light from the unpolarized part. Absorption and reemission processes do not change the polarisation of the light. Then, after passing the polarizer and the aperture, the light hits a PMT of type 9305 KB (Serial 4803) from Electron Tubes Limited²⁵ which is connected to the data acquisition system (see Figure 6.7). This PMT is mounted in such a way, that the observation angle can be adjusted in steps of 15° from 60° to 120°. In this way, the angular distribution of the polarized light can be examined. The light that passes the glass without being scattered (or through being absorbed and reemitted into the forward direction) then passes five grey filters which have the purpose to lessen the light intensity to a factor of about 1/16000 so that the light intensity is not too high for the PMT of the same build

²⁵100 Forge Way, Unit F, Rockaway, NJ 07866, USA.

which is also connected to the data acquisition system. Both PMTs are shielded from external magnetic fields by a coverage of μ -metal foil.

Electronics

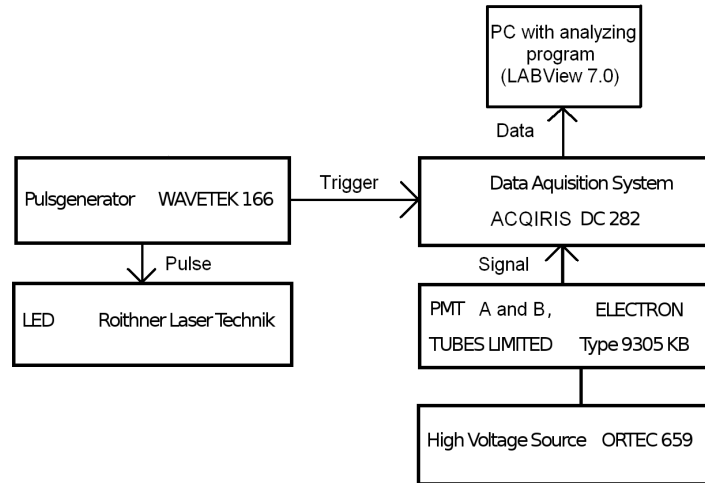


Figure 6.7: A block diagram of the electronics which was used for the data acquisition in the experiment.

The blockdiagram of the electronics is shown in Figure 6.7. The Wavetek 166 generates pulses of $25 \mu\text{s}$ length. These pulses are then transmitted to the LED. The Agilent Acqiris²⁶ data acquisition system is connected to the pulse generator and is triggered by the synchronous output of the pulse generator with a $25 \mu\text{s}$ timegate. The PMTs are operated at a voltage of 1.4 kV . Then the signals are sent directly to the data acquisition system. The Acqiris data acquisition system is a fast waveform digitizer that is recording the analog pulses. A PC with a customized program in National Instruments LABView 7.0²⁷ is analyzing the recorded pulses for the number of photons by counting voltage peaks. Each peak corresponds to a detected photon. The sampling rate for the experiment was set to 2 Gigasamples/s which corresponds to one sample every 0.5 ns or $50.000 \text{ samples per pulse}$. For one point of data acquisition (a certain angle with a certain liquid-scintillator and one of the two polarizer settings), $25.000\text{-}50.000$ pulses were measured in order to decrease the statistical uncertainty.

²⁶5301 Stevens Creek Blvd, Santa Clara, CA 95051, USA.

²⁷11500 N Mopac Expwy, Austin, 78759-3504 Texas, USA.

6.4 The measurement

A list of all the examined liquid-scintillator solvents together with their refractive indices can be found in Table 6.1.

Liquid-scintillator	Manufacturer	Refractive index
PXE	Dixie Chemical Group	1.569
PXE purified with Al ₂ O ₃	Dixie Chemical Group	1.569
LABp500	Petresa	1.482
LABp550	Petresa	1.482
LABp550q	Petresa	1.482
Dodecane	Sigma-Aldrich	1.422
Dodecane	Alway Chem	1.422
Cyclohexane (CH)	Merck ²⁸	1.426
Pseudocumene (PC)	Merck	1.505

Table 6.1: *A list of all liquid-scintillator solvents which were used for the experiment together with their refractive indices and the production companies.*

In addition to the measurement of the different liquid-scintillators, the scattering length of distilled water was also measured. This had the purpose to subtract the background when light is scattered off the glass from the actual scattering off the liquid-scintillator. Because water has a high scattering length in the order of more than 80 m [Shi99], very little scattering will take place when the glass is filled with water. If the glass was not filled with distilled water, but simply with air, the large difference between the refractive index of air ($n = 1.0003$) and of the glass ($n = 1.52$) would lead to a high degree of refraction and of light trapping in the glass by total reflection, thus changing the result to a high extent. However, with water ($n = 1.333$), the difference of the refractive indices is significantly smaller, and the refraction is lessened.

The purified PXE, the standard PXE, the Cyclohexane and the Dodecane from Sigma-Aldrich were measured for 4 different wavelengths, as was the water in order to subtract the background for every wavelength. This was necessary as the scattering length is a function of the wavelength. The other samples were measured only for three different wavelengths (415 nm, 430 nm and 442 nm). Every sample was then measured for each wavelength at 5 different angles and two polarizer settings (horizontal or vertical). As was later discovered, the angle of 60° delivered ratios that were too high, meaning that too much light was scattered and registered in PMT B. Through the use of a laser pointer it could be found that this was due to a

²⁸Frankfurter Str. 250, 64293 Darmstadt, Germany.

refraction reflex which occurred in this direction. Therefore the angle of 60° was left out of the analysis for the scattering length calculation. The goal of the experiment was to calculate the scattering lengths of the different samples and to examine the dependence of the scattering length from the used wavelength.

The essential value which is obtained from the measurement is the ratio between the value of the signals from PMT B to PMT A, which is a measure for how much light was scattered in the sample.

6.4.1 Calculation of the scattering lengths

The value that is measured in the experiment is the ratio of $I(\text{PMT B})/I(\text{PMT A})$, which is the ratio of the registered PMT intensities. The PMT B registers the scattered light, the PMT A registers the transmitted light. The differential loss of light intensity passing through a medium can be written as

$$dI = -\alpha \cdot I_0 \cdot dr \implies I(r) = I_0 \cdot e^{-\alpha \cdot r}; \quad (6.8)$$

A comparison with equation 6.1 then yields

$$\alpha = \frac{1}{L_{Abs}} + \frac{1}{L_{Scat}} = \frac{1}{L_{Att}} \quad (6.9)$$

Because in this experiment the scattered light fraction is measured, the scattering length instead of the attenuation length is the relevant parameter. But α is also a measure for the ratio of the differential scattered intensity to the initial intensity: $\alpha = dI_{Scat}/I_0$. Thus, a link between the ratio of the intensities and the scattering length is established. This α however, is an effective value, which is modified by the setup of the experiment. Several effects have to be taken into account. The ratio which is registered by the PMTs in the experiment, α_{exp} , is the ratio between the light intensities of the scattered light, and of the light in the beam of the LED:

$$\alpha_{exp} = \frac{I_{s,exp}}{I_{b,exp}} \quad (6.10)$$

Now a correction must be done in order to retrieve the ratios of the scattered beam to the initial beam, before passing the glass. Three quantities change this ratio. The first is the PMT efficiency, which is not the same for both PMTs, and is additionally dependent of the angle:

$$\epsilon(\theta) = \frac{\epsilon_b}{\epsilon_s} \cdot f(\theta) \quad (6.11)$$

Through changing the PMTs and comparing the obtained values, a value of $\epsilon_b/\epsilon_s = 0.7 \pm 0.0747$ was obtained. By rotating the experiment in steps of 15° from the initial direction to the perpendicular direction, $f(\theta)$ could be measured. The values

of $f(\theta)$ (See Table A.1 of Appendix A) show no clear correlation and are thus set as a limit for the uncertainty of the efficiency, see chapter 6.4.2. The transmission ratio of the filters has also to be taken into account, it is given by

$$t = \frac{t_g}{t_p} \quad (6.12)$$

t_g is the combined transmission of the greyfilters, t_p is the transmission of the polarizer. The values for the transmission of the greyfilters and of the polarizer together with the uncertainties, in dependance of the four wavelengths is shown in Table A.2 of the Appendix A.

The last quantity is the reflection, which is the amount of reflected light. Two reflections take place, the first when the light beam hits the glass surface, and the second time when it has traversed through the sample and hits the surface when it exits the glass. The fraction of the reflected light when hitting the glass surface for the first time is given by [Zin98]:

$$r = \left(\frac{n-1}{n+1} \right)^2 \quad (6.13)$$

and the second time it hits the glass surface, it is given by

$$r = \left(1 - \left(\frac{n-1}{n+1} \right)^2 \right) \cdot \left(\frac{n-1}{n+1} \right)^2 \cdot e^{-D/L_{Scat}} \quad (6.14)$$

The scattering length L_{Scat} is much larger than the diameter of the glass $D = 6.8$ cm, so that the factor $e^{-D/L_{Scat}}$ delivers a value between $0.99 - 1.00$ ²⁹. The light fraction that is not reflected the first time $1 - \left(\frac{n-1}{n+1} \right)^2$, passes the sample and is then being reflected a second time, which is expressed by equation 6.14. Combined, the effects of both reflections and of the scattering when passing through the sample, deliver a reflected light fraction of $r \approx (8.0 - 9.0)\%$, differing slightly for the different samples. All previously mentioned effects together (PMT efficiency, transmission of the filters and reflection off the glass filled with the respective sample (r_i)) lead to the corrected ratio

$$\alpha_{i,c} = \alpha_{i,exp} \cdot t \cdot \epsilon \cdot r_i \quad (6.15)$$

with $i = \text{PXE, LAB, Dodecane, CH, PC}$. After the correction for these three quantities, the next step is to subtract the contribution generated by the background, that means scattering that takes place by scattering off the glass itself. In order to achieve this, the glass was filled with very clean water and the scattered light was measured. Water has a high scattering length compared to the measured liquid-scintillators ($L_w = (88.5 \pm 11.5)$ m from [Shi99]) and because of its refractive index which is more

²⁹ L_{Scat} is in the order of 10 m and more, at the least a factor 100 higher than D , so that $e^{-D/L_{Scat}} \approx (0.99 - 1.00)$

similar to the glass than for air alone ($n_{water} = 1.33, n_{air} = 1.0003, n_{glass} = 1.52$), optical refractions are in this way limited. The ratio of the background α_{bg} has also to be corrected like α_c . α_{bg} consists of the measured background ratio $\alpha_{bg,exp}$, the transmission ratio of the filters, the efficiency of the PMTs ϵ , and the reflection r_{bg} off the glass filled with water:

$$\alpha_{bg} = \alpha_{bg,exp} \cdot t \cdot \epsilon \cdot r_{bg} \quad (6.16)$$

The factors t and ϵ are the same as for α_c , whereas the reflection has now to be calculated using the refractive index of water and the scattering length of water. Now the remaining ratio α_{rm} is the ratio which remains after subtraction of the difference of the corrected background ratio α_{bg} to the calculated ratio for water α_w . This difference is the ratio of the part which was scattered off the glass.

$$\alpha_{rm} = \alpha_c - (\alpha_{bg} - \alpha_w) \quad (6.17)$$

The intensity ratio of water, α_w , can be obtained by:

$$\alpha_w = \frac{\Omega_{w,1m} \cdot L_{w,sim}}{L_{w,real}} \quad (6.18)$$

where $\Omega_{w,1m}$ is the solid angle which was simulated for water as well as different samples in a Monte Carlo simulation for the experimental setup. The scattering length in the simulation was set to $L_{w,sim} = 1.0$ m, therefore it has to be divided through the real scattering length $L_{w,real}$ to obtain the ratio α_w . The intensity ratio of water can be divided into two contributions, assuming that only Rayleigh scattering takes place in the volume, $\alpha_{w,V}$ and $\alpha_{w,H}$ which add up to α_w :

$$\alpha_w = \alpha_{w,V} + \alpha_{w,H} \quad (6.19)$$

This relation together with the angle dependance of equation 6.3 yield

$$\alpha_{w,V} = \alpha_w \cdot \frac{1}{1 + \cos^2(\theta)}; \quad \alpha_{w,H} = \alpha_w \cdot \frac{\cos^2(\theta)}{1 + \cos^2(\theta)} \quad (6.20)$$

These relations are also satisfied for the other samples:

$$\alpha_i = \alpha_{i,V} + \alpha_{i,H} \quad (6.21)$$

with $i = \text{PXE, LAB, Dodecane, CH, PC}$.

The solid angle is the quotient of photons that were scattered into the direction of the aperture of the PMT B divided through the initial number of generated photons, and is of the order of 10^{-5} for all target materials. The solid angle Ω_i was, as already mentioned, determined by a Monte Carlo simulation (which was performed

by Martin Hofmann) of the experimental setup with GEANT4. This was done for water, but also for the different liquid-scintillators (PXE, Dodecane, CH, LAB), each with a scattering length set to 1 m. Therefore the intensity ratio for each sample can be obtained through equation 6.15. CH has refractive index very similar to Dodecane, thus the solid angle is considered to be the same for both samples, with the same approximation made for PC and LAB. For the Monte Carlo simulation, the dimensions of the experiment were taken into account and photons were generated, that were either reflected off the glass surface, or scattered in the sample, or passed the target volume without interaction. This procedure was done for angles between 0° and 90° in steps of 12.5° . Then the mean value of the solid angle from the MC-simulation was used for the calculation of the scattering length. The number of generated photons was in the order of 10^8 . Figure 6.8 shows the solid angle dependence of the angle for the example of PXE, which was obtained from the simulation.

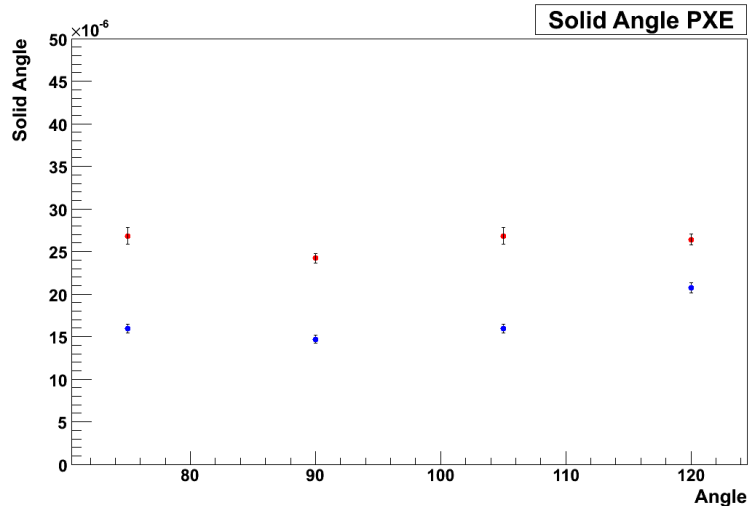


Figure 6.8: *The solid angle Ω together with the respective statistical uncertainties ($= \sqrt{N}$) $\Delta\Omega$ for the example of PXE obtained by a Monte Carlo simulation. Red represents the unpolarized, blue the polarized Rayleigh scattered part.*

If one compares Rayleigh and unpolarized scattering at a fixed scattering length (in this case 1 m), more photons will be scattered at the investigated angles ($75^\circ - 120^\circ$) for unpolarized than for Rayleigh scattering. The effective solid angle is therefore larger, $\Omega_U(\theta) > \Omega_R(\theta)$, which can be seen in Figure 6.8.

In order to get the ratio α_w of water with the assumed scattering length ($L_w = (88.5 \pm 11.5)$ m, see [Shi99]), the solid angle $\Omega_{w,1m}$ of water with a scattering length 1 m was calculated. It is the ratio between the scattered photons which are scattered into the aperture of PMT B to the number of photons that were generated ($1.6 \cdot 10^8$). The reflection off the water was also estimated using the simulation.

The simulation of the solid angle included the Rayleigh scattering. When integrating

over the angle θ , it has to be considered that the simulated solid angle dependance is of the form

$$\Omega_R(\theta) = \Omega \cdot \frac{1 + \cos^2 \theta}{2} \quad (6.22)$$

whereas the unpolarized part has no angular dependance. Summarized over all angles, the intensity must be the same, as the loss of beam intensity also remains the same. An integration thus delivers $\Omega_R = \Omega \cdot \frac{3}{4}\pi$ and $\Omega_U = \Omega \cdot \pi$. Thus the ratio of the Rayleigh to unpolarized solid angle is

$$\frac{\Omega_R}{\Omega_U} = \frac{3}{4} \cdot \frac{2}{1 + \cos^2(\theta)} \quad (6.23)$$

This effect will be taken into account later on.

Now the remaining ratio α_{rm} has to be divided by the solid angle from the Monte Carlo simulation. Therefore, the corrected ratio is

$$a_i = \frac{\alpha_i}{\Omega_i} \quad (6.24)$$

whereas i stands for the different liquid-scintillator samples that were measured, see Table 6.1. In order to obtain the scattering length, a χ^2 fit was performed. 4 fit curves were generated R_V , R_H , U_V and U_H , that stand for the horizontal and vertical parts of the rayleigh scattered and the unpolarized components, respectively. Now these parameters were obtained by fitting to the experimental values of a_V and a_H . The vertical and the horizontal part of the Rayleigh fit parameter have the following parametrisation:

$$R_H = R \cdot \frac{\cos^2(\theta)}{2}; \quad R_V = \frac{R}{2} \quad (6.25)$$

The unpolarized part consists of

$$U_V = U_H = \frac{U}{2} \quad (6.26)$$

The minimum of the χ^2 distribution now delivers the values for R and U. From the ratio of the rayleigh and the unpolarized solid angles (equation 6.19), it can be followed that the unpolarized parameter U is increased by a factor of 4/3, which results in the decrease of the unpolarized scattering length. U and R suffice the following condition for the scattering length:

$$L_R = \frac{1}{R}; \quad L_U = \frac{1}{\frac{4}{3}U} \longrightarrow L_{Scat} = \frac{1}{R} + \frac{1}{\frac{4}{3}U} \quad (6.27)$$

The Monte Carlo simulation was done for Rayleigh scattering and by comparing the fitted experimental to the Monte Carlo value, the scattering length could be

retrieved. The results for the different liquid-scintillators are listed and discussed in section 6.6.

6.5 Uncertainty contributions

Different uncertainties were analyzed and taken into account. For one thing there are statistical uncertainties, such as the uncertainty of the ratio of the PMT intensities, the statistical uncertainty of the Monte Carlo simulation for the solid angle, uncertainties due to the anisotropy of the glass surface ³⁰ and uncertainties due to the finite precisement of the measured angle. On the other hand there are the systematical uncertainties from the filters and the efficiency of the PMTs. There can also be made the distinction between uncertainties that influence all measurements in the same way (correlated), and uncertainties that differ for every measurement (uncorrelated). The light intensity of the LED is not constant over time, but does not contribute to the uncertainty, because what enters the calculation of the scattering lengths is the ratio between the two PMT channels. Thus, fluctuations of the intensity cancel themselves out. The error of the measured ratio α_{exp} can be given through the gaussian error distribution because the error of the filter ratio t is of statistical nature, also the efficiency of the PMTs ϵ . The error of the reflectivity of the glass was set to $r = 0$, because it should cancel itself roughly out for both light paths. Therefore, the error of the corrected ratio α_c , can be written as:

$$\begin{aligned} \Delta\alpha_c &= \sqrt{\left(\frac{\partial\alpha_c}{\partial\alpha_{exp}}\Delta\alpha_{exp}\right)^2 + \left(\frac{\partial\alpha_c}{\partial\epsilon}\Delta\epsilon\right)^2 + \left(\frac{\partial\alpha_c}{\partial t}\Delta t\right)^2} = \\ &= \sqrt{(t \cdot \epsilon \cdot r)^2 \Delta\alpha_{exp} + (\alpha_{exp} \cdot t \cdot r)^2 \cdot \Delta\epsilon + (\alpha_{exp} \cdot \epsilon \cdot r)^2 \cdot \Delta t} \end{aligned} \quad (6.28)$$

The errors from α_{exp} , ϵ and t will be discussed in detail.

6.5.1 Correlated uncertainties

Contribution to $\Delta\alpha_{exp}$ from the photon pile-up

Within a timewindow of 200 samples (100 ns), two incoming photons cannot be distinguished from one another. This has the effect that the LABView 7.0 software, which counts the photons in every pulse, delivers an error for the ratio of the PMT channels (channel3/channel1). The probability for a photon being in the timewindow of another photon is $\frac{\tau}{T}$, T being the length of the whole pulse (25 μ s) and τ

³⁰impurities, oil films or deformations of the glass

being the timeframe of 100 ns. If $\langle N \rangle = \frac{N}{T}$ is the mean rate of photons being registered within a pulse, and N the number of measured photons, the error can be written as³¹ $\Delta = \langle N \rangle \cdot \tau \cdot N = \frac{N}{T} \cdot \tau \cdot \frac{N}{T} \cdot T = \frac{\tau}{T} \cdot N^2$. This error is automatically calculated by the LABView 7.0 software, and enters the ratios accordingly.

The uncertainty of the efficiency of the PMTs $\Delta\epsilon$

The whole experimental setup was rotated in steps of 15° from the initial setup position to a perpendicular position in order to test the influence of the earth's magnetic field on the efficiency of the PMTs. Table A.1 lists the obtained values. No significant dependance of the efficiency from the angle θ could be found. The uncertainty which could be derived from Table A.1 is $\Delta\epsilon = 0.0747$. The efficiency of the PMTs was measured by switching the position of the PMTs, and the uncertainty of the efficiency was set to be the standard deviation σ of the values obtained by rotating the setup.

The uncertainty of the filters Δt

The transmission of the filters and the knowledge of their uncertainty is crucial for the calculation of the scattering lengths, because the absorption ratio of the filters $t = t_g/t_p$ enters the scattering length L_{Scat} linearly (see equations 6.12 and 6.15). The complete results for the measurement of the filter transmission for the four different wavelengths can be found in Table A.2. In order to measure the transmission, a measurement with the respective filter in front of PMT A was conducted, and in a second measurement the LED light intensity without the respective filter was measured. In order to lessen the light intensity of the LED to an amount suitable for the PMT, the other filters were in the beam while the respective filter was measured. The quotient of the measured intensities gives the fraction of transmitted light. The filter transmission was measured twice within the experimental setup. In order to check this method, another measurement series was conducted using a HR2000CG-UV-NIR spectrometer from Ocean Optics³². However, the spectrometer delivers $\sim 20\%$ lower results for the transmission of the filters than for the experimental setup. Because as of this point it is not known what effect causes this deviation, an uncertainty of 20% was estimated for the transmission of the filters, directly entering the scattering length. A similar effect was measured for the polarizing filter. A more precise knowledge of the filter transmission is desirable and further measurements are ongoing.

The FWHM of the narrow bandpass filters used for defining the incident wavelength (see Figure 6.5) is, according to the manufacturer Edmund Optics, 10 nm [Edm].

³¹The summarized probability is the mean rate of additional photons per timeframe of 100 ns for every registered photon, and N photons are registered.

³²830 Douglas Ave., Dunedin, FL 34698, USA.

The uncertainty of the solid angle correction $\Delta\Omega$

The solid angle (the field of view of PMT B) of the experiment has been derived by a GEANT 4 Monte Carlo simulation of the setup. The uncertainty for the solid angle Ω is statistical, it is given by $\Delta\Omega = \frac{\sqrt{N}}{N}$, where N is the number of photons registered by PMT B in the simulation. N is of the order of 10^{-6} to 10^{-7} . The dependance of the solid angle from the scattering angle is shown in Figure 6.8 for the example of PXE.

The uncertainty of the background ratio $\Delta\alpha_{bg}$

Starting from equation 6.13, the uncertainty can be derived analogous to $\Delta\alpha_c$ (see equation 6.28). This leads to the uncertainty

$$\Delta\alpha_{bg} = \sqrt{(t \cdot \epsilon \cdot r_w)^2 \Delta\alpha_w + (\alpha_w \cdot t \cdot r)^2 \cdot \Delta\epsilon + (\alpha_w \cdot \epsilon \cdot r_w)^2 \cdot \Delta t} \quad (6.29)$$

The uncertainty $\Delta\alpha_w$ can be derived from equation 6.18 also through gaussian error propagation:

$$\begin{aligned} \Delta\alpha_w &= \sqrt{\left(\frac{\partial\alpha_w}{\partial\Omega} \Delta\Omega\right)^2 + \left(\frac{\partial\alpha_w}{\partial L_w} \Delta L_w\right)^2} = \\ &= \sqrt{\left(\frac{1 \text{ m}}{L_w} \Delta\Omega\right)^2 + \left(\frac{\Omega \cdot 1 \text{ m}}{L_w^2} \Delta L_w\right)^2} \end{aligned} \quad (6.30)$$

6.5.2 Uncorrelated uncertainties

Anisotropy of the glass surface and impurities $\Delta\alpha_{glass}$

This uncertainty was retrieved through multiple measurements in the same setting, with the glass being rotated every measurement slightly around its axes. The variation of the results corresponds to the uncertainty which is caused by either dirt on the glass surface or anisotropies of the glass thickness itself. The uncertainty is about 4%.

Accuracy of the measured angle

The contribution from this effect is about 1% and is independent of the wavelength. This, together with the uncertainty from the glass surface contribute to the total uncertainty a value of $\sqrt{(4\%)^2 + (1\%)^2} \sim 4\%$.

6.6 Results

The obtained scattering lengths together with the uncertainties and the χ^2/NDF values from the fit procedure (see equations 6.25-6.27) are listed in Table 6.2. Scattering lengths with a high χ^2/NDF value are not as significant as scattering lengths with a χ^2/NDF of ~ 1 or lower. There were two measurement series conducted, the first one with a glass of slightly smaller diameter (6.6 cm). During the course of the measurements, the glass surface became too scratched, requiring a replacement of the glass. This glass had a slightly larger diameter (6.8 cm). By comparison of measurements of the same samples in the two series show that the resulting scattering lengths were not affected. The timespan between the first and the last series of measurements was nine months. The first series was only conducted for a fixed wavelength of 430 nm, whereas the second series was conducted at four different wavelengths: 396 nm, 415 nm, 430 nm, 442 nm (except for PC, which was not measured at 396 nm).

As can be seen, the scattering length of PXE in the first measurement series significantly lower than the calculated value of $L_{Scat} = 35$ m (see section 6.2.1). This is mainly due to the fact that there is additionally a contribution of the unpolarized scattering (absorption-reemission processes) to the Rayleigh scattering, which lowers the scattering length. It is not clear how large the contribution from Mie scattering on impurities is, because Mie scattering is only partially polarized, and cannot be segregated from the other scattering processes. The scattering length of PXE from the first measurement series is in good agreement with the scattering length of the second measurement series. The scattering lengths of the three LAB samples are similar within the uncertainties in the first series of measurements. LABp550 was additionally measured at a wavelength of 396 nm, which the result of a very low scattering length. The reason is probably the higher absorption of LAB in this wavelength regime. Here again the measured value is significantly lower than the calculated value of $L_{Scat} = 45$ m from section 6.2.1. As in the case of PXE, the absorption-reemission processes contribute to the scattering process and lead to a lower scattering length. The two Dodecane samples from different manufacturers have almost the same scattering length. Cyclohexane has the highest scattering length of all samples. In the second series of measurements, PC was analyzed in order to check the result with the value from a measurement of the scattering length of PC performed by the Borexino Collaboration [Bx00]. The obtained results are in good agreement³³ with the values from [Bx00].

Because of the contribution from absorption-reemission processes to the scattering, the samples do not show a clear Rayleigh $L_{Scat} \propto \lambda^4$ dependence. This behaviour would be observed if only Rayleigh scattering took place within the sample. However, it could be shown that the measured scattering lengths are in agreement with

³³ $L_{Scat,PC,Borexino} = 8.2$ m at 436 nm.

Liquid-scintillator	Series	Wavelength [nm]	Scattering length [m]	χ^2/NDF
PXE	1	430	(12.52 ± 4.08)	1.22
LABp500	1	430	(24.33 ± 8.58)	1.07
LABp550	1	430	(21.83 ± 5.99)	1.17
LABp550q	1	430	(22.68 ± 8.02)	0.75
Dodecane (Sigma-Aldrich)	1	430	(33.20 ± 12.21)	0.86
Dodecane (Alway Chem)	1	430	(33.15 ± 12.26)	0.72
Cyclohexane	1	430	(43.42 ± 16.86)	0.67
PXE	2	396	(0.14 ± 0.05)	0.40
PXE	2	415	(11.51 ± 3.58)	0.44
PXE	2	430	(10.50 ± 3.41)	1.63
PXE	2	442	(9.8 ± 3.18)	0.79
PXE purified with Al ₂ O ₃	2	396	(15.03 ± 5.43)	6.49
PXE purified with Al ₂ O ₃	2	415	(28.26 ± 9.68)	0.69
PXE purified with Al ₂ O ₃	2	430	(21.07 ± 8.04)	3.29
PXE purified with Al ₂ O ₃	2	442	(51.17 ± 26.62)	1.04
Cyclohexane	2	396	(11.49 ± 3.73)	1.27
Cyclohexane	2	415	(49.49 ± 17.36)	0.29
Cyclohexane	2	430	(42.45 ± 16.41)	2.20
Cyclohexane	2	442	(38.75 ± 15.75)	1.10
Dodecane	2	396	(9.68 ± 3.18)	3.04
Dodecane	2	415	(34.70 ± 11.66)	0.50
Dodecane	2	430	(35.88 ± 13.55)	2.38
Dodecane	2	442	(56.47 ± 25.44)	0.74
Pseudocumene	2	415	(8.80 ± 2.73)	0.43
Pseudocumene	2	430	(6.81 ± 2.16)	1.35
Pseudocumene	2	442	(7.54 ± 2.41)	0.32
LABp550	2	396	(0.14 ± 0.04)	0.37

Table 6.2: *These are the results from the scattering length experiment. There were two measurement series conducted, the first one with a different glass then the second one which had 2mm smaller diameter. It was changed due to the increased number of scratches on the surface during the course of the experiment. The time between the first measurement of series one (unpurified PXE) and the last measurement of series 2 (purified PXE) was 9 months.*

other experiments [Bx00] (for PC). This suggests that the other scattering lengths are within the range of validity. However, as of now, the scattering lengths still have large uncertainties. Efforts are ongoing to reduce this uncertainty by measuring the filter transmission with a better precision. First results of these measurements show that the transmission of the filters is closer to the value obtained by the measurement with the HR2000CG-UV-NIR spectrometer, than to the value obtained in the experimental setup.

Chapter 7

Summary and outlook

The first part of this thesis has been dedicated to the observation of solar neutrinos in the future large volume liquid-scintillator detector LENA. The Borexino detector has proven with its recent successes that even a spectroscopy of solar neutrinos with energies below 1 MeV is possible, with the first realtime detection of solar ${}^7\text{Be}$ neutrinos [Bx07a]. Also, a spectroscopic measurement of ${}^8\text{B}$ neutrinos in the energy regime above 2.8 MeV confirmed the MSW-LMA solution in the transition regime from vacuum to matter dominated neutrino oscillations [Bx08b]. As LENA would provide a much higher statistics than Borexino. LENA would therefore allow a precision measurement of neutrino fluxes both contributing to the understanding of solar fusion processes and of neutrino properties.

For this thesis, the fiducial mass of LENA was set to 18 kt, which is a conservative estimate because the fiducial mass of the finished detector could be higher. In the first step, the event rates for solar neutrinos were calculated for the elastic neutrino-electron scattering channel, which are summarized in Table 7.1.

The calculated total event rate for the ${}^{13}\text{C}$ reaction channels is ($R = 610 \pm 98$) yr^{-1} for $E_{thr} = 200$ keV and the same for $E_{thr} = 250$ keV, as the intrinsic threshold of the reaction channels is 2.22 MeV 3.68 MeV, respectively. The threshold energy is limited by the natural abundance of ${}^{14}\text{C}$ in the liquid-scintillator.

Besides from the event rates, the electron recoil spectra were calculated and drawn in Figure 5.1. The potential of LENA is strongly dependant of the level of radiopurity achieved for both the detector materials and the liquid-scintillator. Therefore an analysis of the radioactive background was performed. The background rates for LENA were estimated by scaling up the values of the Borexino detector to the fiducial mass of LENA. The production rate of the two cosmogenic radio nuclides ${}^{10}\text{C}$ and ${}^{11}\text{C}$ with respect to Borexino, were estimated with the result of $59.7 \cdot R({}^{11}\text{C} \& {}^{10}\text{C}, BX)$. This is only 1/3 of the production rate of cosmogenic radionuclides in Borexino, scaled down to its fiducial mass of 100 t. The background rates for radionuclides were estimated for the Pyhäsalmi site in Finland, the preferred detector location of LENA. The results are shown in Table 7.2.

$$E_{thr} = 200 \text{ keV}$$

Neutrino sort	Total Event Rate ($\nu_{e,\mu,\tau}$)
${}^7\text{Be}$	$(5.391 \pm 0.566) \cdot 10^3 \text{ d}^{-1}$
pep	$(389 \pm 6) \text{ d}^{-1}$
pp	$(844 \pm 8) \text{ d}^{-1}$
${}^8\text{B}$	$(2.8399 \pm 0.4544) \cdot 10^4 \text{ yr}^{-1}$
hep	$(60 \pm 10) \text{ yr}^{-1}$
CNO	$(656 \pm 1) \text{ d}^{-1}$

$$E_{thr} = 250 \text{ keV}$$

Neutrino sort	Total Event Rate ($\nu_{e,\mu,\tau}$)
${}^7\text{Be}$	$(4.763 \pm 0.500) \cdot 10^3 \text{ d}^{-1}$
pep	$(368 \pm 6) \text{ d}^{-1}$
pp	25 d^{-1}
${}^8\text{B}$	$(2.8076 \pm 0.4492) \cdot 10^4 \text{ yr}^{-1}$
hep	$(60 \pm 10) \text{ yr}^{-1}$
CNO	$(585 \pm 1) \text{ d}^{-1}$

Table 7.1: *Expected event rates R for solar neutrinos in LENA for a threshold energy of $E_{thr} = 200 \text{ keV}$, 250 keV , for the elastic neutrino-electron scattering channel. The threshold energy is limited by the natural abundance of ${}^{14}\text{C}$ in the liquid-scintillator.*

Isotope	Rate in Borexino	Estimated rate in LENA
${}^{14}\text{C}$	$2.0 \cdot 10^6 \text{ d}^{-1} (0.1 \text{ kt})^{-1}$	$3.6 \cdot 10^9 \text{ d}^{-1} (18 \text{ kt})^{-1}$
${}^{210}\text{Po}$	$(882 \pm 3) \text{ d}^{-1} (0.1 \text{ kt})^{-1}$	$(1.5876 \pm 0.0054) \cdot 10^5 \text{ d}^{-1} (18 \text{ kt})^{-1}$
${}^{210}\text{Bi}+\text{CNO}$	$(23 \pm 2) \text{ d}^{-1} (0.1 \text{ kt})^{-1}$	$(4140 \pm 360) \text{ d}^{-1} (18 \text{ kt})^{-1}$
${}^{85}\text{Kr}$	$(25 \pm 3) \text{ d}^{-1} (0.1 \text{ kt})^{-1}$	$(4500 \pm 540) \text{ d}^{-1} (18 \text{ kt})^{-1}$
${}^{214}\text{Pb}$	$0.92 \text{ d}^{-1} (0.1 \text{ kt})^{-1}$	$166 \text{ d}^{-1} (18 \text{ kt})^{-1}$
${}^{10}\text{C}$	$4 \text{ d}^{-1} (0.1 \text{ kt})^{-1}$	$239 \text{ d}^{-1} (18 \text{ kt})^{-1}$
${}^{11}\text{C}$	$(25 \pm 1) \text{ d}^{-1} (0.1 \text{ kt})^{-1}$	$(1493 \pm 60) \text{ d}^{-1} (18 \text{ kt})^{-1}$

Table 7.2: *The total background rates for the main radionuclides that are relevant for solar neutrinos. The data was taken from [Smi08], [Bx08a], and the values for LENA are upscaled on its fiducial volume of 18 kt. For the cosmogenic radionuclides (${}^{10}\text{C}$ and ${}^{11}\text{C}$), the production rate was estimated using further knowledge of the myon flux and average myon energy at Pyhäsalmi.*

Other background sources were also analyzed, for example reactor antineutrinos or atmospheric neutrinos, but they both can be neglected for solar neutrinos (see chapter 5.2.1).

Following the new measurement of ^8B neutrinos down to an energy of 2.8 MeV by the Borexino collaboration [Bx08b], an analysis of the detectability of the MSW-LMA solution for ^8B neutrinos was performed for LENA. The lower threshold is given by cosmogenic ^{10}C and radioactive background. Especially the low energy regime is interesting, because there the transition from vacuum dominated to matter dominated neutrino oscillations takes place. A χ^2 analysis was applied to simulated Monte Carlo ^8B spectra for LENA including or neglecting the MSW-LMA neutrino oscillations. This was done for a threshold energy of 2.0 MeV and 2.8 MeV, respectively, depending on the level of background discrimination of ^{10}C . The analysis shows, that for a measurement time of 24 months, LENA is able to prove the MSW-LMA solution on for the two threshold energies on a 99.5 % C.L (see Table 5.4).

A second analysis investigated the potential discovering periodic oscillations of the ^7Be neutrino flux. Besides from the seasonal induced variation of the solar neutrino flux in the order of 6.9 % due to the excentricity of the earth orbit, the earth matter induced day/night-effect and solar G modes could lead to periodic oscillations of the neutrino flux. For a data acquisition time of one year and a binning of one day, it could be shown (a Monte Carlo simulation was written for this purpose) that periodic oscillations of the flux can be detected down to 1.4 %-2.7 % (depending on the cycle duration T of the oscillations) of the average flux Φ_0 on a 99 % C.L. Smaller variations cannot be distinguished from the case without additional oscillations. The final exclusion plot is shown in Figure 7.1.

For a shorter binning of one hour, and a data acquisition time of one year, oscillations down to 0.7 %-1.4 % can be detected on a 99 % C.L. For a cycle duration of 24 hours, a detection down to 1.2 % of Φ_0 is possible on a 90 % C.L. and down to 1.35 % on a 99 % C.L. A detection of the earth-matter induced day/night-effect, which is in the order of 1 % of total flux, thus lies within reach.

The second part of the thesis describes an experimental setup which was used to measure the scattering lengths of different organic liquid scintillators. Besides the attenuation length L_{Att} and the absorption length L_{Abs} , the scattering length L_{Scat} is the third relevant optical parameter for an organic liquid-scintillator. For a given attenuation length, the scattering length has a large impact on the time- as well as spatial resolution of the detector. In the laboratory experiment, a light beam emitted by a LED at a defined wavelength (four wavelengths were measured: 396 nm, 415 nm, 430 nm and 442 nm) was scattered on a liquid-scintillator sample. The scattered light together with its polarization was detected by a PMT which could be set to 4 different scattering angles (75° , 90° , 105° , 120°), and then compared to the intensity registered by a second PMT in the light beam. From this ratio, together with

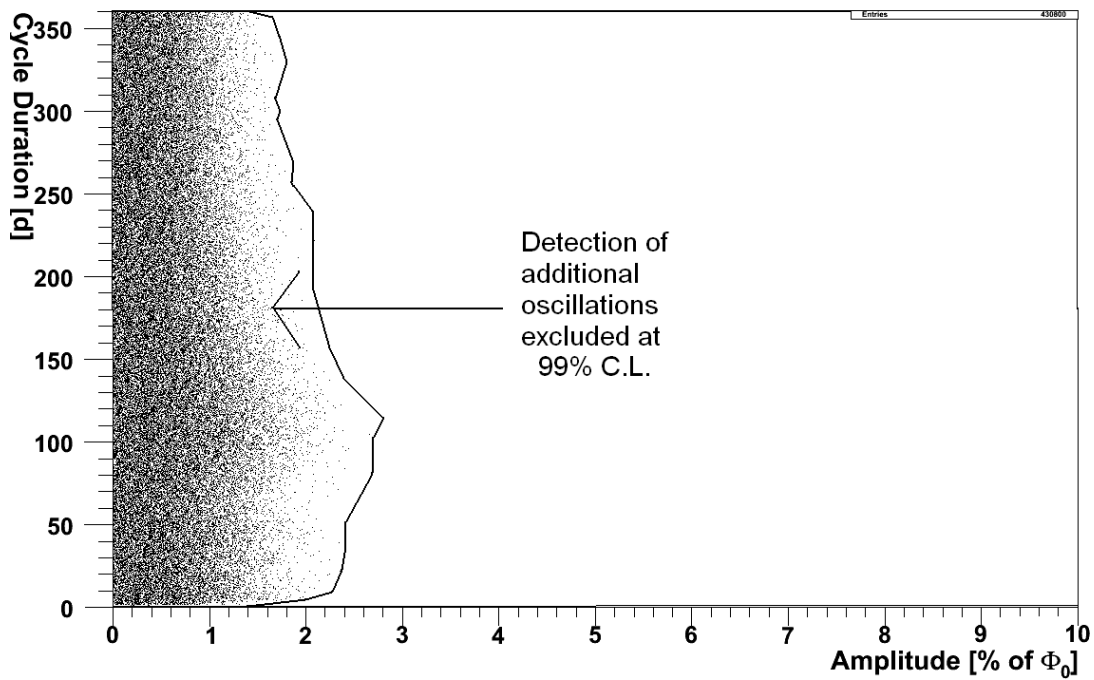


Figure 7.1: *This plot shows the sensitivity of the detector (for the detection of periodic oscillations) depending on the amplitude A and the cycle duration T (fixed phase $\phi = 0$ d). In the left region, a fit function without oscillations except the seasonal one would still reproduce the MC data, therefore it is excluded from detectability at a 99 % C.L. The right region marks the area where the sensitivity is high enough to measure such oscillations. A detection of oscillation amplitudes down to 1.4 % of Φ_0 and 2.7 % can be achieved after one year of data acquisition and a binning of one day on a 99 % C.L..*

several corrections (see chapter 6.4.1), the scattering length could be retrieved by fitting the experimental data to the expected behaviour of both Rayleigh scattering and absorption-reemission processes. As was shown (see table 6.2), no dependence of the scattering length from the wavelength of the form $L_{Scat} \propto \lambda^4$ could be obtained for the samples. This is due to the fact that in addition to Rayleigh scattering, absorption-reemission processes contribute to the scattering process, lowering the scattering length. The contribution of Mie scattering to the process is hard to disentangle, due to the property of Mie scattered light that it is only partially polarized. Table 7.3 shows the main results of the scattering lengths for a wavelength of 430 nm. This is the most important of the measured wavelengths, because the wavelength shifters emission is peaked in this regime.

Liquid-scintillator	Series	Scattering length [m]
PXE	1	(12.52 ± 4.08)
LABp500	1	(24.33 ± 8.58)
LABp550	1	(21.83 ± 5.99)
LABp550q	1	(22.68 ± 8.02)
Dodecane (Sigma-Aldrich)	1	(33.20 ± 12.21)
Dodecane (Alway Chem)	1	(33.15 ± 12.26)
Cyclohexane	1	(43.42 ± 16.86)
PXE	2	(10.50 ± 3.41)
PXE purified with Al ₂ O ₃	2	(21.07 ± 8.04)
Cyclohexane	2	(42.45 ± 16.41)
Dodecane	2	(35.88 ± 13.55)
Pseudocumene	2	(6.81 ± 2.16)

Table 7.3: *These are the results from the scattering length experiment for $\lambda = 430$ nm. PC is a reference measurement and was compared with a measurement from the Borexino Collaboration [Bx00]. The value of (6.81 ± 2.16) is well within agreement of $L_{Scat,PC,Borexino} = 8.2$ m at $\lambda = 436$ nm from [Bx00]. This suggests the validity of the other measured scattering lengths.*

A reference measurement was conducted with PC and compared to a measurement from the Borexino Collaboration and was found to be in good agreement. This leads to the conclusion that the other scattering lengths are within the range of validity. However, the uncertainty of the measured scattering lengths is still large because of the large uncertainty of the measurement of the filter transmission, which enters the scattering length linearly. Two measurement series were conducted, one using the initial experimental setup, the second one using a HR2000CG-UV-NIR spectrometer from Ocean Optics. Efforts are ongoing to measure the values more precisely, reducing the uncertainty of the scattering lengths and leading to a better

knowledge of this important optical parameter. First results of these measurements show that the transmission of the filters is more compatible with the results from the measurement with the spectrometer.

In the future, further investigations of the physical properties of liquid-scintillators will be performed. Further MC-simulations and phenomenological research will contribute to the understanding of the detector. A detector of such magnitude could yield physical results on many fields (see chapter 3) and is within the scope of technological feasibility.

Appendix A

Tables of measurements

Angle Θ [°]	PMT ch1 intensity	PMT ch3 intensity
0	1.474 ± 0.085	0.00634 ± 0.00082
15	1.541 ± 0.085	0.00562 ± 0.00069
30	1.360 ± 0.081	0.00530 ± 0.00048
45	1.392 ± 0.082	0.00662 ± 0.00066
60	1.462 ± 0.084	0.00469 ± 0.00055
75	1.621 ± 0.088	0.00442 ± 0.00053
90	1.626 ± 0.088	0.00453 ± 0.00048

Table A.1: *The PMT efficiency shows no clear correlation in respect to the rotation angle. The intensity values from PMT ch3 are lower and vary more, therefore the uncertainty of the efficiency is set to be the standard deviation σ of the values from PMT ch1, $\sigma = \Delta\epsilon = 0.0747$*

Wavelength [nm]	396	415
Greyfilter 2x nr.1	0.485 ± 0.081	0.515 ± 0.086
Greyfilter 2x nr.2	0.481 ± 0.080	0.500 ± 0.083
Greyfilter 4x	0.175 ± 0.030	0.190 ± 0.032
Greyfilter 10x nr.1	0.050 ± 0.008	0.073 ± 0.012
Greyfilter 10x nr.2	0.051 ± 0.008	0.073 ± 0.012
Greyfilter 10x nr.3	0.049 ± 0.008	0.070 ± 0.012
Total attenuation factor	$(2.009 \pm 0.401) \cdot 10^5$	$(5.458 \pm 1.092) \cdot 10^4$
Polarizer	0.028 ± 0.003	0.172 ± 0.040
Wavelength [nm]	430	442
Greyfilter 2x nr.1	0.526 ± 0.088	0.483 ± 0.081
Greyfilter 2x nr.2	0.509 ± 0.085	0.478 ± 0.080
Greyfilter 4x	0.226 ± 0.038	0.244 ± 0.041
Greyfilter 10x nr.1	0.090 ± 0.015	0.095 ± 0.016
Greyfilter 10x nr.2	0.089 ± 0.015	0.096 ± 0.016
Greyfilter 10x nr.3	0.072 ± 0.012	0.095 ± 0.016
Total attenuation factor	$(3.190 \pm 0.638) \cdot 10^4$	$(1.961 \pm 0.392) \cdot 10^4$
Polarizer	0.191 ± 0.027	0.229 ± 0.030

Table A.2: *The filter transmission as a function of the wavelength. The notation 2x, 4x, 10x indicates the attenuation factor as given by the manufacturer, Edmund Optics. As can be seen, all filters including the polarizing filter, have the strong tendency to absorb a higher fraction of light at smaller wavelengths. The polarizing filter for example absorbs 96.64 % of the light at 396 nm, and only 75,77 % at 442 nm. The total attenuation factor is the factor by which the light from the LED is lessened when traversing through all 6 filters. Between 396 nm and 442 nm, there is a factor ~ 10 difference. In addition, the measured total attenuation factor strongly differs from the manufacturer's value of $2 \cdot 2 \cdot 4 \cdot 10^3 = 1.6 \cdot 10^4$ for lower wavelengths. The uncertainty³ of the greyfilters is 20 % of the absorbed light fraction for every filter, respectively. This was estimated by measuring the filter transmission (greyfilters and polarizer) twice in the experimental setup, and twice with a spectrometer (HR2000CG-UV-NIR from Ocean Optics).*

Bibliography

- [Abd02] SAGE, J.N. Abdurashitov *et al.*, J. Exp. Theor. Phys. **95**, 181 (2002).
- [Ada08] P. Adamson *et al.* Fermilab-Pub-07-577-E, Phys.Rev. D **77** :072002 (2008), Vol. 77, No. 7, 1 April 2008.
- [Age07] M. Ageron *et al.* Nuclear Instruments and Methods in Physics Research A **581** (2007) 695-708.
- [Ahm02] Super-Kamiokande, Q. Ahmad *et al.*, Physics Letters B **539**, 179 (2002), arXiv:hep-ex/0205075.
- [Akh93] E. Kh. Akhmedov, S.T. Petkov, and A. Yu Smirnov, Phys. Rev. D **48**, 2167 (1993).
- [Alf47] Alfven, Hannes (1947). "Magneto hydrodynamic waves, and the heating of the solar corona". MNRAS 107: 211-219.
- [Alt95] GALLEX collaboration, M. Altmann *et al.*, Phys. Lett. B **357** 237 (1995).
- [Alt05] GNO, M. Altmann *et al.*, Phys. Lett. B **616**, 174 (2005).
- [Alt05a] G. Altarelli "The standard model of particle physics", arXiv:hep-ph/0510281.
- [Ama05] Amanda Collaboration, M. Ackermann *et al.*, Phys. Rev. D **71**, 077102 (2005).
- [Ang05] "Towards the detection of low energy solar neutrinos in Borexino: data read-out, data reconstruction and background identification", Dissertion Davide D'Angelo, March 2005, TUM.
- [Apo03] Apollonio *et al.*, CHOOZ collaboration "Search for neutrino oscillations on a long base-line at the CHOOZ nuclear power station", Eur. Phys. J C **27**, 331 (2003), arXiv:hep-ex/0301017.
- [Ara05] Araki T. *et al.* (KamLAND Collaboration) 2005 Nature **436** 499.

- [Ard08] Double CHOOZ, A search for the neutrino mixing angle θ_{13} , F. Ardellier *et al.* arXiv:hep-ex/0606025v4 (2006).
- [Asc04] Aschwanden, M. J. (2004). Physics of the Solar Corona. An Introduction. Praxis Publishing Ltd.. ISBN 3-540-22321-5.
- [Ash05] Super-Kamiokande Collaboration, Y. Ashie *et al.*, arXiv:hep-ex/0501064 (2005).
- [Aut07] The LAGUNA collaboration, D. Autiero *et al.*, arXiv:hep-ph/0705.0116 (2007).
- [Bai06] The BAIKAL collaboration, Zh.-A. Dzhilkibae *et al.*, arXiv:astro-ph/0609711 (2006).
- [Bah03] J. N. Bahcall *et al.* JHEP 02(2003), hep-ph/0212147.
- [Bah05] J. N. Bahcall *et al.* The Astrophysical Journal, 621:L 85-L 88, 2005 March 1.
- [BBM98] P. Bamert, C. P. Burgess and D. Michaud, Nucl. Phys. B 513, 319 (1998).
- [Bec07] J. Becker for the IceCube Collaboration "Implications of AMANDA neutrino flux limits", Journal of Physics: Conference Series **60** (2007) 219-222.
- [Bet07] A. Bettini, "GERDA. Germanium detector array. Search for neutrino-less beta beta Decay of ^{76}Ge ", Nucl. Phys. **B 168** (2007) 67.
- [Bio87] R. M. Bionta *et al.*, Phys. Rev. Lett. 58, 1494 (1987).
- [Bir64] J.B Birks, "The theory and Practice of Scintillation Counting", Pergamon Press, London (1964).
- [Boe04] C. Boehm, P. Fayet, and J. Sikl, Phys. Rev. **D69**, 101302 (2004), hep-ph/0311143.
- [Bor06] Max Born, "Optik", Springer Berlin, 4te Auflage (2006).
- [Bou02] SNO, M. Boulay *et al.*, Physical Review Letters **89** (2002), arXiv:nuclex/0204008.
- [Bra88] C. B. Bratton *et al.*, Phys. Rev. D **37**, 3361 (1988).
- [Buc06] W. Buchmüller, C. Lüdeling "Field Theory and Standard Model", arXiv:hep-ph/0609174v1, (2006).
- [Bur03a] C.P. Burgess *et al.*, arXiv:astro-ph/0304462v2 28 Apr 2003.
- [Bur03b] Burgess *et al.* arXiv:hep-ph/0310366v1 31 Oct 2003.

- [Bur03c] C.P. Burgess *et al.* arXiv:hep-ph/0312345v1 24 Dec 2003.
- [Bx00] "Light propagation in a large volume liquid scintillator" Borexino Collaboration, Nucl. Instrum. Meth. A440 (2000) 360-371.
- [Bx07a] "First realtime detection of ${}^7\text{Be}$ solar neutrinos by Borexino", Physics Letters B PLB-D-07-00772R2 (2007).
- [Bx07b] "Phenylxylylethane (PXE): a high-density, high-flashpoint organic liquid scintillator for applications in low-energy particle and astrophysics experiments" Borexino Collaboration, arXiv:physics/0408032v2 27 Sep 2007.
- [Bx08a] "New results on solar neutrino fluxes from 192 days of Borexino data" Borexino Collaboration, arXiv:0805.3843v2 [astro-ph], 9 June 2008.
- [Bx08b] A. Bellini *et al.* "Measurement of the solar ${}^8\text{B}$ neutrino flux with 246 live days of Borexino and observation of the MSW vacuum-matter transition", arXiv:0808.2868v1, 21.08.2008.
- [Cad02] L. Cadonati *et al.*, Astroparticle Physics **16**, 361 (2002).
- [Cer] <http://root.cern.ch/>.
- [Dav94] R. Davis, Prog. Part. Nucl. Phys. **32**, 13 (1994).
- [DG89] Domingo, V., Guyenne, T.D. (eds.): 1989, The SOHO mission: scientific and technical aspects of the instruments, ESA SP-1104.
- [Dix05] Dixie Chemical Company, PXE- Material Safety Data Sheet, 2005.
- [Edd79] J. Eddy "A New Sun: The Solar Results From Skylab" Washington, D.C: NASA SP-402, 37 (1979).
- [Edm] <http://www.edmundoptics.com/onlinecatalog/displayproduct.cfm?productID=1903>.
- [Enq05] T. Enquist *et al.* arXiv:hep-ex/0506032v1 13 June 2005.
- [Egu03] KamLAND, K. Eguchi *et al.*, Phys. Rev. Lett. **90** (2003).
- [Fal06] D. Falcone "Seesaw mechanism and leptogenesis", arXiv:hep-ph/0612041v1 5 Dec 2006.
- [Fer02] Fermilab-Pub 02/087-A (2002).
- [Fra08] Urbano Franca, "Mass Varying Neutrinos", ISAPP 2008.
- [Gon] National Solar Observatory, Global Oscillation Network Group.
- [GO05] Glatzmaier G. A. and Olson P. 2005 Scientific American April 33.

- [Gro95] Y. Grossman "Non-Standard Neutrino Interactions and Neutrino Oscillation Experiments", arXiv:hep-ph/9507344v1 (1995).
- [Hag00] "Messungen und Untersuchungen zur Bestimmung des kosmogenen Untergrunds im solaren Neutrinoexperiment Borexino" Dissertation Tanja Hagner, June 2000, TUM.
- [Hak05] T.Hakaya, Nucl. Phys. B, Proc. Suppl. **138**, 376 (2005).
- [Har] Hartung "Statistik", 12.Auflage Oldenbourg Verlag (1999), S.893.
- [Hir87] K. Hirata *et al.*, Phys. Rev. Lett. 58, 1490 (1987).
- [Hir88] K. Hirata *et al.*, Phys. Rev. D **38**, 448 (1988).
- [Hoc07] K.A. Hochmuth *et al.*, Astropart. Phys. **27**, 21 (2007).
- [Hol04] P.C. Holanda *et al.* Nuclear Physics B **702** (2004) 307-332.
- [Hol95] Wiberg Hollemann, "Lehrbuch der anorganischen Chemie", De Gruyter Berlin, 1995.
- [Ian05] A. Ianni *et al.* How to observe 8B solar neutrinos in liquid scintillator detectors, arXiv:physics/0506171v2 [physics.ins-det] 22 Sep 2005.
- [Ifa08] www.ifa.hawaii.edu/ (October 2008).
- [Kal08] Kalliosuunnittelu Oy Rockplan LTD, www.rockplan.fi/.
- [KAT04] "KATRIN Design Report 2004", FZKA Scientific Report 7090 MS-KP-0501.
- [Kin99] S.F. King "Large or Small Angle MSW from Single Right-Handed Neutrino Dominance" (1999).
- [Kir08] J. Kiryluk ,Proceedings of the Lake Louise Winter Institute 2008, 18-23 February 2008, Alberta, Canada, arXiv:0806.1717 [astro-ph], 10 June 2008.
- [Kla01] Klapdor-Kleingrothaus *et al.*, Modern Physics Letters A **16** 37(2001) 2409-2420.
- [Kob05] K. Kobayashi *et al.*, Phys.Rev. D **72**, 052007(2005).
- [Kot05] K. Kotake *et al.*, arXiv:astro-ph/0509456v2 (2005).
- [Kud03] V. A. Kudryavtsev *et al.* arXiv:hep-ex/0303007v1 9 March 2003.
- [Kum99] Kumar *et al.* arXiv:astro-ph/9808143v2 19 Feb 1999.
- [Lun06] C. Lunardani, arXiv:astro-ph/0610534 (2006).

- [Lyo08] K. Lyons "The KM3NeT Project", XXth Rencontres de Blois, May 18-23, 2008, Blois France.
- [Mal03] M.S. Malek *et al.* (Super- Kamiokande Collaboration), Phys. Rev. Lett. **90**, 061101 (2003).
- [Mar05] T. Marrodan Undagoitia *et al.*, Phys. Rev. D **72**, 075014 (2005).
- [Mar06] T. Marrodan Undagoitia *et al.* Journal of Physics: Conference Series **39** (2006) 287-290.
- [Mar08] "Measurement of light emission in organic liquid scintillators and studies towards the search for proton decay in the future large-scale detector LENA", dissertation Theresa Marrodan Undagoitia, TUM July 2008.
- [Mei08] Q. Meindl "Identification of Cosmogenic Background Signals in the Neutrino Experiment Borexino", Diploma Thesis, Technische Universität München (2008).
- [Mer08] E. Meroni talk on behalf of the Borexino Collaboration "Borexino and solar neutrinos", April 2008.
- [Mes06] P. Meszaros "Gamma-Ray Bursts", arXiv:astro-ph/0605208v5 (2006).
- [MPK] www.mpi-hd.mpg.de/nuastro/Viewphotos/ppchain.pdf, Max Planck Institut für Kernphysik.
- [MS85] S.P. Mikheyev and A. Yu Smirnov, Sov. J. Nucl. Phys. **42**, 913 (1985).
- [Nef05] M. Göger Neff *et al.* Nuclear Physics B (Proc. Suppl.) 143 (2005) 542.
- [Nyq28] H. Nyquist, "Certain topics in telegraph transmission theory", Trans. AIEE, vol.47, pp.617-644, Apr. 1928.
- [Obe05] Oberauer L, von Feilitzsch F, and Potzel W 2005 Nucl. Phys. B (Proc. Suppl.) **138** 108.
- [Ope08] Cecile Jolet and the OPERA collaboration, Journal of Physics: Conference Series 120 (2008) 052042.
- [Per] Donald H. Perkins, Introduction to High Energy Physics, 4th edition, Cambridge University Press, pages 250,251.
- [Pet01] S.T. Petcov, M. Piai "THE LMA MSW SOLUTION OF THE SOLAR NEUTRINO PROBLEM; INVERTED NEUTRINO MASS HIERARCHY AND REACTOR NEUTRINO EXPERIMENTS" arXiv:hep-ph/0112074v2 (2002).
- [Pov01] Povh, Rith, Scholz, Zetsche "Teilchen und Kerne", Eine Einführung in die physikalischen Konzepte", 5. Auflage (2001), Springer Verlag.

- [Rab02] S.Raby, talk presented at SUSY'02, DESY, Hamburg, Germany (2002).
- [RC56] "The neutrino", Frederick Reines and Clyde L. Cowan, Jr., *Nature* **178**, 446 (1956).
- [Scm97] N. Schmitz, *Neutrino Physik* (Teubner Studienbuecher: Physik, Stuttgart, 1997).
- [Sco08] Stefan Schoenert, MPIK Heidelberg, "Recent progress in double beta decay and low energy solar neutrino experiments", lecture ISAPP 2008, Valencia.
- [Shi99] Masato Shiozawa, "Search for Proton Decay via $p \rightarrow e^+ \pi^0$ in a Large Water Cherenkov Detector", November 1999, University of Tokyo.
- [Smi08] O. Smirnov, Internal analysis within the Borexino collaboration, February 2008.
- [SNS] <http://www.sns.ias.edu/> jnb, John Bahcall, Institute for Advanced Study, School of Natural Sciences Princeton, NJ, USA.
- [Sur08] Surman *et al.* American Physical Society, 2008 APS April Meeting and HEDP/HEDLA Meeting, April 11-15, 2008.
- [Wie04] Sören Wiesenfeldt "Proton Decay in Supersymmetric GUT Models", arXiv:hep-ph/0407173v3 (2004).
- [Win07] J/"urgen Winter, Diploma thesis, Technische Universitaet Muenchen, September 2007.
- [Wol78] L. Wolfenstein, *Phys. Rev. D* **17**, 2369 (1978).
- [Wur05] "Untersuchungen zu den optischen Eigenschaften eines auf PXE basierenden Flüssigszintillators und zum Nachweis von Supernovae Relic Neutrinos mit dem zukuenftigen Neutrinodetektor LENA", Diploma Thesis Michael Wurm, November 2005, TUM.
- [Wur07] M. Wurm *et al.*, *Phys. Rev. D* **75**, 023007 (2007), astro-ph/0701305.
- [Yao06] Yao *et al.* "Review of particle physics", *J. Phys. G* **33**, 1 (2006).
- [Yok05] K2K, M.Yokoyama *et al.*, *Phys. Rev. Lett.* **94** (2005).
- [Zin98] W. Zinth, H.J Körner, "Physik III, Optik, Quantenphänomene und Aufbau der Atome", 3. Auflage, Oldenbourg (1998).

Acknowledgements

Zum ersten möchte ich Prof. Franz von Feilitzsch für die freundliche Aufnahme am Lehrstuhl E 15 danken, und für seine Begeisterung der Astroteilchenphysik, von der ich mich damals in der Vorlesung anstecken ließ.

Des weiteren danke ich Prof. Lothar Oberauer für das Stellen einer sehr interessanten Diplomarbeit und für die sehr gute Betreuung dieser Arbeit. Er hatte immer ein offenes Ohr für Fragen.

Michael Wurm möchte ich für die exzellente Zusammenarbeit am Streuexperiment danken, und dafür dass er sich immer die Zeit nahm mir die Komplexität dieser Thematik näher zu bringen. Ich weiß nun dass allerlei verrücktes Zeug bei einem Streuexperiment passieren kann. Zusätzlich möchte ich ihm für das Korrekturlesen meiner Diplomarbeit danken.

Mein Dank gebührt insbesondere auch meinen freundlichen Bürokollegen Martin Hofmann, Nils Haag und Achim Gütlein. Allen dreien möchte ich nicht nur für das Korrekturlesen meiner Arbeit danken, sondern auch für die große Hilfsbereitschaft bei allen Problemen jeglicher Art, die mich beschäftigten. Insbesondere von Achim Gütlein konnte ich viel über Programmieren lernen. Explizit müssen Martin Hofmann und Achim Gütlein noch für die knallharte Konsequenz gelobt werden, den Spitznamen Höneß zu etablieren.

Teresa Marrodán Undagoitia möchte ich auch für die zahlreichen Anregungen und Tipps und ihr großes Engagement danken, sie gab mir oft neue Denkanstöße. Während meiner Zeit als Werkstudent konnte ich bei ihr auch viel lernen, was mir später bei der Diplomarbeit zugute kam.

Quirin Meindl möchte ich gerne für die guten Gespräche danken, speziell für seine zahlreichen Ausführungen über Command&Conquer und Star Wars. Doch auch für programmiertechnische Probleme hatte er immer ein offenes Ohr und er half mir oft weiter.

Timo Lewke und Jürgen Winter möchte ich für die lustige und schöne Zeit in Valencia danken. Insbesondere von Timo Lewke konnte ich viel über die effiziente Zeitausnutzung bei den langweiligeren Vorträgen lernen, dafür auch danke. Jürgen Winter möchte ich noch für die Tipps bezüglich solarer Neutrinos am Anfang meiner Diplomarbeit danken.

Allen die hier nicht explizit erwähnt worden sind, möchte ich für die nette und sehr freundliche Atmosphäre am Lehrstuhl danken. Ich habe die Zeit hier sehr genossen.

Nicht zuletzt aber möchte ich meinen Eltern danken, ohne deren liebe Unterstützung diese Diplomarbeit garnicht möglich gewesen wäre.